Title

High-Pressure Investigations of Correlated-Electron Phenomena

Author

Wolowiec, Christian

Publication Date

2017

UNIVERSITY OF CALIFORNIA, SAN DIEGO

High-Pressure Investigations of Correlated-Electron Phenomena

A dissertation submitted in partial satisfaction of the
requirements for the degree
Doctor of Philosophy

in

Physics

by

Christian Todd Wolowiec

Committee in charge:

Professor M. Brian Maple, Chair
Professor Olga K. Dudko
Professor Michael Fogler
Professor Eric E. Fullerton
Professor Congjun Wu

2017

The dissertation of Christian Todd Wolowiec is approved, and it is acceptable in quality and form for publication on microfilm and electronically:

Chair

University of California, San Diego

2017

DEDICATION

To my loving parents, Prudence and Richard, for their continued support, and to my son, Gabriel Sebastian, for inspiring me to do my best.

EPIGRAPH

There is no subject so old that something new cannot be said about it.

—Fyodor Dostoevsky

TABLE OF CONTENTS

LIST OF FIGURES

LIST OF TABLES

ACKNOWLEDGEMENTS

Spanning more than half a century and including more than a thousand publications, Professor M. Brian Maple's career in science speaks for itself. His generosity, kindness, and character are of equal stature and unparalleled in this field. I am sure Brian would disagree, but these are the qualities that make him unique and are the primary reason why I am able to write these introductory remarks to a completed and approved dissertation. I am greatly indebted to Professor Maple for his guidance and support during the last five years regarding matters of research and life in general.

In the following paragraphs, I would also like to give thanks to the many people, professionally and personally, that factor into the success of the research and the completion of my graduate work. I have no choice but to first acknowledge Professor Benjamin D. White, who, as a postdoc in the Maple laboratory, welcomed me to the group. It was Ben who introduced me to pressure work and mentored me in performing low-temperature measurements of electrical resistivity for materials under pressure using the piston-cylinder cell technique. Beginning with my first day in the group until Ben's final day as a postdoc, before he left the group to start a position as an assistant professor, Ben was always courteous to me and exemplified professionalism to the highest degree.

As regards high-pressure work, I am extremely grateful to Dr. Jason Jeffries and Dr. Ryan Stillwell at Lawrence Livermore National Laboratory (LLNL) for sharing their time and expertise in assisting me and others in this laboratory with techniques related to the diamond anvil cell (DAC). The high-pressure DAC experiment reported herein would not have been possible without their work in loading our DAC with TiAu. In conjunction, the work of both Dr. Sam Weir at LLNL and Professor Yogesh K. Vohra at the University of Alabama, Birmingham, who continue to generously provide our laboratory with designer diamond anvils, is indispensable to the ongoing high-pressure investigations in our group. I also owe many thanks to Zack Rehfuss for accompanying me on a visit to LLNL

for DAC training and for his initiative in tackling the daunting task of loading a DAC upon our return to San Diego; and to Dr. Colin McElroy and Yuankan Fang for their work in the pressure room, particularly in the building of Bridgman anvil cells. I also can't forget to mention Professor James Hamlin's willingness to field all of my questions either by phone or email regarding equipment in the pressure room. Finally, I am greatly indebted to Don Johnson and the staff in the Campus Research Machine Shop (CRMS), who consistently deliver quality machined parts that are essential to the successful performance of the pressure cells.

I owe many thanks to various members of the Maple Group, past and present, including Alex Breindel for leading the way with the dilution refrigerator experiments and for helping out with all things computer related; Dr. Sheng Ran, Dr. Inho Jeon, and Naveen Pouse for their work in single crystal synthesis of URu_2Si_2; and Professor Duygu Yazici for her excellent and original work on the bismuth sulfide materials.

I would also like to acknowledge the various people in the Physics department that have helped both the laboratory and me personally including Brad Hanson in the Physics department machine shop for providing instruction in machining and always being available to help out with a project; Mike Rezin in the Physics department electronics shop for providing technical support and service on short notice, which has saved the laboratory thousands of dollars; Lester Brooks and Dirk Johnson in Facilities Management for their willingness to work with the laboratory during the construction of the helium recovery system; Kevin Smith, Simone Radice, Brendan Dennis, and Bryan D. Hill in the Physics Computing Facility for helping out with everything from personal computing to software management to bailing us out of deep water on several occasions regarding hardware failure; Hilari Ford, Sharmila Poddar, and Catherine McConney in Student Affairs for propelling me toward the completion of my degree, up to the very last minute. I owe a special thank you to Robin Knox in the Center for Advanced Nanoscience business office for her kindness and support. I would also like to express my appreciation to Professor Maple's administrative assistant, Christine Coffey, for her overall competence, her ability to work with the many personalities in the laboratory, her effort in planning and facilitating my travel to conferences, and for occasionally sharing her wisdom on parenthood.

Finally, I would like to thank my family for their love and support over the last eight years: my mother and father, Prudence and Richard, for finding the time to make visits to San Diego, which were cherished by Gabriel and myself; and Darlene Wolowiec for all her thoughtfulness and help with Gabriel both in San Diego and in Wofford Heights. Lastly, I will always remember and be grateful for the love and support shown to me by my father, especially over the last few years. He has been there for me every step of the way in navigating this new chapter of my life.

Chapter 4, in full, is a reprint of the article, "Pressure-induced enhancement of superconductivity and suppression of semiconducting behavior in $Ln\mathrm{O}_{0.5}\mathrm{F}_{0.5}\mathrm{BiS}_2$ (Ln = La, Ce) compounds," by C. T. Wolowiec, D. Yazici, B. D White, K. Huang, and M. B. Maple, as it appears in *Phys. Rev. B* **88**, 064503 (2013). The dissertation author was the primary investigator and author of this paper.

Chapter 5, in full, is a reprint of the article, "Enhancement of superconductivity near the pressure-induced semiconductor-metal transition in the BiS_2-based superconductors $Ln\mathrm{O}_{0.5}\mathrm{F}_{0.5}\mathrm{BiS}_2$ (Ln = La, Ce, Pr, Nd) compounds," by C. T. Wolowiec, B. D White, I. Jeon, D. Yazici, K. Huang, and M. B. Maple, as it appears in *J. Phys.: Condens. Matter* **25**, 422201 (2013). The dissertation author was the primary investigator and author of this paper.

Chapter 6, in full, is a reprint of the article, "Evolution of critical pressure with increasing Fe substitution in the heavy-fermion system $\mathrm{URu}_{2-x}\mathrm{Fe}_x\mathrm{Si}_2$," by C. T. Wolowiec, N. Kanchanavatee, K. Huang, S. Ran, and M. B. Maple, as it appears in *Phys. Rev. B* **94**, 085145 (2016). The dissertation author was the primary investigator and author of this paper.

Chapter 7, in full, is a reprint of the article, “Pressure effects in the itinerant antiferromagnetic metal TiAu,” by C. T. Wolowiec, Y. Fang, C. A. McElroy, J. R. Jeffries, R. L. Stillwell, E. Svanidze, J. M. Santiago, E. Morosan, S. T. Weir, Y. K. Vohra, and M. B. Maple, as it appears in *Phys. Rev. B* **95**, 214403 (2017). The dissertation author was the primary investigator and author of this paper.

Funding for the high-pressure research performed at the University of California, San Diego was provided by the National Nuclear Security Administration (NNSA) under the auspices of the Stewardship Stockpile Academic Alliances (SSAA) through the United States Department of Energy (DOE) under Grant Nos. DE-NA0001841 and DE-NA0002909. Some aspects of the research including synthesis, characterization, and low-temperature measurement of the samples overlap with projects funded by the United States DOE, Office of Basic Energy Sciences, Division of Materials Sciences and Engineering, under Grant No. DE-FG02-04-ER46105 and the National Science Foundation under Grant No. DMR 1206553.

VITA

1993	B. A. in Economics, University of California, Los Angeles
2003	B. S. in Physics, San Jose State University
2003	B. A. in Mathematics, San Jose State University
2003-2006	Mathematics Teacher, Gilroy High School
2006-2009	Graduate Teaching Assistant, California State University, Northridge
2006-2009	Graduate Research Assistant, California State University, Northridge
2009-2012	Graduate Teaching Assistant, University of California, San Diego
2012	M. S. in Physics, University of California, San Diego
2012-2017	Graduate Research Assistant, University of California, San Diego
2017	Ph.D. in Physics, University of California, San Diego

PUBLICATIONS

C. T. Wolowiec, Y. Fang, C. A. McElroy, J. R. Jeffries, R. L. Stillwell, E. Svanidze, J. M. Santiago, E. Morosan, S. T. Weir, Y. K. Vohra, and M. B. Maple, "Pressure effects in the itinerant antiferromagnetic metal TiAu," *Phys. Rev. B* **95**, 214403 (2017).

S. Ran, C. T. Wolowiec, I. Jeon, N. Pouse, N. Kanchanavatee, B. D. White, K. Huang, D. Martien, T. DaPron, D. Snow, M. Williamsen, S. Spagna, P. S. Riseborough, and M. B. Maple, "Phase diagram and thermal expansion measurements on the system of $URu_{2-x}Fe_xSi_2$," *Proc. Natl. Acad. Sci.* **113**, 13348 (2016).

C. T. Wolowiec, N. Kanchanavatee, K. Huang, S. Ran, and M. B. Maple, "Evolution of critical pressure with increasing Fe substitution in the heavy-fermion system $URu_{2-x}Fe_xSi_2$," *Phys. Rev. B* **94**, 085145 (2016).

A. Ślebarski, J. Goraus, M. M. Maśka, P. Witas, M. Fijałkowski, C. T. Wolowiec, Y. Fang, and M. B. Maple, "Effect of atomic disorder and Ce doping on superconductivity of $Ca_3Rh_4Sn_13$: Electric transport properties under high pressure," *Phys. Rev. B* **93**, 245126 (2016).

Y. Fang, C. T. Wolowiec, D. Yazici, and M. B. Maple, “Chemical substitution and high pressure effects on superconductivity in the LnOBiS$_2$ (*Ln* = La-Nd) system,” *Novel Superconducting Materials* **1**, 79 (2015).

C. T. Wolowiec, B. D. White, and M. B. Maple, “Conventional Magnetic Superconductors,” *Physica C Special Issue, Superconducting Materials: Conventional, Unconventional, and Undetermined* **514**, 113 (2015).

C. T. Wolowiec, B. D. White, I. Jeon, D. Yazici, K. Huang, and M. B. Maple, “Enhancement of superconductivity near the pressure-induced semiconductor-metal transition in the BiS$_2$-based superconductors *Ln*O$_0$.5F$_0$.5BiS$_2$ (*Ln* = La, Ce, Pr, Nd) compounds,” *J. Phys.: Condens. Matter* **25**, 422201 (2013).

C. T. Wolowiec, D. Yazici, B. D. White, K. Huang, and M. B. Maple, “Pressure-induced enhancement of superconductivity and suppression of semiconducting behavior in *Ln*O$_0$.5F$_0$.5BiS$_2$ (*Ln* = La, Ce) compounds,” *Phys. Rev. B* **88**, 064503 (2013).

Luis A. Agapito, Jacob Gayles, Christian Wolowiec, and Nicholas Kioussis “Aviram-Ratner rectifying mechanism for DNA base-pair sequencing through graphene nanogaps," *Nanothechnology* **23** (13), 15202 (2012).

ABSTRACT OF THE DISSERTATION

High-Pressure Investigations of Correlated-Electron Phenomena

by

Christian Todd Wolowiec
Doctor of Philosophy in Physics

University of California San Diego, 2017

Professor M. Brian Maple, Chair

This dissertation includes a discussion of the results of measurements of electrical resistivity for materials under applied pressure extending over a range in pressures from 0 to 27 GPa and temperatures from 1 to 300 K. The primary effect of applying pressure to a solid is to reduce the interatomic distance and to increase the overlap of the electronic orbitals. The secondary effects of applying pressure to a solid include the delocalization of electrons and a broadening of the energy bands. In addition, the application of pressure can induce a variety of transitions, both electronic and structural. Some of the phenomena observed during the pressure experiments reported in this dissertation include the pressure-induced enhancement of the superconducting transition temperature in a recently discovered class of bismuth-sulfide layered superconductors, the anomalous “dome-like” behavior in the pressure dependence of the Néel temperature in the first-known synthesis of an itinerant antiferromagnetic metal with non-magnetic constituents TiAu, and the evolution of the pressure-induced first-order transition to antiferromagnetism in the Fe-substituted heavy fermion compound URu_2Si_2. These and other results including a semiconductor-metal transition in the normal state of one of the bismuth-sulfide layered superconducting compounds are a consequence of the electronic and structural transitions that can occur as a result of the application of pressure. The theoretical context for the experimental results includes a discussion of the effect of pressure on the relevant parameters in condensed matter theory including the density of states, the exchange interaction in both the localized and itinerant models of magnetism, and the electron-phonon coupling parameter, among others. In particular, the pressure dependence of the magnetic ordering temperature and the superconducting transition temperature in various materials can be explained in terms of how the few parameters listed above respond to pressure.

Chapter 1

Introduction

In 1935, Eugene Wigner and Hillard Bell Huntington proposed the possibility of achieving a metallic phase of hydrogen that would exceed the density of ordinary molecular solid hydrogen.[1] Wigner and Huntington concluded that an atomic lattice of metallic hydrogen would be stable under a pressure of approximately 25 gigapascals (GPa).[1] Unfortunately, the pressure techniques available at that time would only allow for experiments up to about 10 GPa. Furthermore, the predicted amount of pressure at 25 GPa was a gross underestimate of the megabar pressures that would be required to achieve solid metallic hydrogen. More than thirty years later in 1968, the prospect of achieving a metallic phase of solid hydrogen under the application of extreme pressure became more intriguing upon the suggestion by Neil W. Ashcroft that the proposed Wigner-Huntington phase of metallic hydrogen would become a superconductor at elevated temperatures.[2]

During the last few years, new developments in the science of materials under pressure have afforded researchers the opportunity to witness groundbreaking phenomena such as the long-standing prediction of the Wigner-Huntington phase of atomic metallic hydrogen at a pressure of $P \sim 500$ GPa.[3] Other notable developments include the recent

---

[1] Pressure in this document is expressed primarily in units of GPa. 1 GPa = 10 kilobar (kbar) $=10^3$ bar and 100 GPa = 1 megabar (Mbar) = 10^6 bar.

observation in 2015 of a record-breaking superconducting transition in hydrogen-sulfide with a $T_c \sim 200$ K at a pressure of $P = 150$ GPa.[4] As shown in Fig. 1.1, the upper limit on static pressures realized in experiments on materials has steadily grown orders of magnitude over the last 60 years from the kilobar ($>$ 10 GPa) range to the several megabar ($>$ 100 GPa) range. Recent advances in diamond anvil cell (DAC) technology are pushing static laboratory pressures toward the terapascal (1000 GPa) range.[5] At these unprecedented pressures, entirely new states of matter, both unforeseen and long-awaited, are being created in materials and are fast becoming available to researchers for investigation.

Indeed, high-pressure measurements in condensed matter research are useful and perhaps best known for creating and studying new and exotic states of matter. However, the application of external pressure is equally useful in studying small and continuous variations of a particular physical property or parameter within a single phase. The primary effect of pressure on a material is to change the interatomic distance through a reduction of volume. A secondary effect of pressure to be discussed in more detail in Chapter 2 is the effect of the change in interatomic distance on key parameters in condensed matter theory such as the density of states, magnetic exchange interactions, electron-phonon coupling (or other pairing interactions), and energy bandwidths and energy-band gaps, among others. Even at modest values, the application of pressure can have drastic effects on the superconducting and magnetic properties of correlated-electron materials.

The most common measurement made on metals at high pressure is the measurement of electrical resistivity, ρ.[7] All of the measurements discussed in this dissertation are exactly that, with the distinction being that not all of the materials studied are metals. The pressure experiments were performed at relatively low values of pressure that range from ambient pressure ($\sim$ 0 GPa) to $\sim$ 27 GPa using a variety of pressure cells including a hydrostatic piston-cylinder cell (PCC), a Bridgman anvil cell (BAC), and a diamond anvil cell (DAC).

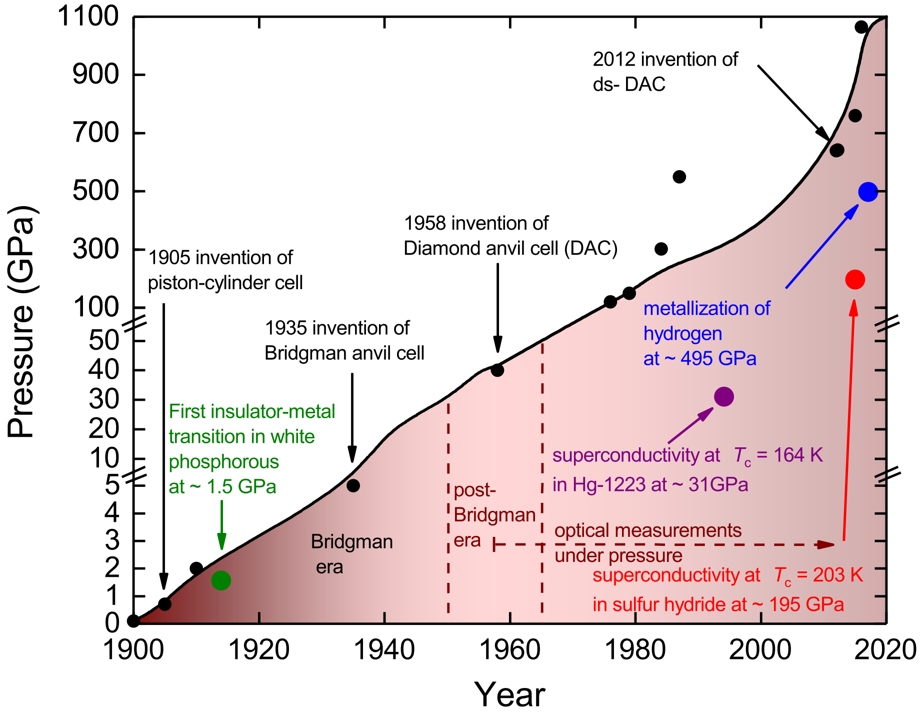

Figure 1.1: A chronology of the more important pressure techniques and static pressures available to researchers over the last 120 years. The Bridgman era spans the years from 1905 to 1950 during which P. W. Bridgman developed the piston-cylinder and opposed-anvil pressure cell techniques for the specific purpose of measuring electrical resistivity of materials under pressure. In the post-Bridgman era (roughly 1950 to 1965), H. G. Drickamer led developments in high-pressure supported anvil devices for both electrical resistance and spectroscopic measurements of materials under pressures up to hundreds of kilobars (10∼70 GPa).[6–8] Concurrent to the developments led by Drickamer during the post-Bridgman era was the birth of the diamond anvil cell (DAC) technique in 1958 and its subsequent development which revolutionized materials research under pressure. The DAC apparatus is small enough to fit into the palm of a hand making it possible for larger numbers of researchers to conduct sophisticated investigations of materials under extremely high pressures approaching 100 GPa and beyond.[6, 9] Recent advances in DAC technology making use of extremely strong laboratory grown nanocrystalline diamond is now allowing for controlled static pressure experiments known as double-stage DAC (ds-DAC) experiments that are approaching the terapascal (1000 GPa) range.[5] The smaller black circles indicate the upper limit of static pressures realized in experiments for a particular year (or period).[5, 9–17] The larger circles in color are notable experiments under pressure.[3, 4, 18, 19] The black curve is a guide to the eye. (Note the break in the vertical axis at 5 and 50 GPa.)

Outline of the dissertation

In this opening chapter, a brief description was given regarding the basic effects of pressure on materials and its importance in studying the properties of condensed matter. A brief outline and description of the contents of the remaining chapters in this thesis is as follows: Chapter 2 provides a more detailed description of the manner in which applied external pressure may affect the correlated-electron phenomena observed in the materials discussed in later chapters of this thesis. While the primary effect of pressure is to reduce the interatomic spacing, the emphasis of the discussion in Chapter 2 is on the secondary effects of pressure on some of the key parameters in condensed matter physics. Chapter 2 opens with a discussion of the effect of pressure on the electronic-band structure of a solid and in particular how pressure can reduce the energy-band gap in non-metals and induce a non-metal to metal transition. The discussion in Chapter 2 continues with the effects of pressure on magnetism in both the localized model and also in the itinerant-electron limit. In general, the application of pressure has the effect of weakening magnetism, but there are exceptions. One such exception is the itinerant magnet discussed in the last chapter of this thesis. Of particular interest to the subject of the effect of pressure on magnetism is a discussion of the results of the systematic investigations of dilute magnetic alloys under pressure in the 1960s and 1970s.[20] These pressure experiments were fruitful in that they provided a quantitative treatment of the response of the exchange interaction parameter $\mathscr{J}$ (in the localized moment model) to pressure in the limit of weak to moderate hybridization of the localized impurity d and f-electrons with the conduction electrons of the host matrix. The discussion of magnetism under pressure in Chapter 2 concludes with the effects of pressure on ferromagnetism in the itinerant-electron model that is useful in describing the d-band systems composed of transition metal elements. This part of Chapter 2 relates to the pressure study described in Chapter 7 of this thesis regarding the recently discovered itinerant antiferromagnetic alloy TiAu. Although there is no current theory of itinerant antiferromagnetism on par with the model of itinerant ferromagnetism developed by Felix Bloch and Edmund Stoner,[21–26] the discussion of d-band magnetism serves as a good starting point for understanding the itinerant antiferromagnetism in TiAu and its response to pressure. Chapter 2 concludes with a discussion of superconductivity under pressure, with a particular emphasis on the pressure (or volume) dependence of the superconducting transition temperature T_c in various classes of superconductors including simple s- and p-electron metal conventional superconductors and the layered high-T_c cuprate-oxide superconducting materials. Chapter 3 presents the experimental details involved in performing measurements of electrical resistivity of materials under pressure. The techniques of applying high-pressure with the various pressure-cells including the hydrostatic piston-cylinder cell, the Bridgman anvil cell, and the diamond anvil cell will be discussed. Consideration is given to the degree to which a (non-)hydrostatic environment can affect the measurement of a particular physical property. Manometry (or the method by which pressure is measured in a pressure cell) as well as thermometry will be discussed. The remainder of the thesis (Chapters 4, 5, 6, and 7) includes the results and discussion of pressure experiments on some rather fascinating materials, both structurally and compositionally. In Chapters 4 and 5, the results of pressure experiments on the novel class of layered superconducting materials $Ln\mathrm{O}_{1-x}\mathrm{F}_x\mathrm{BiS}_2$ (with Ln = La, Ce, Pr, Nd and x = 0.5) are discussed. The measurements of electrical resistivity under pressure reveal a pressure-induced enhancement of superconductivity from a low-T_c phase to a high-T_c-phase. The rapid enhancement of T_c with pressure is the result of a pressure-induced structural phase transition at ambient temperature. These superconducting materials are of particular interest in that they share a similar layered structure to the high-T_c layered superconductors and present an additional opportunity for the study of structural effects in layered superconducting materials. In Chapter 6, the effect of pressure on the Fe-substituted heavy-fermion compound $\mathrm{URu_2Si_2}$ is discussed. This study reveals the remarkable similarity between the effects of chemical pressure P_{ch} (due to the iso-electronic substitution of smaller Fe ions for Ru ions) and externally applied pressure P on the ordered phases of this unique compound. As mentioned previously, the last chapter of the thesis includes a discussion of the results of the effects of pressure on the recently discovered itinerant antiferromagnetic metal TiAu in which there is an anomalous pressure-induced enhancement of the Néel temperature from $T_N \simeq 33$ K at ambient pressure to a maximum of $T_N \simeq 35$ K occurring at $P \sim 5.5$ GPa. This material is unique in that it is the only known itinerant-electron antiferromagnet with non-magnetic constituent elements.

Blbliography

[1] E. Wigner and H. B. Huntington, “On the Possibility of a Metallic Modification of Hydrogen”, J. Chem. Phys. **3**, 764–770 (1935).

[2] N. W. Ashcroft, “Metallic Hydrogen: A High-Temperature Superconductor?”, Phys. Rev. Lett. **21**, 1748–1749 (1968).

[3] R. P. Dias and I. F. Silvera, “Observation of the Wigner-Huntington transition to metallic hydrogen”, Science **355**, 715–718 (2017).

[4] A. P. Drozdov, M. I. Eremets, I. A. Troyan, V. Ksenofontov, and S. I. Shylin, “Conventional superconductivity at 203 kelvin at high pressures in the sulfur hydride system”, Nature **525**, 73–76 (2015).

[5] N. Dubrovinskaia, L. Dubrovinsky, N. A. Solopova, A. Abakumov, S. Turner, M. Hanfland, E. Bykova, M. Bykov, C. Prescher, V. B. Prakapenka, S. Petitgirard, I. Chuvashova, B. Gasharova, Y.-L. Mathis, P. Ershov, I. Snigireva, and A. Snigirev, “Terapascal static pressure generation with ultrahigh yield strength nanodiamond”, Sci. Adv. **2** (2016).

[6] A. Jayaraman, “Diamond anvil cell and high-pressure physical investigations”, Rev. Mod. Phys. **55**, 65–108 (1983).

[7] H. Drickamer, “The Effect of High Pressure on the Electronic Structure of Solids”, Solid State Physics **17**, 1–133 (1965).

[8] H. Drickamer, R. Lynch, R. Clendenen, and E. Perez-Albueene, “X-Ray Diffraction Studies of the Lattice Parameters of Solids under Very High Pressure”, Solid State Physics **19**, 135–228 (1967).

[9] W. A. Bassett, “Diamond anvil cell, 50th birthday”, High Pressure Res. **29**, 163–186 (2009).

[10] R. M. Hazen, *The Diamond Makers* (Cambridge University Press, New York, 1999).

[11] P. F. McMillan, “Pressing on: The legacy of Percy W. Bridgman”, Nat. Mater. **4**, 715–718 (2005).

[12] H. K. Mao and P. M. Bell, “High-Pressure Physics: The 1-Megabar Mark on the Ruby R1 Static Pressure Scale”, Science **191**, 851–852 (1976).

[13] H. K. Mao and P. M. Bell, “Equations of state of MgO and ε-Fe under static pressure conditions”, J. Geophys. Res.: Solid Earth **84**, 4533–4536 (1979).

[14] P. M. Bell, H. K. Mao, and K. Goettel, “Ultrahigh Pressure: Beyond 2 Megabars and the Ruby Fluorescence Scale”, Science **226**, 542–544 (1984).

[15] J. A. Xu, H. K. Mao, and P. M. Bell, “High-Pressure Ruby and Diamond Fluorescence: Observations at 0.21 to 0.55 Terapascal”, Science **232**, 1404–1406 (1986).

[16] I. Kantor, V. Prakapenka, A. Kantor, P. Dera, A. Kurnosov, S. Sinogeikin, N. Dubrovinskaia, and L. Dubrovinsky, “BX90: A new diamond anvil cell design for X-ray diffraction and optical measurements”, Rev. Sci. Instrum. **83**, 125102 (2012).

[17] Dubrovinsky, L. and Dubrovinskaia, N. and Bykova, E. and Bykov, M. and Prakapenka, V. and Prescher, C. and Glazyrin, K. and Liermann, H. -P. and Hanfland, M. and Ekholm, M. and Feng, Q. and Pourovskii, L. V. and Katsnelson, M. I. and Wills, J. M. and Abrikosov, I. A., “The most incompressible metal osmium at static pressures above 750 gigapascals”, Nature **525**, 226–229 (2015).

[18] P. W. Bridgman, “Change of Phase under Pressure. I. The Phase Diagram of Eleven Substances with Especial Reference to The Melting Curve”, Phys. Rev. **3**, 153–203 (1914).

[19] L. Gao, Y. Y. Xue, F. Chen, Q. Xiong, R. L. Meng, D. Ramirez, C. W. Chu, J. H. Eggert, and H. K. Mao, “Superconductivity up to 164 K in $\mathrm{HgBa_2Ca}_{m-1}\mathrm{Cu}_m\mathrm{O}_{2m+2+\delta}$ $(m = 1, 2, \mathrm{and} 3)$ under quasihydrostatic pressures”, Phys. Rev. B **50**, 4260–4263 (1994).

[20] J. S. Schilling, “Pressure as a parameter in the study of dilute magnetic alloys”, Adv. Phys. **28**, 657–715 (1979).

[21] F. Bloch, “Bemerkung zur Elektronentheorie des Ferromagnetismus und der elektrischen Leitfähigkeit”, Zeitschrift für Physik **57**, 545–555 (1929).

[22] E. C. Stoner, “Collective Electron Ferromagnetism”, Proc. Roy. Soc. A **165**, 372–414 (1938).

[23] E. C. Stoner, “Collective Electron Ferromagnetism. II. Energy and Specific Heat”, Proc. Roy. Soc. A **169**, 339–371 (1939).

[24] E. C. Stoner, “Collective Electron Specific Heat and Spin Paramagnetism in Metals”, Proc. Roy. Soc. A **154**, 656–678 (1936).

[25] E. C. Stoner F.R.S., “Ferromagnetism”, Rep. Prog. Phys. **11**, 43 (1947).

[26] C. Herring, “Vol. 4: Exchange Interactions among Itinerant Electrons”, in *Magnetism*, edited by G. T. Rado and H. Suhl (Academic Press, New York, 1966), pp. 1–407.

Chapter 2

Background: Theory and Experiment

2.1 Solids under applied pressure

The pressure experiments reported herein are measurements of the electrical resistivity of solids under applied pressure and over a range of temperature extending from room temperature down to one degree Kelvin. Of the thermodynamic variables including entropy S, temperature T, pressure P, volume V, and particle number N, only P, T, and N are directly controlled by the experimentalist. The defining equation of pressure P is often given as a change in energy with respect to a change in volume:

$$P = -(\partial U/\partial V)_{S,N} \tag{2.1}$$

or

$$P = -(\partial F/\partial V)_{T,N} \tag{2.2}$$

where U in Equation 4.1 is the internal energy of the system and F in Equation 2.2 is the Helmholtz free energy. The particle number N is set from the beginning of the experiment during sample synthesis and is constant throughout the experiment. The experimentalist is able to control the temperature T, but has no control over the entropy S, and so the definition of pressure P, in the form given in Equation 2.2, is more appropriate in this context where P, T, and N are directly in control of the experimentalist and can be held constant if needed. From this point forward, the subscript N will be dropped since it does not change during the measurement of electrical resistivity ρ, under applied pressure. Using the thermodynamic relation $F = U - TS$, the Maxwell relation $(\partial S/\partial V)_T = (\partial P/\partial T)_V$, and noting that $(\partial T/\partial V)_T = 0$, it is possible to rewrite the definition of pressure P, in Equation 2.2, as follows:

$$P = -(\partial U/\partial V)_T + T(\partial P/\partial T)_V \tag{2.3}$$

A brief description of the measurement of electrical resistivity for a sample under applied pressure reveals that the second term in Equation 2.3 can be ignored. After a sample of initial volume V_0, and particle number N, is wired for a measurement of electrical resistivity, the steps for the procedure of performing a measurement of electrical resistivity are performed in the following sequence: (1) pressure P is applied to the sample at room temperature and P is measured with the use of a manometer at either room temperature or low temperature; (2) the sample is held under constant pressure P as it is cooled down to low temperature in a clamped pressure cell; and (3) the electrical resistivity of the sample under constant pressure P is measured upon warming the sample up to room temperature. (Note that after the pressure has been applied to the sample at room temperature, there is a negligible change in both the volume V of the sample and the applied pressure P as the temperature T is changed.) Hence, the second term in Equation 2.3 may be neglected. This leaves a relationship between the pressure P, volume V, and internal energy U of the system at constant temperature T:

$$P = -(\partial U/\partial V)_T \tag{2.4}$$

The application of pressure to a solid material has the effect of perturbing or "tuning" the available energy levels of the outer-shell electrons of the atoms or molecules that make up the solid. The perturbation to the energy levels is primarily achieved through a change in the volume V, or a change to the interatomic spacing. In addition to the work done on the system during the application of pressure, the changes to the electronic orbital energies are reflected on a macroscopic scale (as shown in Equation 2.4) in the change of the bulk internal energy U of the system, as volume V is reduced. The interatomic spacing is fundamental to numerous other bulk physical properties of the condensed phase including electrical conductivity (or resistivity), local moment magnetism, itinerant magnetism, and (un)conventional superconductivity. It is important to mention that the change to the electronic structure of the system due to pressure is generally distinct from temperature effects, in which it is the relative occupancies of the electrons in the available energy levels that change while the energy levels themselves remain unchanged.[1] Alternatively, the basic effects of pressure are (1) to increase the overlap between neighboring electronic orbitals and (2) to affect the relative displacement of one type of orbital with respect to another. These two primary effects may lead to secondary effects such as the delocalization of electrons, broadening of energy bands in solids, and the closing of energy-band gaps, all of which are often associated with the various pressure-induced electronic transitions that occur in materials. Table 2.1 presents a classification of the types of pressure-induced transitions that can occur in solids. Some examples of pressure-induced phenomena observed in the materials discussed in later chapters of this dissertation are listed below each class of transition.

Table 2.1: Examples of the pressure-induced phenomena that occur in some of the materials investigated under pressure and discussed in later chapters in this dissertation. Classes of pressure-induced transitions (one through four) were adapted from Ref. [1].

Class 1	Class 2	Class 3	Class 4	Class 5
First order transition-negligible electronic component	First order transition-significant electronic component	Electronic transition-significant volume or structural change	Electronic transition-continuous	No transtion-continuous evolution of physical property
	hidden order→antiferromagnetic: URu_2Si_2 (Chapter 6) semiconductor→metallic: $NdO_{0.5}F_{0.5}Si_2$ (Chapter 5)	tetragonal→monoclinic with a low-T_c→high-T_c transition: $LaO_{0.5}F_{0.5}Si_2$ (Chapter 4)	antiferromagnetic→paramagnetic: itinerant antiferromagnet TiAu (Chapter 7)	increase in Kondo lattice coherence temperature: URu_2Si_2 (Chapter 6)

2.2 The effect of pressure on electrical resistivity

One of the defining characteristics of a metal is its high electrical conductivity, σ (or low electrical resistivity $\rho = 1/\sigma$). Values of electrical resistivity ρ for the known elements varies 23 orders of magnitude at ambient conditions (room temperature and atmospheric pressure). For metals such as copper and silver, $\rho \approx 1.6 \times 10^{-6}$ Ω·cm, while for insulators such as sulfur, $\rho \approx 1 \times 10^{17}$ Ω·cm. The elements of the periodic table are often grouped according to their electrical conductivity in seemingly well defined blocks of metals, semi-metals, semiconductors, and non-metals in a manner that coincides with the periodicity of the electronic valence structure of the atom. The natural boundary at ambient conditions between the metallic and non-metallic elements that is often highlighted in the periodic table is perhaps the most obvious yet intriguing example of a transition from the metallic to non-metallic phase.[2] However, the conventional boundaries between metallic and non-metallic behavior become blurred under conditions that deviate from ambient conditions, namely at high pressure and high temperature. In 1914, P. W. Bridgman was the first to observe an irreversible non-metal to metal transition in white phosphorous at an elevated temperature of 473 K and a pressure of $\sim$ 1.5 GPa.[3]

It is well known from the quantum theory of solids that the clear distinction between a metal and non-metal can be made from a determination of the band structure at a temperature of absolute zero (T = 0 K), at which point a metal conducts and a non-metal does not conduct.[4] Typically, the electronic band structure of a solid consists of a plot of the band energies as a function of the propagation vector $\mathbf{k}$ of the wavefunction for the Bloch electrons. The discussion in this dissertation is primarily concerned with the effect of pressure on the interatomic spacing in a crystal lattice and consequently how a change in the spacing between ions in a lattice affects the electronic band structure of a material and ultimately its electrical resistivity ρ.

A simple schematic illustrating the differences in band structure for metals, semi-

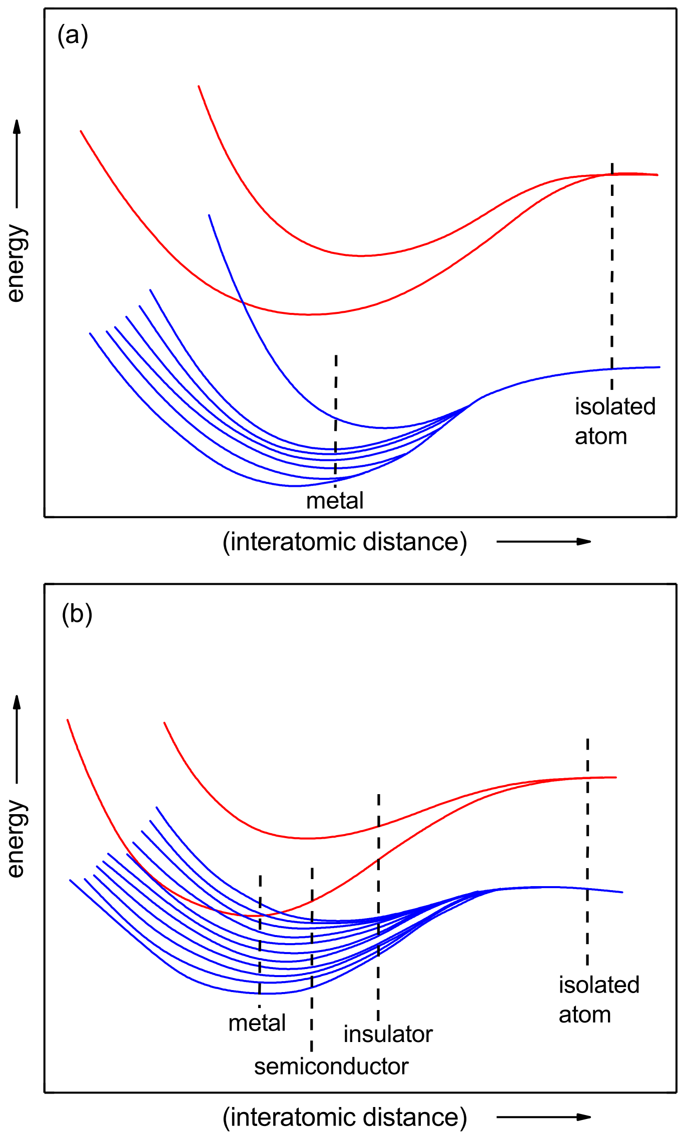

Figure 2.1: A simple schematic of the electronic energy levels in an atom (or lattice) plotted as a function of interatomic distance for (a) a monovalent metal and (b) a semiconductor or insulator. Figure adapted from Ref. [5].

conductors, and insulators is shown in Fig. 2.1 in which energy is plotted as a function of interatomic distance.[5] As the isolated atoms are brought closer together, and the interatomic distance is reduced to form the condensed phase, each of the discrete and well-separated energy levels of the free atoms are split into closely spaced energy bands (blue curves) that are well separated by large “forbidden” gaps of energy from the higher energy bands (red curves).[5] Figure 2.1 (a) represents the energy bands for isolated atoms containing only one electron in the highest occupied energy level. As the atoms condense, the degeneracy of the highest occupied energy level of all the isolated atoms is removed and only half of the available states are occupied within the closely spaced energy bands. Electrons are able to easily access the unoccupied states within the neighboring bands thus allowing the electrons to move through the crystal lattice as carriers of current. Figure 2.1 (b) represents the energy bands for isolated atoms containing two electrons in the highest occupied energy level. As the atoms condense, the degeneracy of the highest occupied energy level of the atom is removed. However, all of the available states are occupied within the closely spaced energy bands (blue curves) and the electrons are not able to easily access the unoccupied states of the higher energy bands (red curves), if the energy gap is too large compared to the thermal energy. This is the condition of the semiconductor or insulator.

The representation of the electronic band structure of a solid in Fig. 2.1 suggests that by applying pressure to a material, and thereby reducing the interatomic spacing in the crystal lattice, it is possible to force an insulator to metal transition. Indeed, high pressure investigations are well known for inducing insulator to metal transitions but are equally important in studying the continuous variation in electrical resistivity as the unit cell volume and interatomic spacing are reduced under applied pressure. Although the measurement of electrical resistivity ρ is a bulk measurement, and by itself cannot reveal the details of a complicated band structure (or Fermi surface), much can be learned about a material from the measurement of its electrical resistivity under pressure. Finally, we discuss the role of pressure in tuning the electrical resistivity of a material.

Based on the theory of electrical conduction proposed by Paul Drude in 1900, the electrical resistivity ρ, in the usual case where the charge carriers are electrons, is given as:

$$\rho = \frac{m}{n\tau e^2} \tag{2.5}$$

where m is the mass of the electron, n is the electron carrier density, e is the charge of the electron, and τ is the time between collision events for the electron and is known as the mean free time or relaxation time for the electron. It is instructive to write ρ in terms of its mobility μ:

$$\rho = \frac{1}{n\mu e} \tag{2.6}$$

where μ is given as $e\tau/m$. Both the electron carrier density n and the mobility μ are dependent on temperature T and pressure P. The electron mobility μ is typically reduced by the amount of scattering from the crystal lattice phonons and so it is expected that μ would decrease at higher temperature. However, the mobility is proportional to the Debye temperature Θ_D, where $\Theta_D \sim 1/V^{1/3}$, and therefore should increase as the volume V of the material is reduced with increasing pressure P. The effect of a pressure increase would then increase the carrier mobility μ causing a decrease in electrical resistivity $\rho \sim 1/\mu$. For insulators and semiconductors, the dominant factor in the electrical resistivity is the electron carrier concentration n. As temperature T increases, it is expected that n will also increase since the probability of exciting electrons to the bottom of the conduction band is given by the following exponential:

$$n \sim exp\left(-\frac{\Delta}{2k_BT}\right) \tag{2.7}$$

where k_B is the Boltzmann constant and Δ is the energy gap between the valence band (highest blue curve in Fig. 2.1 (b)) and conduction band (lowest red curve in Fig. 2.1 (b)). The reduction of the exponent by a factor of two in Equation 2.7 accounts for the fact that the location of the Fermi energy is in the middle of the energy gap Δ. This allows us to write the electrical resistivity as a function of temperature:

$$\rho(T) \sim \rho_0 e^{\Delta/2k_BT}, \tag{2.8}$$

where ρ_0 is a constant.

Figure 2.2 illustrates the effect of pressure on the semiconducting-like behavior that is observed in the normal-state electrical resistivity of the superconducting compound $LaO_{0.5}F_{0.5}BiS_2$. At a given pressure, the temperature dependence of the electrical resistivity $\rho(T)$ is well accounted for by the expression of $\rho(T)$ in Equation 2.8. As pressure is increased, the suppression of the semiconducting-like behavior is easily seen in the flattening of the $\rho(T)$ curves in Fig. 2.2 (a). From the expression of $\rho(T)$ in Equation 2.8, this is necessarily due to a reduction of the energy gap Δ between the valence and conduction bands. It is possible to extract the value of Δ from a plot of $\log(\rho)$ vs. $1/T$ as shown in Fig. 2.2 (b). The solid lines in Fig. 2.2 (b) represent linear fits of Eq. (2.8) from which the high- and low-temperature gaps Δ_1 and Δ_2, respectively, were determined and then plotted as a function of pressure P as shown in Fig. 2.2 (c). The clear suppression of the energy gap shown in Fig. 2.2 (c) is reversible with pressure and is a good example of the role pressure can play in extracting meaningful information from bulk measurements of physical properties such as electrical resistivity. The evolution of the energy gap Δ in the normal-state resistivity, with a change in pressure, is even more intriguing when one compares it to the pressure dependence of the superconducting transition temperature T_c. The correspondence between the normal state and superconducting properties of the $LaO_{0.5}F_{0.5}BiS_2$ compound and other superconducting compounds like it will be examined in more detail in Chapters 4 and 5 which contain the results and analysis from measurements of electrical resistivity under pressure for the novel class of superconducting materials $LnO_{0.5}F_{0.5}BiS_2$ (Ln = La, Ce, Pr, Nd).

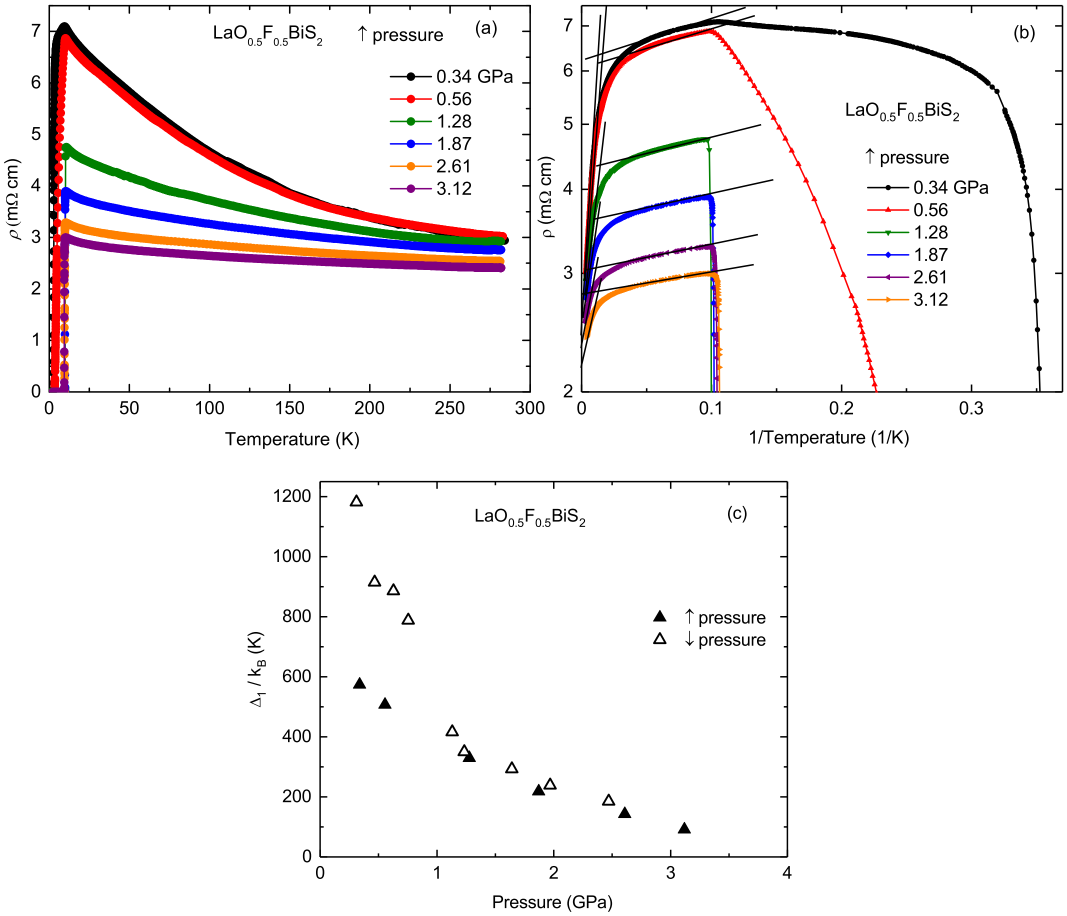

Figure 2.2: (a) Temperature dependence of electrical resistivity $\rho(T)$, for the $LaO_{0.5}F_{0.5}BiS_2$ sample at various pressures up to $P \sim 3$ GPa. As pressure P is increased from ambient pressure, the semiconducting-like behavior of $\rho(T)$ is suppressed as seen from the flattening of the curves at higher P. (b) $\log(\rho)$ vs. $1/T$ at various P for $LaO_{0.5}F_{0.5}BiS_2$. The solid lines represent linear fits of Eq. (2.8) to the data from which the high- and low-temperature gaps Δ_1 and Δ_2, respectively, were determined. (c) The high-temperature energy gap Δ_1 plotted as a function of pressure for $LaO_{0.5}F_{0.5}BiS_2$. Filled (open) symbols were obtained upon increasing (decreasing) pressure cycles.

2.3 The effect of pressure on magnetic order

In a recent study of osmium under high pressure, it was shown that at pressures over 770 GPa, osmium retained its hexagonal close packed (hcp) structure.[6] However, at about 440 GPa, the ratio of the c lattice parameter to the a lattice parameter (c/a ratio) exhibits an abrupt and anomalous decrease. The anomaly in the c/a ratio is explained as a result of a change in the polarizability of the atomic electron density due to the pressure-induced interactions between the low-lying, localized $5p$- and $4f$-core electrons for the Os atom (with electronic structure $[\mathrm{Kr}]4d^{10}5s^{2}5p^{6}4f^{14}5d^{6}6s^{2}$). Indeed, static high-pressure experiments are now being able to affect the core electrons of materials in the condensed phase, even for highly incompressible materials such as Os.

Experiments on materials under high pressure are well known for inducing magnetic to non-magnetic transitions and the overall effect of pressure through a reduction of volume is to reduce the magnetism in a solid. This applies to both local and itinerant magnetism. An increase in pressure (or reduction of volume) can lead to changes in the physical mechanisms responsible for magnetic order in solids including changes to local magnetic moments, energy bandwidths, density of states, exchange interactions, dipole-dipole interactions, crystal field effects, among others. It is suggested that the application of pressure can also lead to a crossover from local moment magnetism to itinerant or “band magnetism”.[7] In this section, we look at the relevant effects of pressure on local magnetism and itinerant magnetism with specific attention given to the effect of pressure on magnetic moments, density of states, and exchange interactions. In particular, it will be emphasized that the response of the exchange interaction to pressure is the primary reason for a reduction in magnetism in materials over an extended range in pressure. In Chapter 7, the results of pressure experiments on the recently discovered itinerant antiferromagnetic metal TiAu will be discussed.

2.3.1 Local moment magnetism

The properties of a class of materials known as dilute magnetic alloys are well suited for the investigation of local moment magnetism. A dilute magnetic alloy is formed by introducing small quantities of magnetic impurities into a non-magnetic metallic host with the intent that the impurity ion will retain its magnetic moment but at the same time have a negligible long-range interaction with the other magnetic impurities in the system. Such a system allows for an investigation of the interaction of the magnetic impurity ion with its immediate short-range environment, namely the interaction with the conduction electrons of the metallic host. At higher concentrations of magnetic impurities, additional interactions between the magnetic impurities themselves must be considered. The application of pressure is sometimes used as a diagnostic in not only determining the relative importance of the various interactions over large ranges in magnetic impurity concentration, but also in determining whether the magnetic order is itinerant or localized. This is possible due to the fact that each of the interactions (i.e., the exchange interaction between the conduction electron spin-density and the localized moment of the magnetic impurity ion, the direct exchange interaction between localized moments, superexchange, RKKY-exchange, and the dipole-dipole interaction) responds to pressure in a unique and identifiable way that is reflected in the overall response of the magnetic ordering temperature T_0 to an increase in applied pressure.[7] The next sections attempt to present a physical representation for the interaction between the localized magnetic moment and the spin density of the surrounding conduction electrons. The goal of the discussion will be to clarify the effect of applied pressure on local magnetic behavior and how pressure, in a large number of cases, ultimately weakens magnetic order in a solid.

In general, it is the core electrons of an atom that give rise to the magnetic moment of an atom and magnetism in a solid. A simple prerequisite for the existence of local magnetism is a partially filled inner atomic shell. As suggested by the recent study of Os under high pressure,[6] the application of pressure on the order of one terapascal (or 1000 GPa) would start to affect the properties and interactions of the inner-shell electrons of the atoms in the condensed phase. Further increases in pressure to values greater than P $\sim$1000 terapascal (or $> 10^6$ GPa) would be enough to progressively break up the electron shell structure of the atoms in a solid, eventually leaving only bare nuclei surrounded by

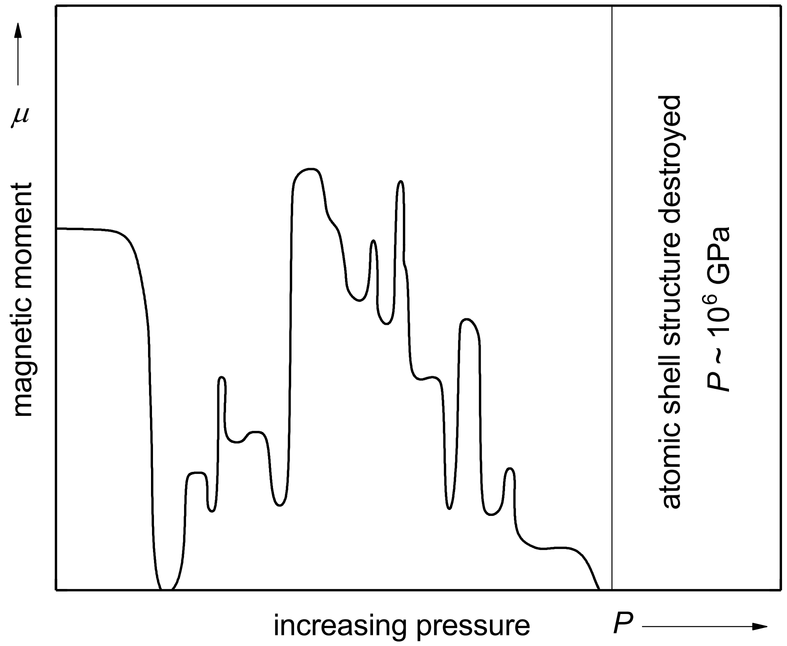

Figure 2.3: A schematic of the magnetic moment μ as a function of increasing applied pressure P in a solid. As pressure is increased, the magnitude of the moment rises and falls as the core electrons are squeezed out of the atomic shell. At high enough pressure $P \sim 10^6$ GPa, the atomic shell is destroyed as all of the core electrons are removed from the atom forming a Thomas-Fermi electron gas around the bare nuclei. Figure adapted from Ref. [8].

an electron gas. After the last electron has been squeezed out of the innermost shell, there would be no opportunity for the existence of local moment magnetism (ignoring the small magnetic moments of the nuclei).[8] Figure 2.3 is a schematic representation of the change in the magnetic moment μ of an atom in the condensed phase with an increase in applied external pressure P. As pressure is increased, the magnitude of the moment rises and falls as the core electrons are “squeezed out” of the atomic shell into the conduction band. The behavior of $\mu(P)$ in the righthand portion of Fig. 2.3, in which μ is reduced to zero, illustrates one way in which the application of pressure might suppress the magnetism in a solid. Although the local magnetism in a solid will reflect the temporary rise and fall of the local magnetic moment, as new shells are broken open and depleted, the overall effect of an increase in applied external pressure is to weaken the bulk magnetism of the material. Even modest pressures on the order of $P \sim 1$ GPa can quickly destroy the magnetic order in a solid. Therefore, a consideration of the effect of pressure on other mechanisms at play in magnetic materials should be considered.

Stability of magnetic moments in solids

According to the Friedel-Anderson model,[9, 10] when a transition metal (T) ion, rare-earth (RE) ion, or actinide (A) ion with a partially-filled d- or f-electron shell is dissolved into a metallic host, the formation (or permanance) of a local magnetic moment is largely determined by the extent to which the localized d- or f-electron wave functions of the substituted ion hybridize with the conduction electron wave functions. If we introduce the concept of the lifetime τ of a localized electron in the d-electron shell of a T ion or f-electron shell of a RE ion, the long lifetime limit corresponds to weak to moderate mixing of the localized d or f electron with the conduction electrons. In this case, the electronic shell structure retains its highly-correlated atomic identity. Conversely, a short τ corresponds to strong hybridization between the d or f electrons and the conduction electrons, in which case, the local shell electronic structure loses its correlated atomic identity.[11] We can relate τ to the lifetime of the localized magnetic moment in a metallic host if we introduce the concept of a localized spin fluctuation lifetime τ_{sf} for the magnetic moment. It is expected that the τ_{sf} of the impurity ion is on the order of the lifetime τ.[11] This concept of a spin fluctuation lifetime τ_{sf} is a natural extension of the "valence fluctuation" model,[12–14] which uses the notion of temporal fluctuations between two integral valence states. This model can be used to explain the non-magnetic nature of Ce impurities which can exhibit a non-integral occupation of the Ce $4f$-shell.[15, 16] The solute impurity can be characterized as magnetic when τ_{sf} is large compared to thermal fluctuation lifetimes ($\tau_{sf} \gg \tau_{th} \sim h/k_BT$) and non-magnetic when τ_{sf} is small compared to thermal fluctuation lifetimes ($\tau_{sf} \ll \tau_{th}$).[11] In our discussion of the exchange interaction below, we will consider two cases in the magnetic limit in which the moment of the solute impurity is long lived ($\tau_{sf} \gg \tau_{th} \sim h/k_BT$): (1) antiferromagnetic exchange ($\mathscr{J} < 0$) and (2) ferromagnetic exchange ($\mathscr{J} > 0$). Here, $\mathscr{J}$ (discussed in more detail below), is the exchange interaction between the spin (or local moment) of a magnetic impurity embedded in a non-magnetic host and the local spin density of the conduction electrons near the impurity. Interestingly, the ferromagnetic and antiferromagnetic exchange interactions respond differently to the application of pressure and give rise to significantly different phenomena in their host metals. There is a third case that occurs in the non-magnetic (or weakly-magnetic) limit corresponding to solute moments with relatively short lifetimes. Any type of exchange interaction between the rapidly fluctuating, "non-existent" moment of the impurity ion and the spins of the conduction electrons is prohibited in this regime.[11] The lefthand portion of the $\mu(P)$ trendline in Fig. 2.3 is constant with increasing pressure and represents a long-lived ($\tau_{sf} \gg \tau_{th} \sim h/k_BT$) and stable local magnetic moment dissolved in a non-magnetic host. In this regime there is weak to moderate hybridization of the d or f electrons of the magnetic impurity ion with the conduction electrons of the non-magnetic host giving rise to an exchange interaction $\mathscr{J}$. In the next sections we will discuss the nature of the exchange interaction, its response to pressure, and its role in the disappearance of magnetic order in the bulk.

Exchange interaction

The simplest model of an exchange interaction between two particles with spin is canonically presented as a model of two independent electrons that gives rise to the Heisenberg exchange Hamiltonian:

$$H_{Heis} = -2\mathscr{J}\boldsymbol{s}_1 \cdot \boldsymbol{s}_2, \tag{2.9}$$

where $\boldsymbol{s}_1$ and $\boldsymbol{s}_2$ are the vector spin momentum operators for the electrons and $\mathscr{J}$ is the exchange constant which depends solely on the Pauli exclusion principle and the electrostatic repulsion between the electrons.[17] The form of this interaction favors parallel spin alignment between the two electrons when $\mathscr{J} > 0$ and its magnitude is much larger than the dipole-dipole interaction between the magnetic moments of the electrons which is often neglected. This exchange model can be extended to explain the interaction between the spin (or local moment) of a magnetic impurity embedded in a non-magnetic host and the local spin density of the conduction electrons near the impurity. When the local magnetic moments exhibit long lifetimes (as discussed above), the exchange Hamiltonian takes the form:

$$H_{ex} = -2\mathscr{J}\boldsymbol{S}\cdot\boldsymbol{s}, \tag{2.10}$$

where $\boldsymbol{S}$ is the spin of the paramagnetic impurity and $\boldsymbol{s}$ is the conduction electron spin density at the impurity site.[18] This Hamiltonian is suitable for conditions where the orbital angular momentum $\boldsymbol{L}$ of the impurity is quenched, as occurs for the case of $3d$ transition metal (T) impurities; however, for the case of RE impurities, $\boldsymbol{L}$ is in general non-zero and the spin of the paramagnetic impurity $\boldsymbol{S}$ is replaced by its projection onto the total angular momentum vector $\boldsymbol{J} = \boldsymbol{L} + \boldsymbol{S}$ in the ground state: $\boldsymbol{S} \rightarrow [\langle\boldsymbol{S}\cdot\boldsymbol{J}\rangle/J(J+1)]\boldsymbol{J}$. Hence, the exchange Hamiltonian in Equation 2.10 becomes:

$$H_{ex} = -2\mathscr{J}(g_J - 1)\boldsymbol{J}\cdot\boldsymbol{s}, \tag{2.11}$$

where g_J is the Landè g-factor for the Hund's rule ground state of the RE ion.[19]

The exchange interaction parameter $\mathscr{J}$ that appears in Equation 2.11 is generally expressed as the sum of two terms: $\mathscr{J} \simeq \mathscr{J}_0 + \mathscr{J}_1$. The ferromagnetic term $\mathscr{J}_0$ is positive ($\mathscr{J}_0 > 0$) which favors parallel alignment between the impurity spin and the conduction electron spin density at the impurity site, while $\mathscr{J}_1$ is an antiferromagnetic term ($\mathscr{J}_1 < 0$) that favors antiparallel alignment. As mentioned in Section 2.3.1, the ferromagnetic and antiferromagnetic exchange interactions both take place within the long lived limit, where the localized d- or f-electron shell of the impurity ion retains its atomic identity. The degree to which the d or f electrons hybridize with the conduction electrons determines whether $\mathscr{J}_0$ or $\mathscr{J}_1$ will be dominant.

In the case of moderate hybridization between the localized d- or f-electron states and conduction electron states, the exchange interaction is dominated by the antiferromagnetic term $\mathscr{J}_1$ causing an antiparallel orientation between the impurity spin and the spin polarization of the local conduction electron density. Hence, the localized magnetic moment of the impurity ion is quenched (or screened out) by the spin polarization of the surrounding conduction electron density leading to the Kondo effect. In the case of weak hybridization between the itinerant and localized electron states, the exchange interaction parameter $\mathscr{J}$ is dominated by the ferromagnetic (Heisenberg) exchange term $\mathscr{J}_0$. In the case of strong hybridization, the local moment is short-lived and unstable. In this case, the exchange interaction is all but non-existent and the exchange Hamiltonian in Equation 2.10 is no longer appropriate in describing the local moment magnetism.[11]

Negative exchange interaction ($\mathscr{J} < 0$) under pressure

Typically, dilute magnetic systems containing rare-earth impurity ions with unstable valence configurations (Ce, Pr, Sm, Eu, Tm, and Yb), transition metal impurity ions with partially-filled d-electron shells, or actinide impurity ions with partially-filled f-electron shells, tend to exhibit a moderate amount of mixing of the localized d- or f-electron states of the impurity ion with the conduction electron states. For these systems, the total effective exchange interaction $\mathscr{J}$ is dominated by the negative component $\mathscr{J}_1$. According to Schrieffer and Wolff,[20] the negative $\mathscr{J}_1$ term can be expressed in terms of the matrix mixing elements $\langle V_{kl}^2 \rangle$ in the Friedel-Anderson Hamiltonian [9, 10]:

$$\mathscr{J}_1 \sim -\frac{|V_{kl}^2|}{E_l} < 0, \tag{2.12}$$

where V_{kl} is the overlap integral for the localized impurity electron orbital wavefunction ϕ_l and the conduction electron wavefunction Ψ_k, and E_l is the energy separating the energy level of the localized impurity electron orbital and the Fermi energy level. Measurements of electrical resistivity on dilute magnetic alloys under pressure show that there is a universal increase in the magnitude of the effective exchange interaction $|\mathscr{J}|$ in the case of moderate hybridization where the effective exchange interaction is dominated by the $\mathscr{J}_1$ term. The physical mechanism for the increase in $|\mathscr{J}|$ with pressure P is unclear but the universal result for the dilute magnetic alloy systems suggests a common mechanism. Equation 2.12 suggests that the increase in $|\mathscr{J}_1|$ with increasing P arises from either an increase in the mixing matrix element $|V_{kl}^2|$ or a decrease in the separation energy E_l between the local magnetic level and the Fermi level, or both. Under the assumption that the decrease in separation energy E_l with applied pressure is primarily responsible for the increase in $|\mathscr{J}_1|$, it can be shown that $|\mathscr{J}_1|$ increases with a decrease in volume V according to:

$$d\ln|\mathscr{J}_1|/d\ln V = -2/3(E_f/E_l). \tag{2.13}$$

The energetics of a negative ($\mathscr{J} < 0$) exchange interaction as represented by the exchange Hamiltonian in Equation 2.10: $H_{ex} = -2\mathscr{J}\boldsymbol{S}\cdot\boldsymbol{s}$, dictate an antiparallel orientation of the impurity spin $\boldsymbol{S}$ and the spin polarization $\boldsymbol{s}$ of the local conduction electron density. This situation leads to the Kondo effect,[21–23] in which the localized magnetic moment (or spin) of the impurity ion is "quenched" by the spin polarization of the surrounding conduction electron density at temperatures below a characteristic temperature called the "Kondo temperature” T_K:

$$T_K \simeq T_f \exp[1/\mathscr{J}_1 N(E_f)], \tag{2.14}$$

where T_f is the Fermi temperature, $\mathscr{J}_1$ is the dominant component of the overall effective exchange interaction responsible for the Kondo effect, and $N(E_f)$ is the density of states at the Fermi energy E_f. It is the increase in the magnitude of $\mathscr{J}_1$ with pressure and that is predominantly responsible for the demagnetization of materials under applied external pressure. The negative exchange interaction is especially large when the energy of a bound state localized electron of the magnetic impurity approaches the Fermi energy, i.e., when the energy E_l required to move an electron from the impurity ion orbital to the Fermi level is small.

Positive exchange interaction ($\mathscr{J} > 0$) under pressure

While most dilute magnetic alloy systems exhibit an overall negative effective exchange interaction in the moderate hybridization regime, there are systems (i.e., LaGd) in the weak hybridization regime with an overall positive effective exchange interaction ($\mathscr{J} > 0$) that favors parallel alignment between the magnetic moment of the impurity ion and the spin-density of the conduction electrons and the core d and f electrons. For these systems, it was found that $|\mathscr{J}|$ decreases with pressure or $d\ln|\mathscr{J}|/d\ln V > 0$. Recall that the effective exchange interaction can be expressed as the competition between a positive and negative contribution $\mathscr{J} \simeq \mathscr{J}_0 + \mathscr{J}_1$. As pressure is increased, the $\mathscr{J}_0$ term may still be dominant if the hybridization is weak enough, but the overall effective exchange interaction may be reduced as $\mathscr{J}_1$ becomes more negative owing to the observed increase in $|\mathscr{J}_1|$ with pressure. In this case, a positive effective exchange interaction $\mathscr{J}$ would eventually pass through zero and become negative. Driving a weak hybridization regime toward a moderate hybridization regime with increasing pressure toward an ever increasingly negative exchange interaction is consistent with the overall tendency of magnetic systems to become non-magnetic with pressure. Moreover, a negative overall effective exchange interaction is an indication that the local magnetic impurity is becoming unstable and preparing to demagnetize. A further increase in pressure toward the strong hybridization regime where E_l approaches zero and the core d or f electrons move into the conduction band results in a destabilization of the local impurity moment.

The RKKY interaction and other magnetic exchange interactions under pressure

The exchange interaction described by the Hamiltonian in Equation 2.10 for the interaction between the spin $\boldsymbol{S}$ of a local impurity ion and the spin density $\boldsymbol{s}$ of the conduction electrons can set up a spatial oscillation in the spin-density polarization of the conduction electrons that can interact with the spin $\boldsymbol{S}'$ of a second local impurity ion. This is a long-range interaction between the localized magnetic moments that typically occurs in systems with higher concentrations of magnetic impurities. This type of indirect exchange interaction commonly known as the RKKY (Ruderman-Kittel-Kasuya-Yosida) exchange interaction [24–26] is among the various additional interactions that may occur between localized magnetic moments that can create magnetic order. Other types of magnetic exchange interaction include the direct exchange between the magnetic impurities themselves due to an overlap of their wavefunctions, the superexchange interaction, in which the magnetic ions can interact with each other through their mutual overlap with the electron wavefunctions of non-magnetic ions, and the dipole-diploe interaction between localized magnetic moments, among others. Each of these mechanisms changes with pressure in its own unique and measurable way such that by measuring the evolution of the magnetic ordering temperature with increasing pressure, it is possible to identify the dominant interaction responsible for the magnetic ordering.[8]

For many systems, it turns out that for the RKKY interaction, the effective exchange interaction parameter $\mathscr{J}_{RKKY}$ is dominated by the magnitude of the negative ex-

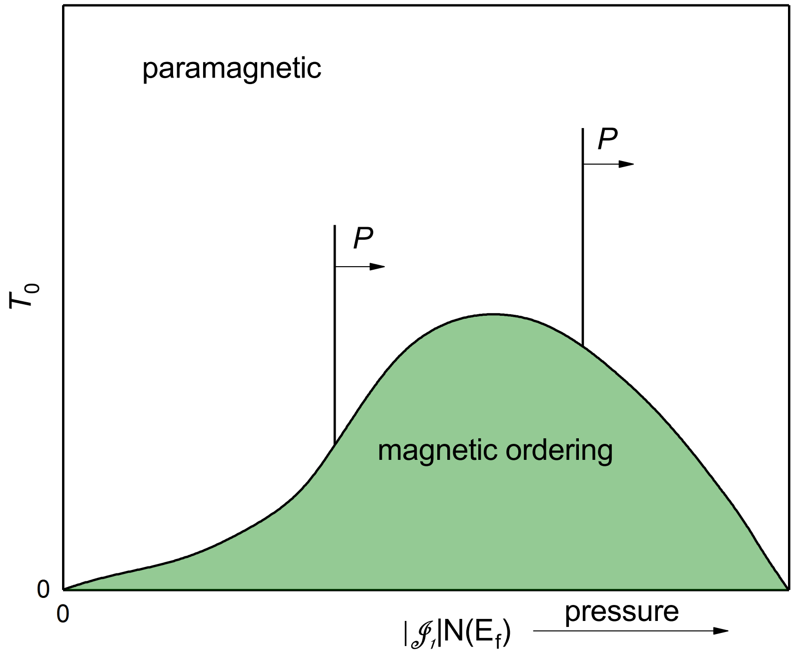

Figure 2.4: A schematic of the magnetic ordering temperature T_0 as a function of $|\mathscr{J}_1|N(E_f)$. An increase in the applied pressure P has the effect of increasing $|\mathscr{J}_1|$. (Here, $N(E_f)$ is assumed to have a small pressure dependence.) Depending on the value of $|\mathscr{J}_1|N(E_f)$ at ambient pressure, the initial effect of an increase in pressure may be to enhance the magnetic order but the ultimate effect of pressure on a system is to suppress the magnetic ordering temperature. Figure adapted from Ref. [8].

change component $\mathscr{J}_1$. As discussed above, this is also the case for the exhange interaction that occurs for a moderate hybridization between the localized impurity wavefunctions and the conduction electron wavefunctions. In the case of the RKKY interaction, the functional dependence of the magnetic ordering temperature T_0 on the exchange parameter $\mathscr{J}_1$ is given as:

$$T_0 \sim \mathscr{J}_1^2 N(E_f). \tag{2.15}$$

Hence, for a negligible pressure dependence observed for $N(E_f)$ and a positive pressure coefficient for the magnitude of the exchange interaction parameter $|\mathscr{J}_1|$, one would expect to observe an increase in the magnetic ordering temperature T_0 at modest pressures if the RKKY interaction was the dominant exchange interaction. The effect on magnetic order due to the competition between the RKKY interaction and the Kondo interaction (in which there is a "quenching" of the local magnetic moments under moderate hybridization with the conduction electrons) can be summarized in the phase diagram shown in Fig. 2.4.[27] It is easy to see that the overall effect of an increase in pressure is to increase the magnitude of the exchange interaction parameter $|\mathscr{J}_1|$ toward the right, thereby ultimately having a negative impact on the magnetic order. However, depending on the ambient pressure value of $|\mathscr{J}_1|N(E_f)$, it is possible for the magnetic ordering temperature T_0 to either monotonically decrease with pressure or to first pass through a maximum before decreasing with pressure.[8]

2.3.2 Itinerant magnetism

The general tendency of pressure to destroy magnetism in solids is well accounted for by the localized-spin model whereby the magnitude of the exchange interaction parameter $|\mathscr{J}_1|$ (where $\mathscr{J}_1 < 0$) increases with decreasing volume V, leading to "quenched" or compensated magnetic moments of the magnetic impurity ions in dilute magnetic alloys. While the $4f$-shell electrons of rare-earth ions tend to retain their localized atomic character thus leading to direct and indirect exchange interactions, experiments indicate that the $3d$ electrons in transition metals and transition metal alloys exhibit high mobility with band-like characteristics. The magnetism in these systems is perhaps better described by an itinerant-electron model rather than a localized-electron picture of magnetism. Furthermore, magnetovolume effects (or the magnetic response to pressure) seem to be particularly well described by the itinerant electron picture.[28]

The itinerant picture of ferromagnetism was built on the early theory of Felix Bloch in 1929,[29] who demonstrated (in the Hartree-Fock approximation[1]) that a free-electron

---

[1] A many body wave-function in a free-electron gas can be written as a product (or determinant) of non-interacting single-particle electron wave-functions in which the coordinate exchange of any two electrons

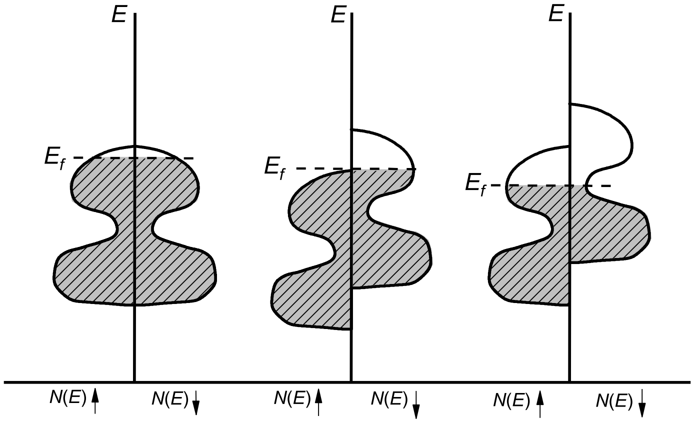

Figure 2.5: A schematic representation of the partially depleted $3d$ band: (a) paramagnetism (b) strong ferromagnetism (c) weak ferromagnetism with typical variation of $N(E)$ as observed in transition element metals (or alloys). Figure adapted from Ref. [28].

gas at sufficiently low-density would exhibit ferromagnetism. The development of the theory of itinerant-electron magnetism is essentially an attempt at replacing the low-density free-electron theory proposed by Bloch with a theory that is more appropriate for $3d$-band electrons in transition metal elements. Edmund Stoner in the 1930s,[30–32] and later Erich P. Wohlfarth in the 1950s,[33] suggested that various properties of metallic systems including non-integral magnetic moments, electronic specific heat, magnetic ordering temperature, and paramagnetism could be described by just a few parameters such as the density of states $N(E_f)$, and the exchange interaction energy $\mathscr{E}$.

The large spatial extent of the $3d$ wavefunctions in transiton metal elements and alloys suggests that as isolated atoms are brought closer together in the condensed phase, the $3d$-electron orbitals of the independent atoms broaden into "delocalized" energy bands.

---

introduces a negative sign in the product.

The highly mobile $3d$ electrons may also move through the crystal lattice similar to conduction electrons. The degree to which the energy bands are broadened is inversely proportional to the interatomic spacing so that for a smaller separation between atoms, the larger the bandwidth of the $3d$ energy bands. If the $3d$ band is partially filled (less than ten $3d$ electrons per atom), there are several possibilities for the manner in which the $3d$ spin sub-bands are populated. Figure 2.5 displays a schematic representation of the density of states $N(E)$ of a partially depleted $3d$ energy band in a typical transition metal element or alloy. Generally, there is a large density of states $N(E)$ at the lower part of the $3d$ bandwidth which then passes through a maximum at slightly higher energy levels. In the higher energy region, the value of $N(E)$ then begins to decrease to a minimum before returning to larger values at the highest energy region within the band.[34]

The change in energy ΔE associated with moving a $3d$ electron from one spin sub-band to the other spin sub-band depends on the increase in the kinetic energy $\mathscr{K}$ of the $3d$ electron relative to the decrease in energy owing to the effective exchange interaction energy $\mathscr{E}$ between the $3d$ electrons. Fig. 2.5 (a) represents a depleted $3d$ band in which there is no preference for the population of one spin band over the other. The Fermi energy is lower than the top of each of the $3d$ spin sub-bands such that energy states above E_f are unoccupied. However, the value of the exchange interaction energy $\mathscr{E}$ is too small to produce a shift in the $3d$ spin sub-band populations. In this case, there is no magnetic moment associated with the $3d$ band, and the bulk of the sample exists in the paramagnetic phase. If the value of $\mathscr{E}$ is large enough, it is energetically favorable for a redistribution of the electrons among the $3d$ spin-sub bands such that there is a shift of the spin sub-bands relative to the Fermi energy E_f as shown in Fig. 2.5 (b) and (c). The redistribution of electrons or shift in the spin sub-bands gives rise to a non-zero magnetic moment in the $3d$ band which is determined from the difference between the number of spin-up electrons and spin-down electrons over all values of energy within the $3d$ band: $\Sigma_E(N(E)_\uparrow - N(E)_\downarrow)$. This is also represented by the difference in the shaded areas. The non-zero magnetic moment in the 3*d* band leads to an overall ferromagnetic phase in the system. In Fig. 2.5 (b), the situation in which the majority spin sub-band is completely occupied (or saturated) is sometimes referred to as strong itinerant ferromagnetism. In a weak itinerant ferromagnet, both 3*d* spin sub-bands are not saturated as depicted in Fig. 2.5 (c).

The Stoner criterion for 3*d*-band ferromagnetism

The change in energy for a spin-down electron to move into the spin-up band (or vice versa) is given by the following expression:

$$\Delta E \sim \frac{(n_\uparrow - n_\downarrow)^2}{N(E_f)}[1-\mathscr{E}N(E_f)], \tag{2.16}$$

where $n_\uparrow$ and $n_\downarrow$ are the number of electrons in each spin state. For $[1-\mathscr{E}N(E_f)] > 0$, the lowest value for the energy change requires that $(n_\uparrow - n_\downarrow) = 0$ and that the system is then non-magnetic. For the case where $[1-\mathscr{E}N(E_f)] < 0$, the 3*d* energy band is now split as depicted in Fig. 2.5 (b) and (c), leading to a non-zero magnetic moment in the 3*d* band and an overall ferromagnetic phase in the system. Hence, the conditions that favor ferromagnetic order in this simplified representation of an itinerant system include: (1) a large value of the exchange interaction energy $\mathscr{E}$ and (2) a large value of the density of states at the Fermi energy $N(E_f)$. The $[1-\mathscr{E}N(E_f)] < 0$ condition (or equivalently $\mathscr{E}N(E_f) > 1$) is known as the Stoner criterion for the occurrence of ferromagnetism at T=0 K in an itinerant magnet with 3*d* bands.[35]

Pressure effects in 3*d* itinerant-electron magnets

The pressure dependence of the magnetic ordering temperature T_C in an itinerant ferromagnet allows for the study of the effect of the interatomic distance on the magnetic coupling between the $3d$ moments. In a low-density free-electron gas of volume V, the volume dependence of the density of states at the Fermi energy is $N(E_f) \sim V^{2/3}$, while the volume dependence of the exchange interaction energy is $\mathscr{E} \sim V^{-1/3}$, leading to the volume dependence for the product, $\mathscr{E}N(E_f) \sim V^{1/3}$, which decreases with increasing external pressure.[29] Hence, a decrease in $\mathscr{E}N(E_f)$ with an increase in pressure reduces the likelihood of meeting the Stoner criterion for ferrromagnetism. The general result for a free-electron gas is that the high-density, high-pressure state is non-magnetic. In the case of a $3d$-band metal, the volume dependence of the density of states is $N(E_f) \sim V^{5/3}$ whereas the volume dependence of the exchange interaction parameter is $\mathscr{E} \sim V^{-5/3(1-\alpha)}$ with $(0.5 < \alpha < 1)$.[36] This suggests that as pressure is increased, $N(E_f)$ decreases at a faster rate than the rate of increase for $\mathscr{E}$ which reduces the likelihood of a ferromagnetic ground state in a $3d$ transition metal element or compound.

In general, the pressure coefficient of the Curie temperature $\mathrm{d}T_C/\mathrm{d}T_P$, may be initially negative or positive for an itinerant ferromagnet according to the Wohlfarth model [37]: $\mathrm{d}T_C/\mathrm{d}T_P = \mathrm{A}T_C - \mathrm{B}/T_C$ (with A and B positive constants). Most $3d$ systems exhibit negative pressure coefiicients ($\mathrm{d}T_C/\mathrm{d}T_P < 0$) owing to the fact that most $3d$ itinerant electron ferromagnets of interest have low values of magnetic ordering temperature T_C. In the case of strong itinerant ferromagnetism, one of the $3d$ spin sub-bands is completely full as shown in Fig. 2.5 (b). As such, the magnetic moment is saturated and there is usually hardly an change in the magnetization as pressure is increased.[38] In contrast, weak itinerant ferromagnets (as shown in Fig. 2.5 (c)) exhibit extremely small magnetic moments per formula unit and low values of the magnetic ordering temperature T_C. Hence the magnetism is usually destroyed quickly with the application of small external pressure. As an example, in the weak itinerant ferromagnet $\mathrm{ZrZn_2}$, the Curie temperature is reduced quickly from $T_C = 25$ K at ambient pressure to $T_C = 0$ K at $P = 0.8$ GPa.[39–41] There are cases in which the magnetic properties are significantly enhanced under the initial application of external pressure. The weak itinerant-electron ferromagnet Sc_3In shows a positive pressure dependence in its low and high temperature magnetic moments as well as a positive pressure coefficient ($dT_C/dT_P > 0$) for the magnetic ordering temperature.[42, 43] Such a pressure-induced enhancement of the magnetic properties of Sc_3In is not well accounted for by the Stoner-Wohlfarth model in which the density of states at the Fermi energy is assumed to scale with the bandwidth W.[37] As an alternative to the Stoner-Wohlfarth model, for a system with a weak exchange interaction $\mathscr{E}$, the application of pressure could lead to an enhancement of the magnetic properties if there was a pressure-induced change in the number of d electrons, which would cause the Fermi energy to shift into a peak in the density of states $N(E)$. In Chapter 7, the results of the effect of pressure on the recently discovered weak itinerant antiferromagnetic metal TiAu are presented, which indicate that there is an initial enhancement of the Néel temperature T_N as pressure is increased up to $\sim$ 6 GPa. At present, a theory explaining the magnetovolume effects for weak itinerant antiferromagnets does not exist. However, pressure experiments on the weak itinerant antiferromagnets Cr and $Cr_{1-x}V_x$, suggest that the suppression of magnetic order with pressure results from an increase in band (kinetic) energy at the expense of exchange energy.[44]

2.4 Superconductivity

The first report of the effect of pressure on superconductivity revealed that (for the simple metals of Sn and In) the superconducting transition temperature T_c decreases with pressure.[45] This initial observation is consistent with the pressure dependence of the vast majority of superconductors which exhibit a negative pressure coefficient ($dT_c/dP < 0$) where T_c decreases monotonically with pressure P.[46, 47] In contrast to the tendency of pressure to suppress the superconductivity in simple conventional superconductors, T_c

is observed to increase with pressure in the high-temperature superconducting cuprate oxides.[48–50] Despite these observed differences in dT_c/dP, the current understanding of the pairing mechanisms responsible for superconductivity in the different classes of superconducting materials is consistent with the response of T_c to pressure. In conventional superconducting materials, the pressure-induced stiffening of the lattice tends to inhibit the pairing of electrons. In the layered structures of the high-T_c cuprates, theoretical models which attribute the pairing of electrons to *intra*-planar mechanisms rather than *inter*-planar mechanisms are consistent with uni-axial pressure investigations in which T_c is observed to increase with decreasing planar area rather than decreasing separation between the planes. However, a complete understanding of the nature of high-temperature superconductivity is still lacking. One of the main research objectives in condensed matter physics today is to develop a comprehensive theory of superconductivity in the high-T_c cuprates. Pressure experiments offer a clean and systematic avenue for investigating the effect of a change in lattice parameter on T_c and other superconducting properties with the primary objective of increasing our understanding of the pairing mechanism in high-T_c layered superconducting materials such as the cuprate oxides. The subject of the effect of pressure on layered superconducting materials is of particular relevance to some of the investigations examined in this dissertation. In Chapters 4 and 5, the effect of pressure on both the normal-state transport and superconducting properties of the layered BiS_2 superconducting materials will be discussed. Some of these layered superconducting materials undergo a pressure-induced structural phase transition at ambient temperature which is accompanied by a rapid enhancement of superconductivity from a low-T_c to high-T_c phase in which there is as much as a threefold enhancement of T_c.

2.4.1 BCS Theory of Superconductivity

The BCS (Bardeen-Cooper-Schrieffer) theory of superconductivity is sometimes regarded as a one parameter theory.[51] Specifically, there is a single parameter associated with the superconducting state, namely, the superconducting transition temperature T_c, that factors into the more salient phenomena associated with the superconductivity. Some of the more important phenomena include the perfect diamagnetism associated with the Meissner-Ochsenfeld effect, the long-range order quantitatively characterized by the coherence length, the existence of an energy gap for single particle excitations between the superconducting ground state and the normal state, and the vanishing of electrical resistance below the superconducting transition.[52]

As the temperature of a metal in the normal state is lowered through T_c, the material undergoes a second order phase transition to the superconducting state in which the conduction electrons form "Cooper" pairs that consist of two electrons with opposite spins and momenta. The pairing mechanism proposed by the BCS theory of superconductivity, which is now accepted as part of an accurate model for describing conventional superconductivity, is the electron-phonon interaction.[52] The Coulomb repulsion between the two conduction electrons is screened by the motion of the positive ions of the lattice (or phonons); the screening allows for the attraction or "pairing" of electrons, provided that the difference in kinetic energy of the two conduction electrons is not larger than the typical energy of a phonon, namely $\hbar\omega_D$, where ω_D is the Debye frequency. This proposed phonon-mediated coupling of electrons is confirmed by experiments on different isotopes of simple s- and p-electron metals such as Pb, Sn, Hg, etc. in which the superconducting transition temperature T_c is suppressed with increasing atomic mass M of the isotope according to a $1/M^{\alpha}$ dependence with $\alpha = 1/2$.[53–56]

In the superconducting phase, the ground states that are available to the electrons are grouped in pairs such that either both states of a pair are occupied or both states of a pair are unoccupied. The two electrons that make up a pair have opposite spins and have a combined momentum that is equal to the momentum of any other superconducting pair. In the case of a superconductor with zero current, the sum of the total momentum of the pair is zero, *i.e.*, the electrons that make up a pair have equal and opposite momentum.

A conduction electron that is paired in the superconducting state can become temporarily unpaired as it scatters off a phonon. Scattering from energetic phonons arising from thermal fluctuations may excite an electron to an energy level above the energy gap. An excited electron can occupy any of the available states at higher energy and thus fail to return to its paired state (or ground state) before the scattering event. However, if the scattering interaction is not too strong, the unpaired conduction electron will soon return to its paired state with exactly the same momentum prior to scattering such that there is no net change in the momentum of the charge carriers of the system and hence no lasting net effect on the current (or electrical resistivity) of the system. Hence, the momentum pairing of conduction electrons in the superconducting state accounts for both the vanishing dc electrical resistance and the long-range superconducting order which is quantitatively characterized by a coherence length given by $\xi_0 \sim \frac{\hbar v_f}{k_B T_c}$, where v_f is the Fermi velocity; ξ_0 is of the order of a micrometer for simple *s*- and *p*-wave superconductors, but may be much smaller for exotic superconductors including low-T_c heavy-fermion and high-T_c cuprate-oxide superconductors.

2.4.2 The suppression of superconductivity with pressure in simple *s*- and *p*-electron metals

The tendency of pressure to reduce T_c in conventional superconductors is primarily due to a pressure-induced enhancement of the spring constant k that governs the phonon vibrational frequency $\omega \approx \sqrt{k/M}$. In short, a "stiffening" of the lattice interrupts the phonon-mediated pairing of superconducting electrons. This is reminiscent of the isotope effect described above where the substitution of atoms of varying mass M has a singular effect on the spectrum of phonon vibration frequencies. Both the pressure and isotope effects are easily accounted for in the following simple expression for the transition temperature T_c in a conventional superconductor [52] in which the coupling of the conduction electrons to the lattice is not too strong:

$$k_B T_c = 1.13\hbar\omega_D \exp\left\{\frac{-1}{N(E_f)\mathscr{V}_{eff}}\right\}. \tag{2.17}$$

In Equation 2.17, ω_D is the Debye frequency, $N(E_f)$ is the density of electronic states at the Fermi energy, and $\mathscr{V}_{eff}$ is the effective interaction between conduction electrons and the lattice that is responsible for the pairing of electrons into Cooper pairs. In the negative exponent, a reduction in either $N(E_f)$ or $\mathscr{V}_{eff}$ has the effect of lowering T_c. In Section 2.3.2, we learned that for a low-density free-electron gas, the volume dependence of the density of states is $N(E_f) \sim V^{2/3}$. The effect of pressure is to reduce $N(E_f)$; however, the dominant effect due to an increase in pressure is the reduction in the effective pairing interaction $\mathscr{V}_{eff}$. In the limit of a strong coupling interaction between electrons and phonons (and a weak electron-electron (Coulomb) repulsion), the expression for the electron-phonon coupling interaction was worked out by W. L. McMillan [57] as a ratio of the average over the Fermi surface of the square of the electronic matrix element $\langle \mathrm{X}^2 \rangle$ to the average of the square of the phonon frequency $\langle \omega^2 \rangle$ scaled by the atomic mass M^{-1}:

$$\lambda = N(E_f)\mathscr{V}_{eff} = \frac{N(E_f)\langle \mathrm{X}^2 \rangle}{M\langle \omega^2 \rangle}. \tag{2.18}$$

Here, λ is the electron-phonon coupling parameter and for $\langle \omega^2 \rangle \approx \langle \omega \rangle^2 \approx k/M$, where k is the lattice spring constant not to be confused with Boltzmann's constant k_B in Equation 2.17, it is possible to rewrite the expression for the superconducting transition temperature T_c explicitly as a function of the atomic mass M, the lattice spring constant k, and the density of states $N(E_f)$:

$$T_c \approx \sqrt{\frac{k}{M}} \exp\left\{\frac{-k}{N(E_f)\langle \mathrm{X}^2 \rangle}\right\}. \tag{2.19}$$

Here, the pressure-induced stiffening of the lattice which is reflected in a larger value of k is dominant to the weak dependence on pressure of the denominator: $N(E_f)\langle \mathrm{X}^2 \rangle$. Furthermore, an enhancement of k which appears in the negative exponent is dominant to the effect of k in the prefactor $\sqrt{k/M}$. The universal decrease in the superconducting transition temperature T_c with pressure in simple metals is ultimately a result of the pressure-induced stiffening of the lattice and the associated shift of the phonon vibrational spectrum to higher frequency $\omega = \sqrt{k/M}$. As a final note, the weakening of the electron-phonon interaction $\lambda \propto 1/k$ due to a stiffening of the lattice under pressure is responsible for the almost universal decrease in the normal-state electrical resistivity ρ for simple metals. Alternatively, this can be explained by the pressure-induced enhancement of the Debye temperature $\Theta_D = \hbar\omega_D = \hbar\sqrt{k/M}$ which translates into an increase in electron mobility μ and a reduction of the electrical resistivity $\rho \propto 1/\mu$ (see Section 2.2).

2.4.3 Anomalous dT_c/dP behavior: pressure-induced structural and electronic transitions in superconductors

As discussed previously, pressure has a tendency to destroy superconductivity by weakening the phonon-electron coupling parameter λ. It stands to reason that a material that is not superconducting at ambient pressure would be unlikely to exhibit superconductivity at high pressure. However, there are numerous elements and materials that are only superconducting under the application of pressure. The application of pressure has raised the total number of superconducting elements from 29 (at ambient pressure) to 52.[58] Many of the non-superconducting alkali metals exhibit pressure-induced superconductivity. For example, Li undergoes a structural phase transition and an associated superconducting transition at $T_c \sim 5$ K and $P \sim 20$ GPa which is followed by a rapid and nearly threefold enhancement of T_c to 14 K at a pressure of $P = 30$ GPa.[59–61] As another example, the alkali metal Cs undergoes a pressure-induced electronic transition at $P \sim 15$ GPa in which the 6s-band is squeezed toward the top of the empty 5d band near the Fermi energy allowing for an $s \to d$ charge transfer.[62–64] Hence, at pressures above 15 GPa, the alkali metal Cs obtains the characteristics typical of non-magnetic transition metals with a large density of states (d-band conduction electrons) at the Fermi energy which is favorable for the occurrence of superconductivity. The anomalous and sometimes complex $T_c(P)$ behavior observed in some of the transition metal superconductors is often the result of pressure-induced structural and electronic transitions whereby the $s \to d$ charge transfer results in an enhanced number of d-band conduction electrons.

The pressure investigations of the layered superconductors $Ln\mathrm{O}_{0.5}\mathrm{F}_{0.5}\mathrm{BiS}_2$ (Ln = La, Ce, Pr, Nd) discussed in Chapters 4 and 5 of this dissertation reveal some rather anomalous behavior in the pressure dependence of T_c in which there is pressure-induced enhancement of T_c from a low-T_c superconducting phase to a high-T_c superconducting phase. In the particular case of the $\mathrm{LaO}_{0.5}\mathrm{F}_{0.5}\mathrm{BiS}_2$ compound, associated with the rapid three-fold enhancement of T_c from ~ 3 to 10 K is a high temperature structural transition from the tetragonal to monoclinic phase at a transition pressure of $P_T \sim 1$ GPa as shown in Fig. 2.6. Although it is unclear as to the nature of the pairing mechanism in these layered materials, the superconductivity is known to occur in the BiS_2 layers. Single crystal studies under uniaxial and hydrostatic pressure are needed in order to investigate the lattice effects on superconductivity.

Investigation of the effects of pressure on superconductivity in various binary compounds with high values of T_c such as the quasi-two-dimensional material MgB_2, or the alkali-doped fullerides $A_3\mathrm{C}_60$ with A = K, Rb, and Cs, reveal that the pairing mechanism of electrons responsible for superconductivity is *intraplanar* (in the case of MgB_2) and *intramolecular* (in the case of A_3C_60). In both classes of binary materials, which are shown to behave as conventional superconductors with electron-phonon coupling, the superconducting transition temperature T_c exhibits a negative pressure dependence, but for different reasons. As with the case of most simple *s*- and *p*-electron conventional superconductors, the reduction of T_c with pressure in MgB_2 is due to the lattice stiffening in the B_2 planes, where the phonon mediated pairing of electrons is believed to occur.[65, 66] For the extremely stiff C_{60} molecule in the doped fullerene Rb_3C_{60}, both the frequency of phonon vibration $\langle\omega\rangle$ and the mean-square of the electron-phonon matrix element $\langle X^2\rangle$, are independent of pressure (see McMillan expression for the coupling parameter λ in Equation 2.18). The reduction in T_c with pressure results from a rapid decrease in the electronic density of states $N(E_f)$ with an increase in pressure due to the broadening of the conduction band as the C_{60} molecules are squeezed together.[67] Relatedly, an enhancement of T_c observed in A_3C_60 with A = K, Rb, and Cs with T_c = 19, 29.5, and 40 K, respectively, is primarily accounted for by the increase in $N(E_f)$ as the conduction band is narrowed in an expanded lattice of larger alkali ions.

2.4.4 Pressure-induced enhancement of T_c in the layered cuprate superconductors

Barring any pressure-induced structural phase transitions or electronic transitions such as in the case of $s \rightarrow d$ charge transfer, most simple-metal and binary-material compounds behave as conventional superconductors with a phonon-mediated pairing mechanism for electrons in which the effect of pressure is to increase the stiffness of the lattice, thereby interrupting the pairing of electrons and reducing the superconducting transition temperature T_c. In the high-T_c cuprate oxides, the superconducting pairing mechanism is believed to be unconventional (for which most researchers believe is to be enhanced by

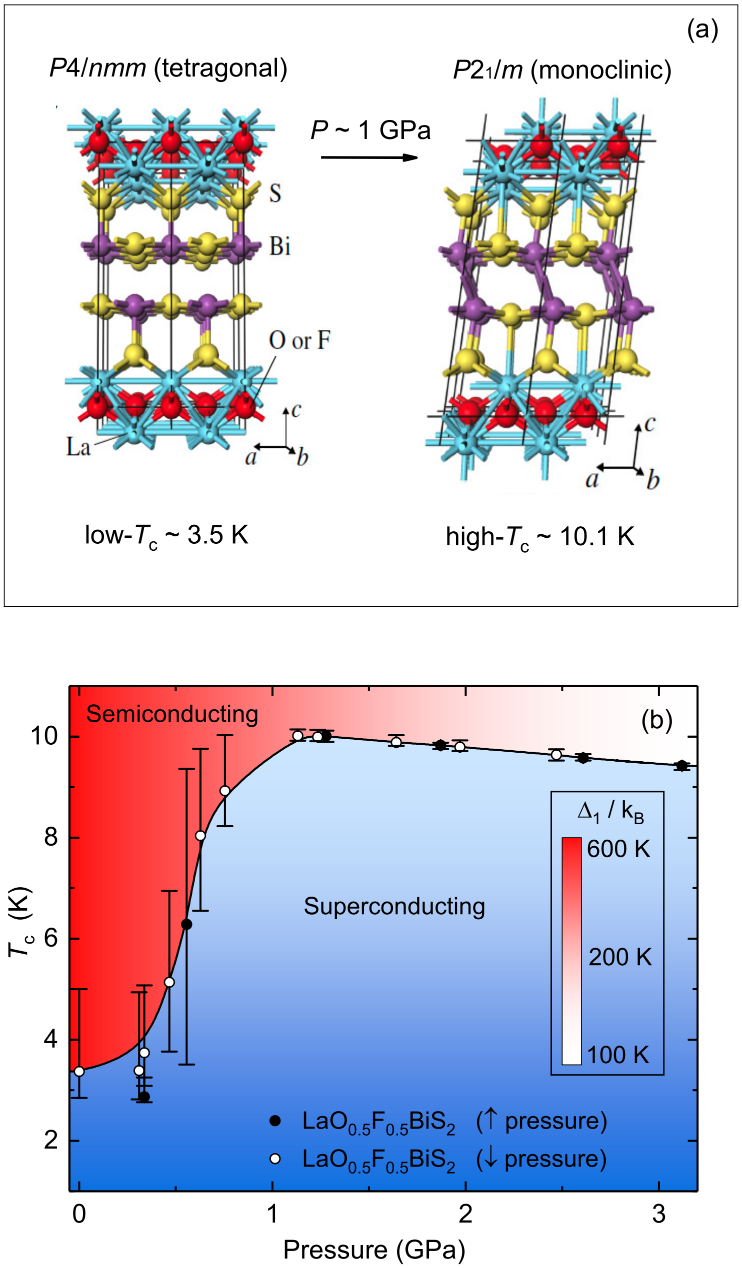

Figure 2.6: (a) A schematice of a pressure-induced structural phase transition from the tetragonal to monoclinic structure in the layered superconductor $LaO_{0.5}F_{0.5}BiS_2$ occurring at a transition pressure of $P_t \sim 1$ GPa. (b) The superconducting critical transition temperature T_c vs pressure P, illustrating the rapid enhancement of T_c at the same transition pressure $P_t \sim 1$ GPa that forces the structural transition in panel (a). Panel (a) adapted from Ref. [68] and panel (b) adapted from Ref. [69].

spin-fluctuations), and the initial effect of applied pressure is to increase T_c. For example, T_c increases with pressure P at an exceptionally high rate (dT_c/d$P > 6$ K GPa^{-1}) for the $La_{1.8}Ba_{0.2}CuO_{4-\delta}$ compound.[70] This large pressure coefficient motivated a series of chemical substitution experiments designed to simulate the effect of external pressure with a "chemical pressure" (or lattice contraction) in which the La^{3+} ions were replaced with smaller Y^{3+} ions.[71] The new Y-Ba-Cu-O system exhibited a high superconducting transition temperature with T_c = 93 K. However, upon the application of pressure, there was no additional enhancement of T_c but rather a broadening of the superconducting transition. Further experiments revealed that the superconducting phase in Y-B-Cu-O was characterized as the tetragonal $RE_{1.8}Ba_{0.2}Cu_3O_{6+\delta}$ phase with $T_c \geq 90$ K for various rare earth (*RE*) ions of different sizes *RE* = La, Nd, Sm, Eu, Gd, Ho, Er, and Lu. The results indicated that the layered structure with planes of CuO_2-Ba-$CuO_{2-\delta}$-Ba-CuO_2 separated by *RE* ions along the *c*-axis is responsible for the substantial increase of T_c rather than the effect of a lattice contraction due to smaller *RE* ion size.[72]

The essential structural feature of the high-T_c cuprate materials is the CuO_2 planar lattice where the carrier (electron or hole) concentration n per Cu cation has an important effect on the behavior of T_c. Although $T_c(n)$ exhibits dome-like behavior for both hole-doped and electron-doped high-T_c cuprates, only the hole-doped materials show an increase in T_c with increasing n according to the following expression [73, 74]:

$$T_c(n) = T_c^{max}[1 - \beta(n - n_{opt})^2], \tag{2.20}$$

where $\beta \simeq 82.6$ and $n_{opt} \simeq 0.16$. It is clear from experiment that an initial increase in pressure has the effect of increasing the concentration of holes n in the CuO_2 planes such that the $T_c(n)$ dependence adds an additional degree of freedom in determining the pressure effect on T_c in the high-T_c cuprates.[58] This makes it more difficult to determine the intrinsic effect of pressure on T_c in these materials. The pressure dependence of T_c can then be separated into (1) the pressure-induced change in n and its effect on T_c as expressed in Equation 2.20 and (2) the "intrinsic" pressure-induced effects on the lattice parameters in the layered structures of the cuprates.[75] Indeed, as observed in the anomalous $T_c(P)$ behavior in the transition-metal superconductors described above, the pressure-induced changes to both the lattice parameters and also the effect of pressure on the electronic properties are necessary for a complete understanding of the response of the high-T_c cuprate superconducting materials to pressure. Short of a full discussion of the other factors that may influence the pressure-dependence of T_c in the layered cuprate-oxide superconducting materials, including pressure-induced structural transitions, pressure-induced increases in n due to ordering of oxygen, and the effect of non-hydrostatic strain, the following discussion will be limited to the intrinsic effect of pressure on T_c for near optimally doped high-T_c cuprate compounds. For $n \simeq n_{opt}$ (near T_c^{max}), the n dependence ($dT_c/\mathrm{d}n \simeq 0$) is negligible, and therefore the effect of pressure on T_c due to dn/dP is small. It is in this region that one can better isolate the intrinsic pressure-induced lattice effects on T_c. The pressure-induced enhancement of T_c owing to a reduction in volume V for numerous high-T_c cuprate systems over an extended pressure range up to $P \sim 30$ GPa is astonishingly consistent: $T_c \propto V^{-1.2}$.[75] The weak volume dependence of T_c is well accounted for by the large number of uniaxial pressure experiments which determined that while the intrinsic effect of pressure on T_c is large within the planes, the pressure-induced changes to the spacing between CuO planes has relatively little effect on T_c. At optimal doping, it is found that the intrinsic pressure-induced enhancement of T_c varies as the inverse of the square of the area A of the CuO_2 planes: $T_c \propto A^{-2}$.

The clever investigations involving pressure for optimally doped high-T_c cuprate materials serve as both motivation and an experimental-design model for the pressure experiments performed on the layered superconducting compounds LnO$_{1-x}$F$_x$BiS$_2$ discussed in Chapters 4 and 5. The dome-like behavior observed in the dependence of T_c on fluorine concentration x (electron doping) is reminiscent of the $T_c(n)$ dependence in the high-T_c cuprate materials. For several of the $Ln\mathrm{O}_{1-x}\mathrm{F}_x\mathrm{BiS}_2$ ($Ln = $ La, Ce, Pr, Nd) compounds, the optimal doping level is shown to be $x_{opt} \simeq 0.5$.

Blbliography

[1] H. G. Drickamer and C. W. Frank, *Electronic Transitions and the High Pressure Chemistry and Physics of Solids*, Studies in Chemical Physics (Springer Netherlands, Netherlands, 1973).

[2] P. P. Edwards and M. J. Sienko, "The transition to the metallic state", Acc. Chem. Res. **15**, 87–93 (1982).

[3] P. W. Bridgman, "Change of Phase under Pressure. I. The Phase Diagram of Eleven Substances with Especial Reference to The Melting Curve", Phys. Rev. **3**, 153–203 (1914).

[4] P. P. Edwards, M. T. J. Lodge, F. Hensel, and R. Redmer, "'. . . a metal conducts and a non-metal doesn't'", Philos. Trans. R. Soc. London, Ser. A **368**, 941–965 (2010).

[5] H. Drickamer, "The Effect of High Pressure on the Electronic Structure of Solids", Solid State Physics **17**, 1–133 (1965).

[6] Dubrovinsky, L. and Dubrovinskaia, N. and Bykova, E. and Bykov, M. and Prakapenka, V. and Prescher, C. and Glazyrin, K. and Liermann, H. -P. and Hanfland, M. and Ekholm, M. and Feng, Q. and Pourovskii, L. V. and Katsnelson, M. I. and Wills, J. M. and Abrikosov, I. A., "The most incompressible metal osmium at static pressures above 750 gigapascals", Nature **525**, 226–229 (2015).

[7] J. S. Schilling, "Pressure as a parameter in the study of dilute magnetic alloys", Adv. Phys. **28**, 657–715 (1979).

[8] J. S. Schilling, "Some Recent Results in Magnetism under High Pressure", in *Physics of Solids under High Pressure*, edited by J. S. Schilling and R. S. Shelton (North-Holland Publishing Company, Amsterdam, 1981), pp. 345–356.

[9] J. Friedel, "XIV. The distribution of electrons around impurities in monovalent metals", Phil. Mag. **43**, 153–189 (1952).

[10] P. W. Anderson, "Localized Magnetic States in Metals", Phys. Rev. **124**, 41–53 (1961).

[11] M. B. Maple, "Superconductivity: A probe of the magnetic state of local moments in metals", Appl. Phys. **9**, 179–204 (1976).

[12] L. L. Hirst, "Theory of magnetic impurities in metals", Phys. Kondens. Mat. **11**, 255–278 (1970).

[13] M. B. Maple and D. Wohlleben, "Nonmagnetic $4f$ Shell in the High-Pressure Phase of SmS", Phys. Rev. Lett. **27**, 511–515 (1971).

[14]M. B. Maple and D. Wohlleben, "Demagnetization of Rare Earth Ions in Metals Due to Valence Fluctuations", AIP Conf. Proc. **18**, 447–462 (1974).

[15]M. B. Maple, J. G. Huber, and K. S. Kim, "Pressure dependence of the pair breaking parameter of superconductors with Ce impurities", Solid State Comm. **8**, 981–985 (1970).

[16]J. G. Huber and M. B. Maple, "The effect of nonmagnetic $4f$ resonances on the superconducting transition temperature: ThCe alloys", J. Low Temp. Phys. **3**, 537–544 (1970).

[17]N. W. Ashcroft and N. D. Mermin, *Solid State Physics* (Brooks/Cole, Australia and United States, 1976).

[18]M. B. Maple, E. D. Bauer, V. S. Zapf, and J. Wosnitza, "Unconventional Superconductivity in Novel Materials", English, in *Superconductivity*, edited by K. H. Bennemann and J. B. Ketterson (Springer, Berlin Heidelberg, 2008), pp. 639–762.

[19]J. Jensen and A. R. Mackintosh, *Rare Earth Magnetism: Structures and Excitations*, The International Series of Monographs on Physics (Clarendon Press, Oxford, 1991).

[20]J. R. Schrieffer and P. A. Wolff, "Relation between the Anderson and Kondo Hamiltonians", Phys. Rev. **149**, 491–492 (1966).

[21]J. Kondo, "g-Shift and Anomalous Hall Effect in Gadolinium Metals", Prog. Theor. Phys. **28**, 846–856 (1962).

[22]P. G. De Gennes, "Polarisation de charge (ou de spin) au voisinage d'une impureté dans un alliage", J. Phys. Radium **23**, 630–636 (1962).

[23]J. Kondo, "Resistance Minimum in Dilute Magnetic Alloys", Prog. Theor. Phys. **32**, 37–49 (1964).

[24]M. A. Ruderman and C. Kittel, "Indirect Exchange Coupling of Nuclear Magnetic Moments by Conduction Electrons", Phys. Rev. **96**, 99–102 (1954).

[25]T. Kasuya, "A Theory of Metallic Ferro- and Antiferromagnetism on Zener's Model", Prog. Theor. Phys. **16**, 45–57 (1956).

[26]K. Yosida, "Magnetic Properties of Cu-Mn Alloys", Phys. Rev. **106**, 893–898 (1957).

[27]S. Doniach, "The Kondo lattice and weak antiferromagnetism", Physica B **91**, 231–234 (1977).

[28] K. H. J. Buschow, “Intermetallic compounds of rare-earth and 3*d* transition metals”, Rep. Prog. Phys **40**, 1179 (1977).

[29] F. Bloch, “Bemerkung zur Elektronentheorie des Ferromagnetismus und der elektrischen Leitfähigkeit”, Zeitschrift für Physik **57**, 545–555 (1929).

[30] E. C. Stoner, “Collective Electron Ferromagnetism”, Proc. Roy. Soc. A **165**, 372–414 (1938).

[31] E. C. Stoner, “Collective Electron Ferromagnetism. II. Energy and Specific Heat”, Proc. Roy. Soc. A **169**, 339–371 (1939).

[32] E. C. Stoner, “Collective Electron Specific Heat and Spin Paramagnetism in Metals”, Proc. Roy. Soc. A **154**, 656–678 (1936).

[33] E. P. Wohlfarth, “The theoretical and experimental status of the collective electron theory of ferromagnetism”, Rev. Mod. Phys. **25**, 211–219 (1953).

[34] J. Friedel, “Transition Metals. Electronic Structure of the *d*-Band. Its Role in the Crystalline and Magnetic Structures”, in *The Physics of Metals*, edited by J. Ziman (Cambridge University Press, Cambridge, 1969), p. 340.

[35] E. C. Stoner F.R.S., “Ferromagnetism”, Rep. Prog. Phys **11**, 43 (1947).

[36] T. F. M. Kortekaas and J. J. M. Franse, “Volume magnetostriction in Ni_3Al and Ni-Pt alloys and its interpretation in the band model of magnetism”, J. Phys. F Met. Phys. **6**, 1161 (1976).

[37] E. Wohlfarth, “The invar problem”, IEEE Trans. Magn. **11**, 1638–1644 (1975).

[38] K. Buschow, M. Brouha, J. Biesterbos, and A. Dirks, “Crystalline and amorphous rare-earth transition metal alloys”, Physica B **91**, 261–270 (1977).

[39] R. C. Wayne and L. R. Edwards, “Effect of Pressure on the Curie Temperature of $ZrZn_2$”, Phys. Rev. **188**, 1042–1044 (1969).

[40] T. F. Smith, J. A. Mydosh, and E. P. Wohlfarth, “Destruction of Ferromagnetism in $ZrZn_2$ at High Pressure”, Phys. Rev. Lett. **27**, 1732–1735 (1971).

[41] J. G. Huber, M. B. Maple, D. Wohlleben, and G. S. Knapp, “Magnetic properties of $ZrZn_2$ under pressure”, Solid State Commun. **16**, 211–216 (1975).

[42] W. E. Gardner, T. F. Smith, B. W. Howlett, C. W. Chu, and A. Sweedler, “Magnetization Measurements and Pressure Dependence of the Curie Point of the Phase Sc_3In”, Phys. Rev. **166**, 577–588 (1968).

[43] J. Grewe, J. S. Schilling, K. Ikeda, and K. A. Gschneidner, "Anomalous behavior of the weak itinerant ferromagnet Sc_3In under hydrostatic pressure", Phys. Rev. B **40**, 9017–9024 (1989).

[44] Jaramillo, R. and Feng, Yejun and Lang, J. C. and Islam, Z. and Srajer, G. and Rønnow, H. M. and Littlewood, P. B. and Rosenbaum, T. F., "Chromium at high pressures: Weak coupling and strong fluctuations in an itinerant antiferromagnet", Phys. Rev. B **77**, 184418 (2008).

[45] G. J. Sizoo and H. K. Onnes, "Further experiments with liquid helium. Influence of elastic deformation on the supraconductivity of tin and indium", Commun. Phys. Lab. Univ. Leiden **180** (1925).

[46] M. Levy and J. Olsen, "Can pressure destroy superconductivity in aluminum", Solid State Commun. **2**, 137–139 (1964).

[47] T. F. Smith and C. W. Chu, "Will Pressure Destroy Superconductivity?", Phys. Rev. **159**, 353–358 (1967).

[48] A.-K. Klehe, A. Gangopadhyay, J. Diederichs, and J. Schilling, "Dependence of the superconducting transition temperature of $HgBa_2CaCu_2O_{4+\delta}$ on hydrostatic pressure", Physica C **213**, 266–270 (1993).

[49] A.-K. Klehe, J. Schilling, J. Wagner, and D. Hinks, "Hydrostatic presure dependence of the superconducting transition temperature of $HgBa_2CaCu_2O_{6+\delta}$ and $HgBa_2Ca_2Cu_3O_{8+\delta}$", Physica C **223**, 313–320 (1994).

[50] L. Gao, Y. Y. Xue, F. Chen, Q. Xiong, R. L. Meng, D. Ramirez, C. W. Chu, J. H. Eggert, and H. K. Mao, "Superconductivity up to 164 K in $HgBa_2Ca_{m-1}Cu_mO_{2m+2+\delta}$ $(m = 1, 2, \text{and } 3)$ under quasihydrostatic pressures", Phys. Rev. B **50**, 4260–4263 (1994).

[51] D. M. Ginsberg, "Experimental Foundations of the BCS Theory of Superconductivity", Am. J. Phys. **30**, 433–438 (1962).

[52] J. Bardeen, L. N. Cooper, and J. R. Schrieffer, "Theory of Superconductivity", Phys. Rev. **108**, 1175–1204 (1957).

[53] E. Maxwell, "Isotope Effect in the Superconductivity of Mercury", Phys. Rev. **78**, 477–477 (1950).

[54] C. A. Reynolds, B. Serin, W. H. Wright, and L. B. Nesbitt, "Superconductivity of Isotopes of Mercury", Phys. Rev. **78**, 487–487 (1950).

[55] B. Serin, “Chapter VII The Magnetic Threshold Curve of Superconductors”, in *Prog. Low Temp. Phys.* Vol. 1, edited by C. Gorter, Prog. Low Temp. Phys. (Elsevier, 1955), pp. 138–150.

[56] R. R. Hake, D. E. Mapother, and D. L. Decker, “Isotope Effect on the Superconducting Transition in Lead”, Phys. Rev. **112**, 1522–1532 (1958).

[57] W. L. McMillan, “Transition Temperature of Strong-Coupled Superconductors”, Phys. Rev. **167**, 331–344 (1968).

[58] B. Lorenz and C. W. Chu, “High Pressure Effects on Superconductivity”, in *Frontiers in Superconducting Materials*, edited by A. V. Narlikar (Springer-Verlag, Berlin, 2005), pp. 459–496.

[59] T. H. Lin and K. J. Dunn, “High-pressure and low-temperature study of electrical resistance of lithium”, Phys. Rev. B **33**, 807–811 (1986).

[60] K. Shimizu, H. Ishikawa, D. Takao, T. Yagi, and K. Amaya, “Superconductivity in compressed lithium at 20 K”, Nature **419**, 597–599 (2002).

[61] V. V. Struzhkin, M. I. Eremets, W. Gan, H.-k. Mao, and R. J. Hemley, “Superconductivity in dense lithium”, Science (2002).

[62] Wittig, Jörg, “Pressure-induced superconductivity in cesium and yttrium”, Phys. Rev. Lett. **24**, 812–815 (1970).

[63] J. Wittig, “Presure induced d- and possible f-band superconductors”, in *Superconductivity in d- and f-Band Metals*, edited by W. Buckel and W. Weber (Kernforschungszentrum Karlsruhe, Karlsruhe, 1982), pp. 321–329.

[64] M. Ross and A. K. McMahan, “Systematics of the $s \rightarrow d$ and $p \rightarrow d$ electronic transition at high pressure for the elements I through La”, Phys. Rev. B **26**, 4088–4093 (1982).

[65] S. L. Bud’ko, G. Lapertot, C. Petrovic, C. E. Cunningham, N. Anderson, and P. C. Canfield, “Boron Isotope Effect in Superconducting MgB_2”, Phys. Rev. Lett. **86**, 1877–1880 (2001).

[66] D. G. Hinks, H. Claus, and J. D. Jorgensen, “The complex nature of superconductivity in MgB_2 as revealed by the reduced total isotope effect”, Nature **411**, 457–460 (2001).

[67] J. Diederichs, A. K. Gangopadhyay, and J. S. Schilling, “Pressure dependence of the electronic density of states and T_c in superconducting Rb_3C_{60}”, Phys. Rev. B **54**, R9662–R9665 (1996).

[68] T. Tomita, M. Ebata, H. Soeda, H. Takahashi, H. Fujihisa, Y. Gotoh, Y. Mizuguchi, H. Izawa, O. Miura, S. Demura, K. Deguchi, and Y. Takano, "Pressure-Induced Enhancement of Superconductivity and Structural Transition in BiS_2-Layered $LaO_{1-x}F_xBiS_2$", J. Phys. Soc. Japan **83**, 063704 (2014).

[69] C. T. Wolowiec, D. Yazici, B. D. White, K. Huang, and M. B. Maple, "Pressure-induced enhancement of superconductivity and suppression of semiconducting behavior in $LnO_{0.5}F_{0.5}BiS_22$ (Ln = La, Ce) compounds", Phys. Rev. B **88**, 064503 (2013).

[70] C. W. Chu, P. H. Hor, R. L. Meng, L. Gao, Z. J. Huang, Wang, and Y. Q., "Evidence for superconductivity above 40 K in the La-Ba-Cu-O compound system", Phys. Rev. Lett. **58**, 405–407 (1987).

[71] M. K. Wu, J. R. Ashburn, C. J. Torng, P. H. Hor, R. L. Meng, L. Gao, Z. J. Huang, Y. Q. Wang, and C. W. Chu, "Superconductivity at 93 K in a new mixed-phase Y-Ba-Cu-O compound system at ambient pressure", Phys. Rev. Lett. **58**, 908–910 (1987).

[72] P. H. Hor, R. L. Meng, Y. Q. Wang, L. Gao, Z. J. Huang, J. Bechtold, K. Forster, and C. W. Chu, "Superconductivity above 90 K in the square-planar compound system $ABa_2Cu_3O_{6+\mathrm{x}}$ with A=Y, La, Nd, Sm, Eu, Gd, Ho, Er and Lu", Phys. Rev. Lett. **58**, 1891–1894 (1987).

[73] M. Presland, J. Tallon, R. Buckley, R. Liu, and N. Flower, "General trends in oxygen stoichiometry effects on T_c in Bi and Tl superconductors", Physica C **176**, 95–105 (1991).

[74] J. L. Tallon, C. Bernhard, H. Shaked, R. L. Hitterman, and J. D. Jorgensen, "Generic superconducting phase behavior in high-T_c cuprates: T_c variation with hole concentration in $YBa_2Cu_3O_{7-\delta}$", Phys. Rev. B **51**, 12911–12914 (1995).

[75] J. S. Schilling, "High-Pressure Effects", in *Handbook of High-Temperature Superconductivity: Theory and Experiment*, edited by J. R. Schrieffer and J. S. Brooks (Springer New York, New York, NY, 2007), pp. 427–462.

Chapter 3

Experimental Methods

The most common measurement performed on a metal under pressure is that of electrical resistivity, ρ. Considerable information can be obtained about the electronic structure and phase evolution of a material from electrical resistivity measurements under pressure. Even more so, when the measurements of ρ under pressure are used in conjunction with optical experiments under pressure. The results of the pressure experiments discussed in Chapters 4, 5, 6, 7 of this dissertation are based solely on electrical resistivity measurements under pressure. However, some of the discussion and conclusions regarding these results make use of optical experiments under pressure performed by independent researchers.

This chapter provides the details in performing measurements of electrical resistivity under pressure. After an initial discussion regarding the preparation of a sample for a four-wire measurement of electrical resistance, the hydrostatic piston-cylinder cell (PCC) and the diamond anvil cell (DAC) pressure techniques will be discussed. The chapter will conclude with a discussion of manometry for determining the pressure during a measurement.

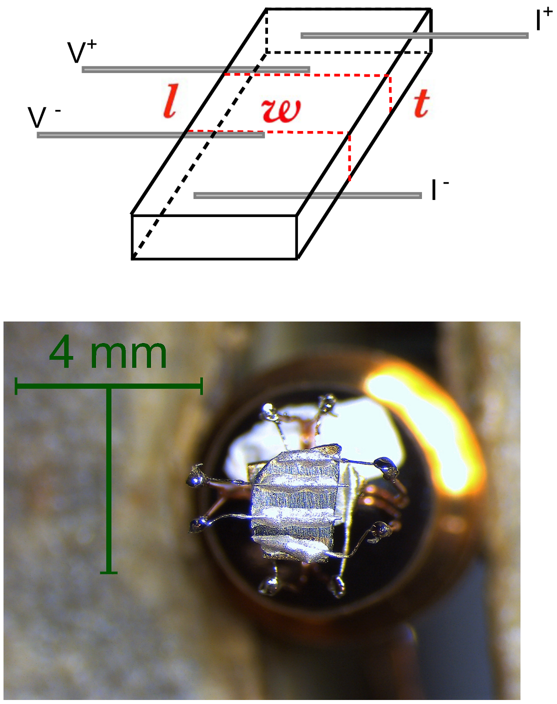

Figure 3.1: (*Top*) A schematic of electrical leads affixed to a sample for a four-wire measurement of electrical resistance. The sample dependent quantity of electrical resistance R is converted to electrical resistivity ρ based on the simple relation: $\rho = (wt/l)R$ where l is the distance across the measured voltage drop, w is the width across the sample (perpendicular to l) and t is the thickness of the sample. (*Bottom*) A photograph of a single crystal sample of an Fe-substituted compound URu_2Si_2 from the pressure investigation discussed in Chapter 6.

3.1 Four-wire measurement of electrical resistance

The standard four-wire technique was used in measuring the electrical resistance of the samples under applied pressure. The typical four-lead configuration includes two pair of platinum leads extending from the sample in an antiparallel fashion. Figure 3.1 includes a schematic (top) of a sample with platinum leads configured for a four-wire measurement and a photograph (bottom) of a single crystal sample of the Fe-substituted URu_2Si_2 which has been prepared for a four-wire electrical resistivity measurement in the hydrostatic piston-cylinder cell. (In the diamond anvil cell (see section 3.2.2 below), electrical contact between the sample and micro-electrodes that are embedded in the diamond anvil occurs during the application of pressure.) Prior to affixing the platinum leads, the sample is first prepared for good electrical contact. The sample is shaped into a rectangle and then polished with 600 grit sandpaper. After masking the polished surface of the sample, gold is evaporated onto the surface of the sample creating four well-separated gold contact pads. The platinum leads (25 to 50 μm in diameter) are then cemented to the sample using a two-part conductive silver epoxy and then later soldered to the 36-guage copper electrical feedthrough wires (see Fig. 3.2(n)). This procedure typically results in a contact resistance of $\approx 2\ \Omega$. In the four-wire measurement, an appropriate value of the current I is supplied by the measurement device while the drop in voltage V is measured across the inside pair of platinum leads by the measurement device. This allows for a determination of the electrical resistance R according to Ohms law: $V = IR$. The four-wire measurements of electrical resistance in each pressure cell were measured with a LR-700 Linear Research ac resistance bridge during which excitation currents were consistently set to 1 mA.

The fact that the current and voltage leads are separate is an important feature of the four-lead measurement technique and is what distinguishes it from the two wire measurement technique in which the same pair of leads is used for both the supply of current and measurement of voltage. A four-wire measurement of electrical resistance allows the experimentalist to eliminate the electrical resistance of the leads (or cables) used in connecting the sample to the measurement device. This is important due to the fact that the electrical resistance of the leads ($\sim 20\ \Omega$) is three or more orders of magnitude larger than the typical electrical resistance of the samples ($\sim$ mΩ) that were measured in these pressure experiments. Furthermore, the signatures of various transitions in the electrical resistivity data have magnitudes on the order of a fraction of a mΩ which would be difficult to study, let alone find, in the large 20 Ω background resistance of the leads. As a final note, the four-wire measurements of electrical resistance R are sample dependent and not intrinsic to the material. A conversion of R to the intrinsic property of electrical resistivity

ρ requires information of the geometry of the four-wire measurement. Once R has been measured it can be converted to ρ based on the following simple relation: $\rho = (wt/l)R$ where l is the distance across the measured voltage drop, w is the width across the sample (perpendicular to l) and t is the thickness of the sample as shown in Fig. 3.1.

3.2 High-pressure techniques

The high-pressure experiments discussed in this dissertation were performed in one of several different pressure cells including the hydrostatic piston cylinder cell, Bridgman anvil cell, and diamond anvil cell. The piston-cylinder cell provides the most hydrostatic environment of the three pressure cells but has an upper limit of $\sim$ 3 GPa. The diamond anvil cell is a direct descendent of the opposed anvil device developed by P. W. Bridgman with the distinction being that the anvils in a DAC are made of highly incompressible single crystal diamond while the opposed anvil cell developed by Bridgman makes use of tungsten carbide anvils. The principle of operation for the DAC and Bridgman anvil cells is the same but the upper limit of pressures reached in the DAC ($\sim$ 100 GPa and above) are considerably higher than the maximal pressure of 16 GPa achieved in a Bridgman anvil cell. A detailed discussion below is only given for the piston-cylinder cell and diamond anvil cell.

3.2.1 Hydrostatic piston-cylinder pressure cell

A schematic of the hydrostatic piston-cylinder cell and pressure clamp used for measurements of electrical resistivity of samples under pressure up to $P \sim 2.5$ GPa is shown in Fig. 3.2. An enlarged view of the sample space (h) located within the Teflon capsule (g) is shown to the right in which two single crystal samples have been wired to the BeCu sample holder (i). The Teflon capsule is filled with a liquid pressure-transmitting

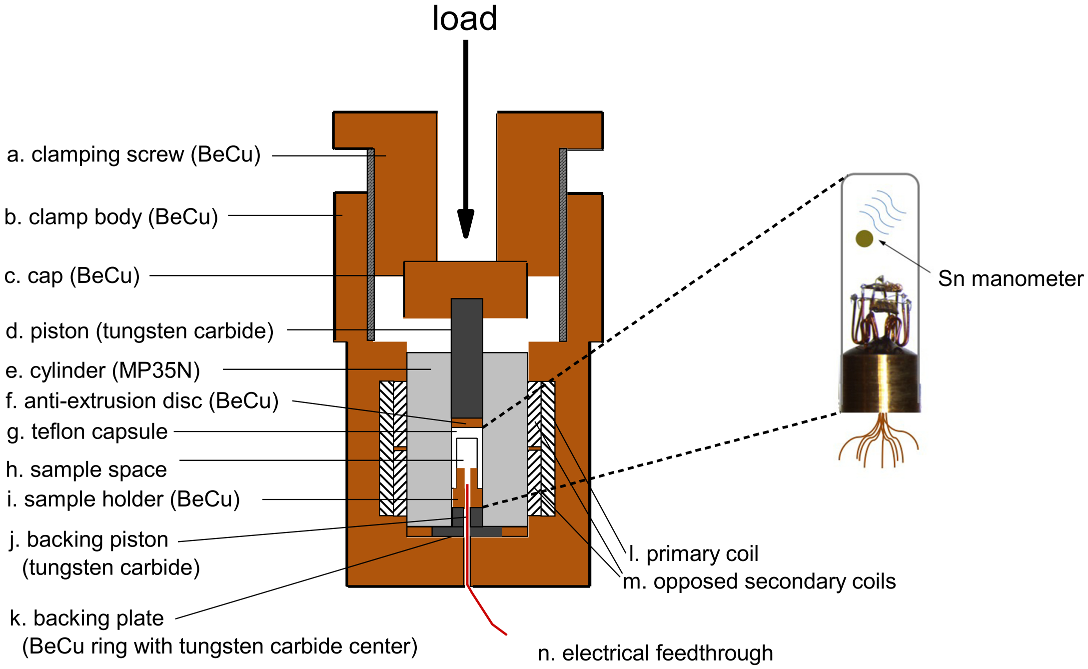

Figure 3.2: A schematic of the hydrostatic piston-cylinder cell and pressure clamp used for measurements of electrical resistivity of samples under pressure up to $P \sim 2.5$ GPa. An enlarged view of the BeCu sample holder (i) with two electrically-wired single crystal samples within the sample space (h) of the Teflon capsule (g) is shown to the right. The sample space is squeezed by applying a load up to 25,000 pounds to the BeCu cap (c) and piston (d) with a BeCu push-rod (not shown) using a hydraulic press.

medium composed of an equal parts by volume mixture of n-pentane and isoamyl alcohol which is the most hydrostatic pressure medium of choice for this type of pressure experiment. The mixture of n-pentane and isoamyl alcohol as a pressure medium has a melting point near 120 K at ambient pressure. Above 120 K, the pressure medium is liquid and the pressure environment is at its most hydrostatic. However, as the pressure-medium solidifies below 120 K, the pressure environment is subject to small shear and strain forces (see section 3.2.3 on manometry below). A load of up to 25,000 pounds is applied to the BeCu cap (c) and piston (d) with a BeCu push-rod (not shown) using a hydraulic press. The Teflon capsule (g) is squeezed to a reduced volume as it balloons out against the inside of the pre-stressed and heat-treated ultra-strong nickel-cobalt alloy MP35N cylinder (e). The applied pressure to the sample space is locked in at room temperature by turning the BeCu clamping screw (a) while the BeCu push-rod presses down on the piston. The electrical feedthrough wires (n) shown at the bottom of the clamp originate outside of the pressure cell and pass through small holes in the clamp body (b), backing plate (k), backing piston (j), and sample holder (i), into the sample space (h) to make electrical contact with the sample. A stycast epoxy is applied around the electrical feedthrough in the BeCu sample holder (i) to seal the pressure. Susceptibility coils (primary coil (l) and secondary coil (m)) are embedded within the BeCu clamp body (b) for the measurement of the superconducting transition of a tin or lead manometer inside the sample space. The BeCu clamp pictured in Fig. 3.2 is designed to lock in the pressure at room temperature and hold the pressure down to millikelvin temperatures.

3.2.2 Diamond anvil cell

The diamond anvil cell (DAC) is a direct descendent of the opposed anvil technique pioneered by P. W. Bridgman early in the 20th century. The mechanical principle behind the application of pressure in the opposed anvil configuration is: $P = F/A$, where P is pressure, F is force, and A is area. Achieving the highest of pressures then requires maximizing F and minimizing A. The conical shape of the diamond anvil (or tungsten carbide anvil in the case of the Bridgman anvil design) allows an extremely small area A to be supported by the bulk of the anvil material behind it as a force F is applied (see Fig. 3.3). Diamond anvils are well suited to achieving extremely high pressure for two reasons: (1) single crystal diamond has an extremely high incompressibility allowing it to produce a large force F to an area A and (2) the area A of the tip of the diamond anvil or

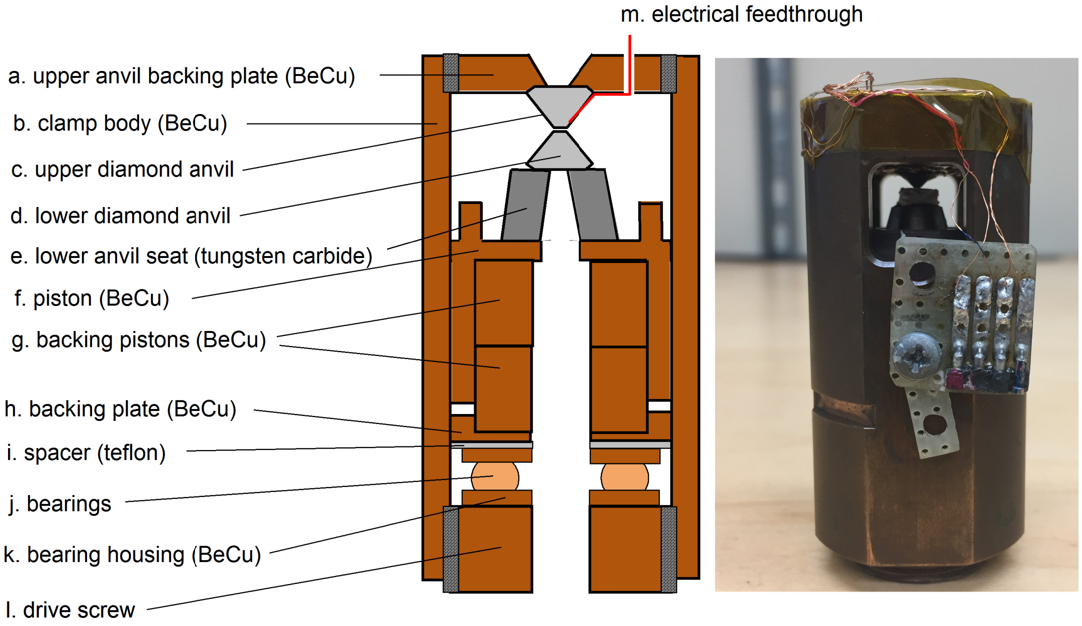

Figure 3.3: (*Left*) A schematic of the diamond anvil cell (DAC) used for measurements of electrical resistivity of samples up to pressures as high as $P \sim 40$ GPa. The sample (not shown) is located in the sample space (see Fig. 3.4) between the upper diamond anvil (c) and lower diamond anvil (d). Load is applied to the sample by driving the lower diamond anvil toward the upper diamond anvil with the BeCu drive screw (l). The bearings (j) and BeCu bearing housing (k) allow the drive screw to push on the BeCu piston assembly (piston (f), backing piston (g), backing plate (h)) without introducing unwanted friction to the cell assembly and diamond anvil. The lower and upper diamond anvils are affixed using a stycast epoxy to the lower anvil seat (e) and upper anvil backing plate (a), respectively. The electrical feedthrough (m) is connected to micro-electrodes embedded in the upper diamond anvil. Electrical contact between the micro-electrodes and the sample occurs during the application of pressure. (*Right*) A photograph of the loaded DAC used in the measurement of the TiAu sample discussed in Chapter 7.

“culet” is extremely small on the order of 150 to 300 micrometers.

A third and equally important technical aspect of the DAC design is the use of a gasket for the purpose of containing a pressure medium within the sample space between the opposed culets (see Fig. 3.4). As pressure is applied, the metal gasket extrudes around the diamond culet and seals the pressure medium, sample, and ruby sphere in the sample space between the diamond anvil faces. In additon, the compressed gasket helps to prevent the diamonds from breaking by reducing the stress to the edge of the culet. For the purpose

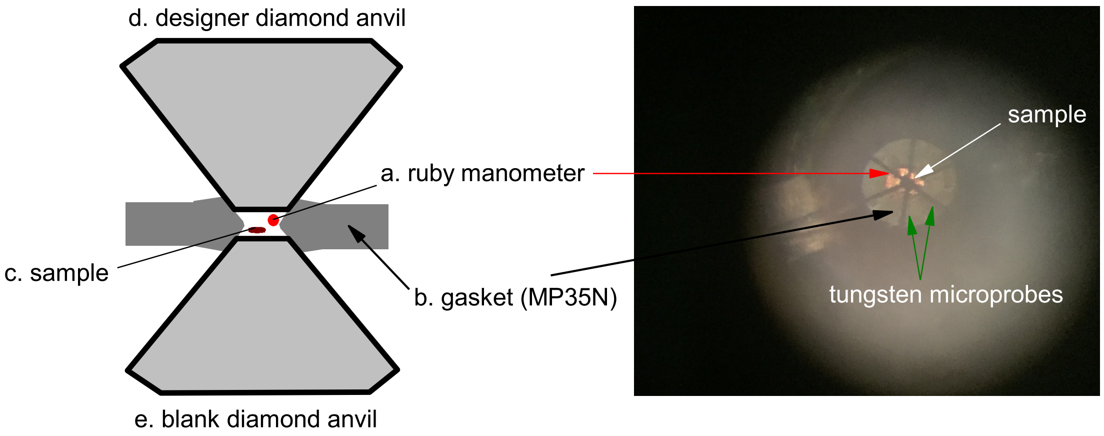

Figure 3.4: (*Left*) A schematic of the sample space in a diamond anvil cell which includes a ruby manometer (a), a gasket (b), a sample (c), and pressure medium (not shown). (*Right*) A photograph of the sample space of a DAC under pressure at ∼ 15 GPa. The photograph was taken with a cell phone looking through the eyepiece of a microscope. The lines extending radially from the sample are the tungsten electrodes. The oblong and illuminated space surrounding the sample is the deformed gasket hole under pressure. At ambient pressure, the hole is circular and can deform as the gasket extrudes under pressure. The small sphere at the border of the gasket hole is a ruby manometer on the order of 5 μm in diameter.

of preventing diamond failure, the geometry and dimensions of the gasket are important and dependent on the culet size of the diamond and the desired pressure to be reached in the experiment. The gasket is usually made of a metal foil of a thickness of 200 μm such as rhenium or MP35N, an age-hardened nickel-cobalt steel alloy. A hole must be drilled into the gasket so that it has a diameter that is roughly 1/3 to 1/2 the size of the culet diameter. For example, a 100-μm hole is appropriate for the 250 μm and 300 μm sized culets used in the DAC experiment discussed in Chapter 7. This hole must be centered on the culet (or face) of the diamond anvil. The hole is drilled into the center of the gasket with a micro electric discharge machine (micro-EDM) after the gasket has been pre-indented on the diamonds to a thickness of ∼ 40 μm for a 250 μm culet. At these dimensions, there is enough material to support the edges of the diamond culets as the gasket is compressed and extrudes around the diamond anvils.

The high pressures achieved in the diamond anvil cell, owing to the small size of the culet, come at the cost of increased difficulty in preparing the sample space for an electrical resistivity measurement. In the case of a 100-μm hole drilled in the center of an indented gasket, a sample of size on the order of $\sim$ 50 μ must be "wired" for electrical resistivity. This task is greatly simplified by modifying one of the diamond anvil culets for the purpose of making good electrical contact with the sample inside the sample space enclosed by the gasket. The modified diamond anvil or "designer diamond anvil" contains 4 or 6 or 8 electrode micro-pads on the surface of the culet that are made of tungsten. The tungsten electrodes are embedded in an epitaxial layer of high-quality single crystal diamond and extend down inside and away from the culet to the side of the anvil (see Fig. 3.4) where easy electrical connection can be made with platinum wire and the larger-guage electrical wiring of the measurement device. Electrical contact between the tungsten electrode micro-pads and the sample occurs mechanically as the sample space is closed upon the application of pressure at $\sim$ 2 GPa. The closed sample space consists of a sample in contact with the tungsten electrodes, solid steatite used as a pressure-medium, and one or more ruby spheres used as manometers to determine the pressure. The subject of manometry is discussed in the next section for both the DAC and hydrostatic piston-cylinder techniques.

3.2.3 Manometry

The measurement of pressure in both the hydrostatic piston-cylinder cell and the diamond anvil cell are conceptually simple. A carefully chosen material is selected so that one of its physical properties can be measured under pressure. The pressure dependence of the physical property is then calibrated against a known pressure marker. An important criteria for the physical property is that it is responsive enough to small changes in pressure. In the case of a hydrostatic piston-cylinder measurement, the physical property measured under pressure is the superconducting transition temperature T_c of a simple superconducting metal such as tin or lead.[1] In the case of the diamond anvil cell, the physical property measured under pressure is the ruby R1 line in the fluorescence spectrum of an irradiated grain of ruby grain of the size on the order of a few micrometers.

In the hydrostatic piston-cylinder cell, the pressure is applied at room temperature and may be determined accurately. However, there may be some relaxation of the pressure clamp and other contraction effects during cooling which can lead to some uncertainty in the final pressure at low temperatures (i.e., at the liquid helium boiling point). In particular, at low pressures less than 1 GPa, the reduction in the volume of the liquid pressure medium can result in a drop in pressure within the cell as much as 0.2 GPa.[1] At higher pressures, this effect is less, owing to the solidification of the pressure medium and to the squeezing of the Teflon capsule to smaller volume. To remove the uncertainty in determining the final pressure at low temperature, a superconducting transition of a simple well-known superconductor such as tin or lead that is sufficiently responsive to pressure is measured inductively by the coil system embedded within the piston-cylinder clamp shown in Fig. 3.2. The superconducting transition temperature T_c of high-purity (99.999%) tin was used for the determination of pressure in the piston-cylinder pressure experiments described in later chapters. A small piece of tin is placed inside the Teflon capsule during the loading of the pressure cell. At ambient pressure, $T_c = 3.72$ K for Sn which is below the liquid helium temperature of 4.22 K. In order to observe the superconducting transition, one must pump on the helium bath in the cryostat thus lowering the vapor pressure and boiling point. This is advantageous in that it allows the experimentalist more control over the rate of temperature change during the measurement of the superconducting transition. This rate should be slow and consistent across different pressure runs. By measuring the superconducting transition temperature T_c of tin and using the well known pressure dependence of $T_c(P)$, it is possible to determine the pressure P within the sample space as shown in Fig. 3.2.[1] For the pressure medium of n-pentane and isoamyl alcohol, the error in determining the pressure from the superconducting transition of Sn is approximately ± 2% for pressures below 3 GPa which is the upper bound on the pressure that can be reached with the piston-cylinder cell.[1] Figure 3.5 displays the superconducting transitions of Sn at various pressures during measurements of electrical resistivity using the piston-cylinder cell.

A determination of pressure in the diamond anvil cell is most easily made by measuring the shift of the R1 line of the ruby fluorescence spectrum of a micrometer sized ($\sim 5\ \mu$m) ruby grain. For the purpose of measuring the significant pressure gradients that can sometimes occur across the culet of the diamond, several ruby grains are carefully placed throughout the sample space enclosed by the gasket hole. The pressure can then be measured at each ruby location. After the DAC has been closed, a laser (at a power of ∼ 50 mW over a 349 to 501 nm bandwidth) is focused down the axis of the DAC (see Fig. 3.3) into the sample space containing the ruby grains. The fluorescence from the ruby under pressure is detected and measured with a spectrometer from which the wavelength of the R1 ruby line can be determined. Figure 3.5 displays the shift in the peak intensity of the R1 ruby line at various pressures up to ∼ 25 GPa during measurements of electrical resistivity of the itinerant antiferromagnetic metal alloy TiAu as discussed in Chapter 7. The peak of the R1 ruby line shifts to larger wavelengths as pressure is increased and the width of the peak is broadened at higher pressure. The wavelength λ of the R1 ruby line is used to determine the pressure P (in units of GPa) in the sample space according to the calibration equation:

$$P = \frac{A}{B}\left[\left(\frac{\lambda}{\lambda_0}\right)^{B} - 1\right], \tag{3.1}$$

where $A = 1876 \pm 6.7$, $B = 10.71 \pm 0.14$, and λ_0 is the peak wavelength of the ruby R1 line at atmospheric pressure.[2] The reference wavelength $\lambda_0 = 694.26$ nm at atmospheric pressure was measured from the fluorescence spectrum of an irradiated ruby on a glass slide. In contrast to the low-temperature manometry used in the piston-cylinder cell, the measurement of pressure in the DAC using the ruby fluorescence method is performed at

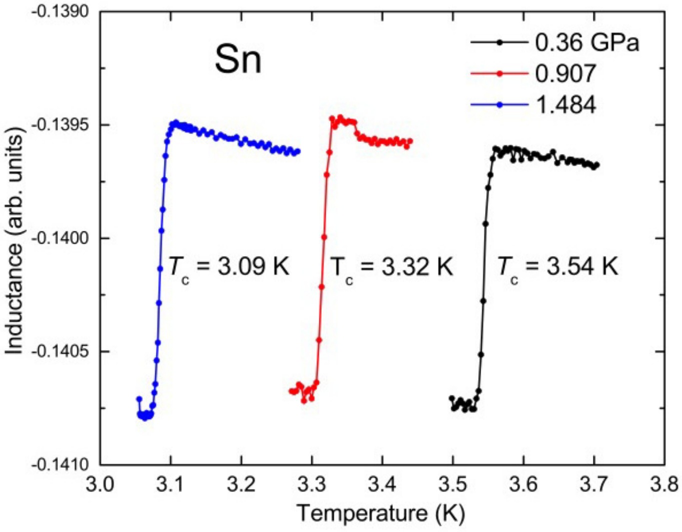

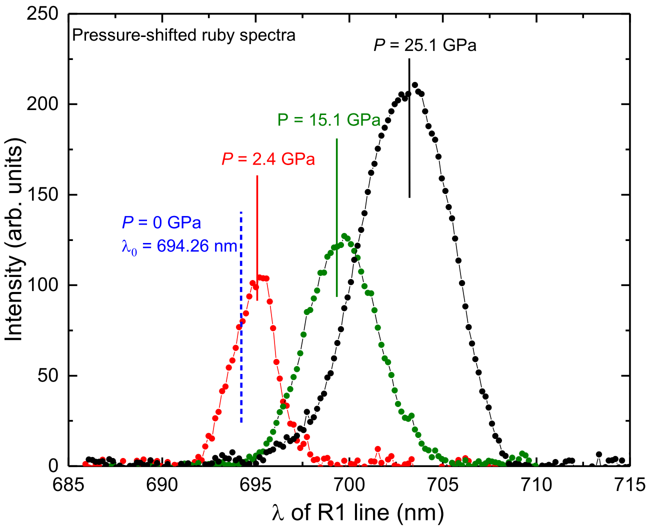

Figure 3.5: (*Top*) Superconducting transitions of a Sn manometer at various pressures in a hydrostatic piston-cylinder cell. The superconducting transitions were measured inductively from an ac susceptibility coil system embedded in the piston-cylinder pressure clamp. (*Bottom*) A plot of the peak intensity of the R1 ruby line at various pressures up to $\sim$ 25 GPa during measurements of electrical resistivity of the itinerant antiferromagnetic metal alloy TiAu as discussed in Chapter 7. The solid vertical lines indicate the location of the wavelength at the peak. These and other values for the peak λ were used in determining the pressure in the DAC based on the expression in Equation 3.1. The reference wavelength λ_0 is indicated by the blue dotted line but the spectrum at atmospheric pressure is not shown.

room temperature. Upon cooling, some relaxation and differential contraction can occur in the DAC resulting in a reduction of pressure. However, the change in pressure is within the error of ~ 1 GPa across the sample space of the DAC owing to pressure gradients and strain in the quasi-hydrostatic sample space environment.

Blbliography

[1] T. F. Smith, C. W. Chu, and M. B. Maple, “Superconducting manometers for high pressure measurement at low temperature”, Cryogenics **9**, 53 (1969).

[2] A. D. Chijioke, W. J. Nellis, A. Soldatov, and I. F. Silvera, “The ruby pressure standard to 150GPa”, J. App. Phys. **98**, 114905 (2005).

Chapter 4

Pressure-induced enhancement of superconductivity and suppression of semiconducting behavior in the $LnO_{0.5}F_{0.5}BiS_2$ (Ln = La, Ce) compounds

4.1 Introduction

Superconductivity with a superconducting critical temperature T_c = 8.6 K has recently been reported in the layered compound $Bi_4O_4S_3$. [1, 2] Following this report, other BiS_2-based superconductors including $LnO_{1-x}F_xBiS_2$ (Ln = La, Ce, Pr, Nd, Yb) with a T_c as high as 10.6 K have been synthesized and studied.[3–12] More recent work demonstrates that chemical substitution of the tetravalent ions Th^{+4}, Hf^{+4}, Zr^{+4} and Ti^{+4} for trivalent lanthanum, La^{+3}, in $LaOBiS_2$ increases the charge-carrier density and induces superconductivity.[13] Most of the research on the layered BiS_2 compounds has heretofore centered on the effect of chemical substitution on superconductivity. Application of an external pressure may also be employed as a method for reducing the unit cell volume of these compounds and studying the resultant effect on superconductivity. In this paper, we report measurements of the pressure dependence of the normal state electrical resistivity between 1 K and 300 K and T_c at various pressures up to $\sim$ 3 GPa for the compounds $\mathrm{LaO_{0.5}F_{0.5}BiS_2}$ and $\mathrm{CeO_{0.5}F_{0.5}BiS_2}$. We compare our results to recently reported studies of $\mathrm{LaO_{0.5}F_{0.5}BiS_2}$ samples synthesized under high pressure by Kotegawa *et al.* [7]

The qualitative evolution of T_c with pressure is markedly similar for both the $\mathrm{LaO_{0.5}F_{0.5}BiS_2}$ and $\mathrm{CeO_{0.5}F_{0.5}BiS_2}$ compounds, which have T_c values (at atmospheric pressure) of 3.3 K and 2.2 K, respectively. For both compounds, T_c initially increases, reaches a maximum value of 10.1 K at $\sim$ 1 GPa for $\mathrm{LaO_{0.5}F_{0.5}BiS_2}$ and 6.7 K at $\sim$ 2 GPa for $\mathrm{CeO_{0.5}F_{0.5}BiS_2}$, and then gradually decreases with increasing pressure. Both compounds also exhibit striking transient behavior in the region between the lower T_c phase near atmospheric pressure and the higher T_c phase at higher pressures. This transient region is characterized by a rapid increase of T_c and an increase of the superconducting transition width ΔT_c, in which both T_c and ΔT_c are reversible with increasing and decreasing pressure cycles. This occurs over a range in pressure from $\sim$ 0.5 GPa to 1.1 GPa for $\mathrm{LaO_{0.5}F_{0.5}BiS_2}$ and from $\sim$ 0.5 GPa to 1.5 GPa for $\mathrm{CeO_{0.5}F_{0.5}BiS_2}$. In both materials, there is a sizable pressure-induced suppression of semiconducting behavior exhibiting hysteresis up to the pressure at which the maximum value of T_c is found. The rapid increase of the charge carrier density inferred from the suppression of the semiconducting behavior correlates with the rapid increase of T_c in this region. At pressures above the value at which the maximum in T_c occurs, there is a gradual decrease of T_c and further suppression of the semiconducting behavior with pressure, both of which are reversible.

4.2 Experimental Details

Polycrystalline samples of $Ln\mathrm{O}_{1-x}\mathrm{F}_x\mathrm{BiS}_2$ (Ln = La, Ce) with $x = 0.5$ were prepared by solid-state reaction using powders of La_2O_3 (99.9%), LaF_3 (99.9%), La_2S_3 (99.9%), and Bi_2S_3 (99.9%) for $\mathrm{LaO}_{1-x}\mathrm{F}_x\mathrm{BiS}_2$, and powders of CeF_3 (99.9%) and CeO_2 (99.9%) for $\mathrm{CeO}_{1-x}\mathrm{F}_x\mathrm{BiS}_2$. Bi_2S_3 precursor powder was prepared in an evacuated quartz tube by reacting Bi (99.99%) and S (99.9%) at 500°C for 10 hours. The $Ln_2\mathrm{S}_3$ (Ln = La, Ce) precursor powders were prepared in an evacuated quartz tube by reacting chunks of La and Ce with S grains at 800°C for 12 hours. The starting materials with nominal composition $Ln\mathrm{O}_{0.5}\mathrm{F}_{0.5}\mathrm{BiS}_2$ (Ln = La, Ce) were weighed, thoroughly mixed, pressed into pellets, sealed in evacuated quartz tubes, and annealed at 800°C for 10 hours. The products were then ground, mixed for homogenization, pressed into pellets, and annealed again in evacuated quartz tubes at 800°C for 10 hours. X-ray powder diffraction measurements were made using an X-ray diffractometer with a Cu K_α source to assess phase purity and to determine the crystal structure of the $Ln\mathrm{O}_{0.5}\mathrm{F}_{0.5}\mathrm{BiS}_2$ (Ln = La, Ce) compounds. Lattice parameters for $\mathrm{LaO}_{0.5}\mathrm{F}_{0.5}\mathrm{BiS}_2$ are a = 4.0613 Å and c = 13.3157 Å, while for $\mathrm{CeO}_{0.5}\mathrm{F}_{0.5}\mathrm{BiS}_2$ the lattice parameters are a = 4.0398 Å and c = 13.4513 Å. [12]

Measurements of $\rho(T)$ under applied pressure were performed up to $\sim$ 3 GPa in a clamped piston cylinder pressure cell between $\sim$ 1 K and 300 K in a pumped ^{4}He dewar. A 1:1 by volume mixture of n-pentane and isoamyl alcohol was used to provide a quasi-hydrostatic pressure transmitting medium. A second set of electrical resistivity measurements were performed by releasing pressure from the pressurized cell down to atmospheric pressure. Annealed Pt leads were affixed to gold-sputtered contact surfaces on each sample with silver epoxy in a standard four-wire configuration. The pressure dependent superconducting T_c of high purity Sn, measured inductively, was used as a manometer and calibrated against data from Smith.[14]

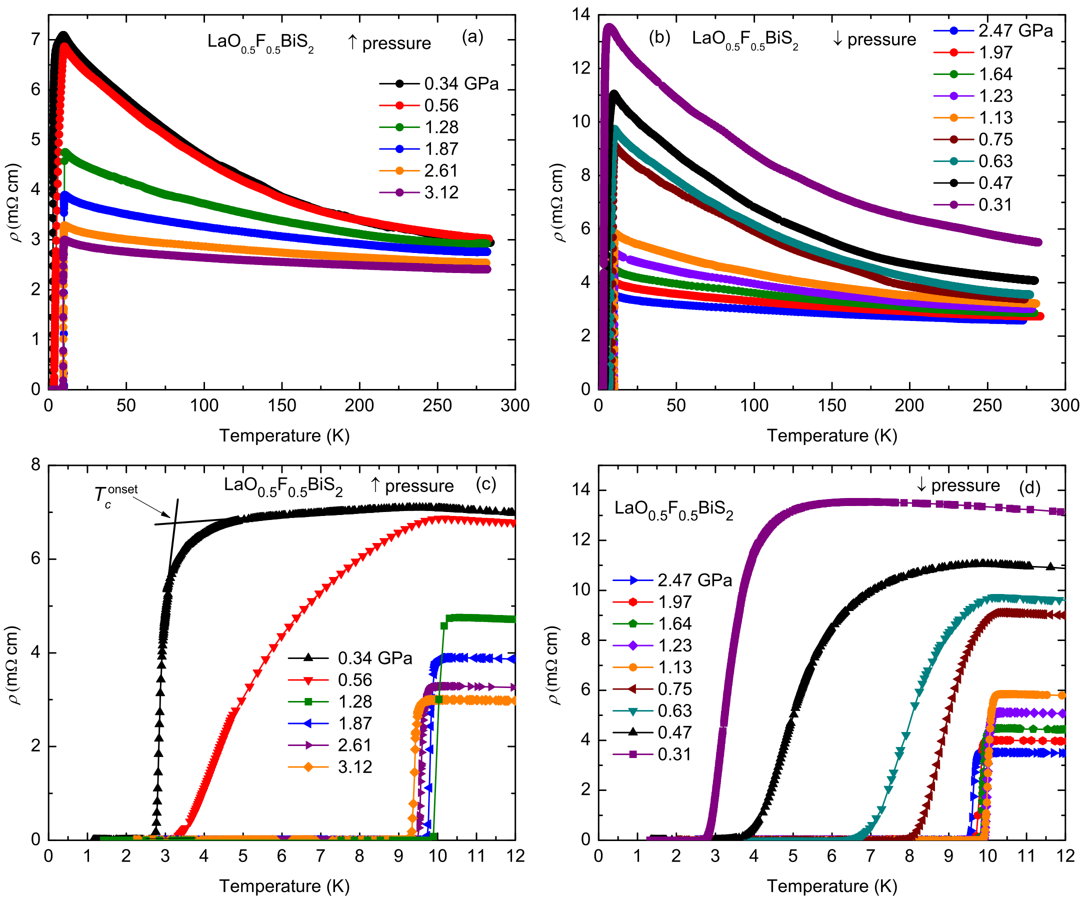

Figure 4.1: (a) (b) Temperature dependence of electrical resistivity, ρ, for the $LaO_{0.5}F_{0.5}BiS_2$ sample at various pressures upon (a) increasing and (b) decreasing pressure. The electrical resistivity $\rho(T)$ is suppressed with increasing pressure as seen from the flattening of the curves at higher pressure. (c) (d) Resistive superconducting transition curves for $LaO_{0.5}F_{0.5}BiS_2$ upon (c) increasing and (d) decreasing pressure. T_c increases from 2.9 K to a maximum of 10.1 K before gradually decreasing.

4.3 Results and Discussion

The temperature dependence of the electrical resistivity, ρ, below 300 K for the $LaO_{0.5}F_{0.5}BiS_2$ compound at various pressures is displayed in Fig. 4.1. Figure 4.1(a) shows $\rho(T)$ upon increasing pressure to 3.1 GPa, while Fig. 4.1(b) gives $\rho(T)$ upon decreasing pressure back down to 0.31 GPa. The temperature dependence of $\rho(T)$ at lower pressures exhibits semiconducting behavior. The semiconducting behavior is suppressed with increasing pressure as seen from the nearly constant $\rho(T)$ curves above 2 GPa. A comparison of Fig. 4.1(a) with Fig. 4.1(b) shows that the suppression of $\rho(T)$ is continuous and reversible over the full range 0.3 - 3.1 GPa. At pressures above 2 GPa where suppression is greatest, the values of $\rho(T)$ are comparable in Fig. 4.1(a) and Fig. 4.1(b) and reversible with pressure. However, whereas the suppression of $\rho(T)$ is reversible with pressure, the magnitude of $\rho(T)$ exhibits hysteretic behavior with pressure. At lower pressures, measurements of $\rho(T)$ made during release of pressure yield higher values than $\rho(T)$ measurements performed upon increasing pressure. The difference between $\rho(T)$ measurements made during increasing pressure and those made during decreasing pressure are largest at lower pressures where the rate of suppression of semiconducting behavior is largest. After a release in pressure to the lowest value of 0.31 GPa, the maximum value of ρ is nearly 14 mΩ cm. This is a factor of 2 larger than the corresponding value along the increasing pressure path at 0.34 GPa.

Superconducting transitions at low temperature were measured upon increasing and then releasing pressure as shown in Fig. 4.1(c) and Fig. 4.1(d), respectively. There is a striking similarity in the qualitative behavior and evolution of the transitions in both plots. For pressures in the range 0.5 GPa to 1.0 GPa, the superconducting transitions broaden significantly. For higher pressures above 1.0 GPa, the transition curves begin to sharpen again at approximately 10 K. It is in this higher pressure region where T_c passes through a maximum of 10.1 K at $\sim$ 1 GPa and then gradually decreases as pressure increases. The evolution of both the value of the superconducting critical temperature T_c and the superconducting transition width ΔT_c defined by the procedure described in the text, were reversible with respect to both increasing and decreasing pressure. T_c was defined as the temperature at which ρ falls to 50% of its value at the temperature of the onset of superconductivity, T_c^{onset}, with T_c^{onset} determined as illustrated in Fig. 4.1(c). The temperature where the resistivity vanishes, T_0, was determined in a similar fashion as T_c^{onset} using a linear extrapolation of the resistive superconducting curve to $\rho = 0$. In determining T_c for

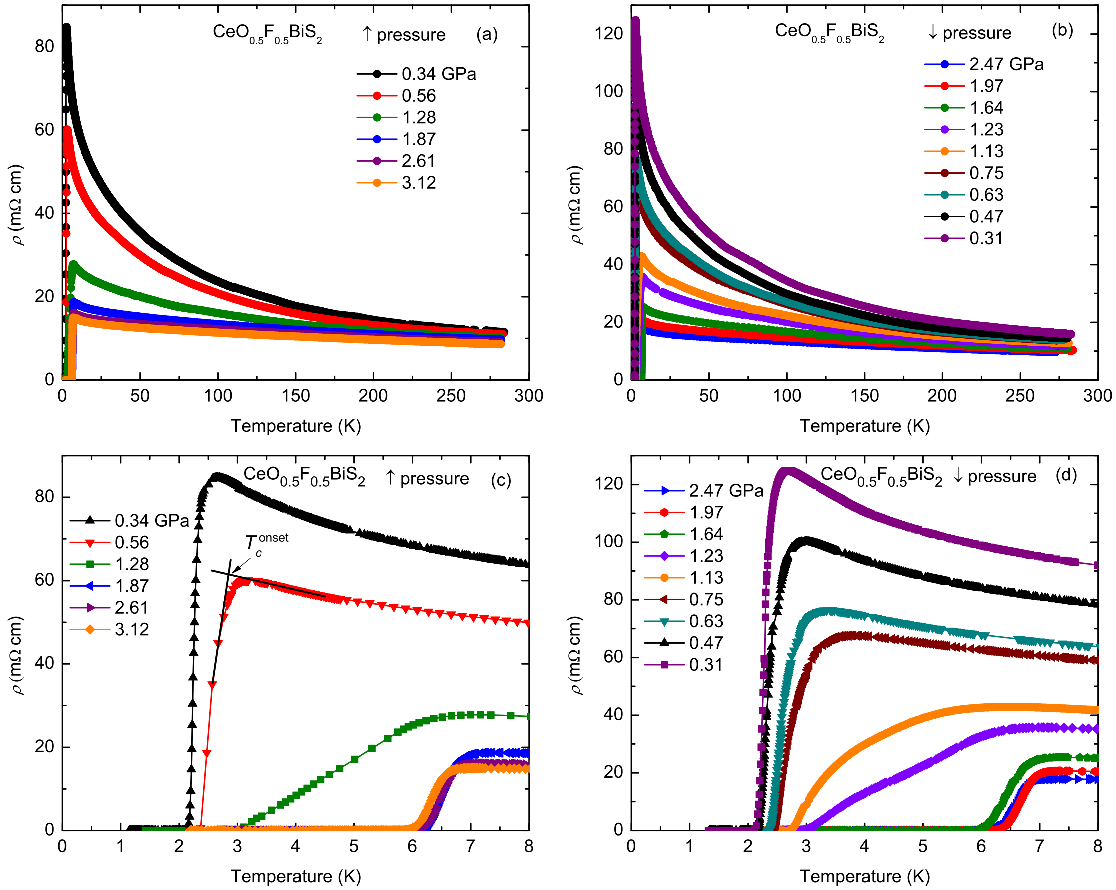

Figure 4.2: (a) (b) Temperature dependence of electrical resistivity, ρ, for the $CeO_{0.5}F_{0.5}BiS_2$ sample at various pressures upon (a) increasing pressure and (b) decreasing pressure. At lower pressures, the compound exhibits semiconducting behavior. The semiconducting behavior is suppressed at higher pressure as seen from the flattening of the curves. (c) (d) Resistive superconducting transition curves for $CeO_{0.5}F_{0.5}BiS_2$ at various pressures upon (c) increasing and (d) decreasing pressure. T_c increases from 2.3 K to a maximum of 6.7 K before gradually decreasing.

the broader transitions, we used the same criteria as for the sharper transitions; however, we make note of the less definitive T_c for these broader transitions.

Measurements performed on $CeO_{0.5}F_{0.5}BiS_2$ reveal remarkably similar behavior to the results for $LaO_{0.5}F_{0.5}BiS_2$. As shown in Fig. 4.2, the qualitative behavior of the results are reversible upon application and release of pressure. Measurements of $\rho(T)$ show semiconducting behavior which is suppressed at higher pressures. As pressure is released, the semiconducting behavior is recovered. The measured values of $\rho(T)$ are higher along

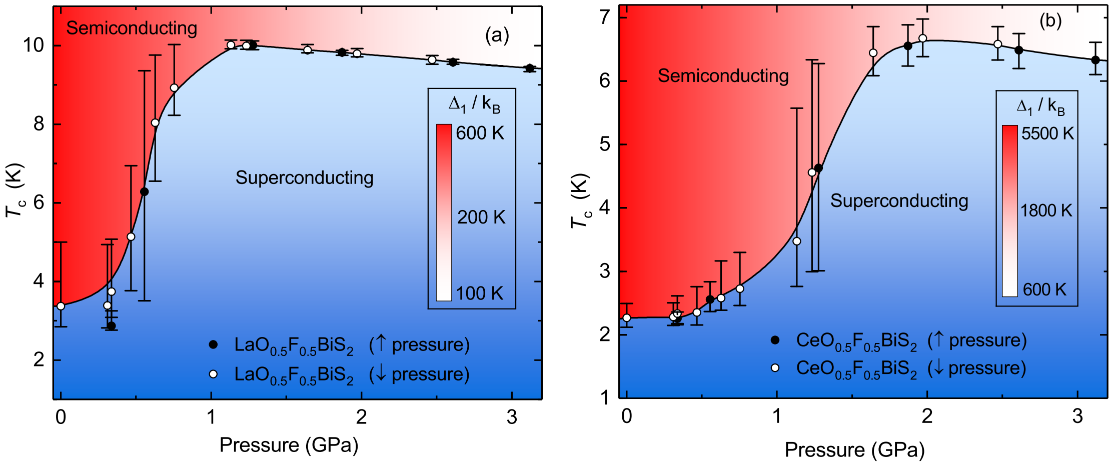

Figure 4.3: Phase diagrams for (a) $LaO_{0.5}F_{0.5}BiS_2$ and (b) $CeO_{0.5}F_{0.5}BiS_2$ under pressure. T_c was defined as the temperature at which the electrical resistivity, ρ, falls to 50% of its value at the temperature of the onset of superconductivity, T_c^{onset}. The vertical bar lengths indicate the superconducting transition width ΔT_c and vertical bar caps indicate T_c^{onset} (upper) and T_0 (lower). Filled symbols denote measurements performed upon increasing pressure, while open symbols represent measurements made upon decreasing pressure. The solid black curves are guides to the eye. The change in color in the semiconducting normal state region represents the suppression of the semiconducting behavior with pressure as manifested in the decrease of the larger energy gap Δ_1 whose values are indicated in the legend.

the reversed path during a release of pressure. The discrepancy between $\rho(T)$ measurements made during increasing pressure and those made during decreasing pressure are largest at lower pressures where the rate of suppression of the semiconducting behavior is largest. After releasing the pressure to the lowest value of 0.31 GPa, ρ is nearly 130 mΩ cm; this is a factor of 1.5 larger than the corresponding value along the increasing pressure path at 0.34 GPa.

Superconducting transitions at low temperature were measured for $CeO_{0.5}F_{0.5}BiS_2$ while increasing and then decreasing pressure. The trend and character of the transitions are reversible upon application and subsequent release of pressure as seen from a comparison of Fig. 4.2(c) and Fig. 4.2(d). Similar to the evolution of T_c in $LaO_{0.5}F_{0.5}BiS_2$, sharp superconducting transitions are observed at low pressures up to approximately 0.5

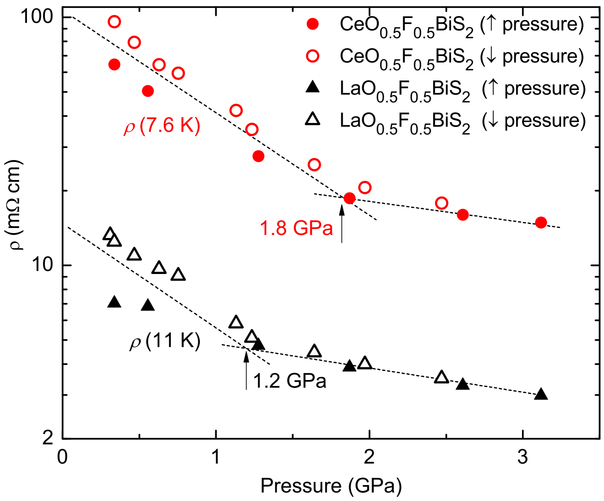

Figure 4.4: Electrical resistivity, ρ, in the normal state just above the superconducting onset temperature, T_c^{onset}. Electrical resistivity values for $CeO_{0.5}F_{0.5}BiS_2$ were taken at T = 7.6 K, while ρ values for $LaO_{0.5}F_{0.5}BiS_2$ were taken at T = 11 K. Filled (open) symbols represent measurements upon increasing (decreasing) pressure. Dotted lines reflect the slopes (suppression rates), and arrows point to changing slopes at $\sim$ 1.2 GPa and $\sim$ 1.8 GPa in $LaO_{0.5}F_{0.5}BiS_2$ and $CeO_{0.5}F_{0.5}BiS_2$, respectively. The break in slope occurs at a pressure near that at which T_c reaches a maximum for both $LaO_{0.5}F_{0.5}BiS_2$ and $CeO_{0.5}F_{0.5}BiS_2$.

GPa before they begin to broaden. From both the increasing and decreasing pressure plots (Fig. 4.2(c) and Fig. 4.2(d), respectively), the transitions begin to broaden significantly up to pressures of approximately 1.5 GPa. At pressures above 1.5 GPa, the superconducting transitions become sharp again. It is in this pressure region where T_c passes through a maximum of 6.7 K at $\sim$ 2 GPa and then decreases gradually at higher pressures.

Figure 4.3 summarizes the results for the superconducting phase diagram, $T_c(P)$, for both the $LaO_{0.5}F_{0.5}BiS_2$ and $CeO_{0.5}F_{0.5}BiS_2$ compounds. The measurements were performed first by increasing the pressure monotonically in six steps (filled symbols) up to 3.1 GPa, followed by a monotonic decrease in pressure in nine steps (open symbols) back down to 0.31 GPa. The phase diagram indicates $T_c(P)$ is highly reversible for both compounds; negligible pressure hysteresis is observed even in the regions where the resistive transition broadens significantly.

The phase diagram in Fig. 4.3 shows T_c maxima for both the $LaO_{0.5}F_{0.5}BiS_2$ and $CeO_{0.5}F_{0.5}BiS_2$ compounds. In the case of $LaO_{0.5}F_{0.5}BiS_2$, T_c initially increases with pressure up to a maximum of 10.1 K at 1.1 GPa. T_c then gradually decreases with a slope of -0.30 K GPa^{-1}. This T_c maximum is also preceded by a reversible broadening of the superconducting transition in the pressure range 0.5 - 1.0 GPa, represented as elongated vertical bars in Fig. 4.3. In the normal state (above the $T_c(P)$ curve), the semiconducting behavior of $LaO_{0.5}F_{0.5}BiS_2$ is continuously suppressed with pressure as manifested in a larger energy gap Δ_1 that decreases with pressure, the values of which are indicated in the legend. The determination of the energy gaps Δ_1 and Δ_2 from the $\rho(T,P)$ data are discussed below. This maximum in $T_c(P)$ at 1.1 GPa occurs in the vicinity of a change of slope in the normal state $\log(\rho)$ vs. P curve, measured at 11 K, as shown in Fig. 4.4.

In the case of $CeO_{0.5}F_{0.5}BiS_2$, T_c initially increases to a maximum of 6.7 K at $\sim$ 2 GPa and then decreases slowly with a slope of -0.30 K GPa^{-1} at higher pressures. Leading up to this maximum is a reversible broadening of the superconducting transition in the region 0.5 - 1.5 GPa depicted by the lengthened vertical bars in Fig. 4.3. In the normal state (above the $T_c(P)$ curve), the semiconducting behavior of $CeO_{0.5}F_{0.5}BiS_2$ is also continuously suppressed with pressure as manifested in a larger energy gap Δ_1 that decreases with pressure, the values of which are indicated in the legend. The maximum in $T_c(P)$ at 2 GPa also occurs in the vicinity of a slope change in $\log(\rho)$ vs. P, measured at 7.6 K, as shown in Fig. 4.4.

The width of the superconducting transitions in the broadening region, represented by the vertical bars in Fig. 4.3, is $\Delta T_c \sim$ 4 - 6 K. Pressure gradients in the piston-cylinder cell were estimated from the error in pressure to be of the order $\Delta P \sim \pm$ 0.05 GPa where the error in pressure was determined from the width of the superconducting transition of the Sn manometer. It is possible to relate ΔT_c and ΔP through the slope of $T_c(P)$ in

Fig. 4.3 so that $\Delta T_c \simeq (dT_c(P)/dP)\Delta P$. Even though ΔP is small and constant for pressures measured as part of this study, ΔT_c can be large when $dT_c(P)/dP$ is large (*i.e.*, in the pressure region where broadened transitions are observed). Rough estimates of ΔT_c were made using ΔP = 0.1 GPa and slopes of 18 K/GPa and 11 K/GPa for $LaO_{0.5}F_{0.5}BiS_2$ and $CeO_{0.5}F_{0.5}BiS_2$, respectively. These calculations yield values of ΔT_c = 1.8 K and 1.1 K for $LaO_{0.5}F_{0.5}BiS_2$ and $CeO_{0.5}F_{0.5}BiS_2$, respectively, which are of the correct order of magnitude. The size of the vertical bars characterizing ΔT_c also appear to qualitatively track with the local slope of $T_c(P)$ for most pressures in Fig. 4.3.

Kotegawa *et al* [7] previously reported the pressure dependence of T_c for those $LaO_{0.5}F_{0.5}BiS_2$ samples that were synthesized under high pressure, which apparently exhibit only the high T_c phase uncovered in the present study. In their experiments, it was found that T_c exhibits a maximum of 10.6 K at $\sim$1 GPa and then gradually decreases with a slope of -0.40 K/GPa (compared to -0.30 K/GPa in this study) at pressures above 1 GPa. The low T_c phase and broadened superconducting transitions bridging the low T_c and high T_c phases, however, are not present in their $T_c(P)$ phase diagram. The presence of only the high T_c phase at ambient pressure in the study by Kotegawa *et al.*[7] suggests that synthesis of the $LaO_{0.5}F_{0.5}BiS_2$ samples under high pressure has already induced the high T_c superconducting phase.

From the plot of log(ρ) vs. P at low temperature displayed in Fig. 4.4, there is a noticeable change in the magnitude of the suppression rate, dlog(ρ)/dP, for both the $LaO_{0.5}F_{0.5}BiS_2$ and $CeO_{0.5}F_{0.5}BiS_2$ compounds. In the case of $LaO_{0.5}F_{0.5}BiS_2$, there is a strong suppression of resistivity up to $\sim$ 1.2 GPa, followed by a weaker suppression at higher pressures. In the case of $CeO_{0.5}F_{0.5}BiS_2$, there is a strong suppression of resistivity up to $\sim$ 1.8 GPa, followed by a weaker suppression at higher pressures. The $\rho(P)$ data for $LaO_{0.5}F_{0.5}BiS_2$ and $CeO_{0.5}F_{0.5}BiS_2$ were taken in the normal state at 11 K and 7.6 K, respectively. These temperatures occur just above the onset of the superconducting transi-

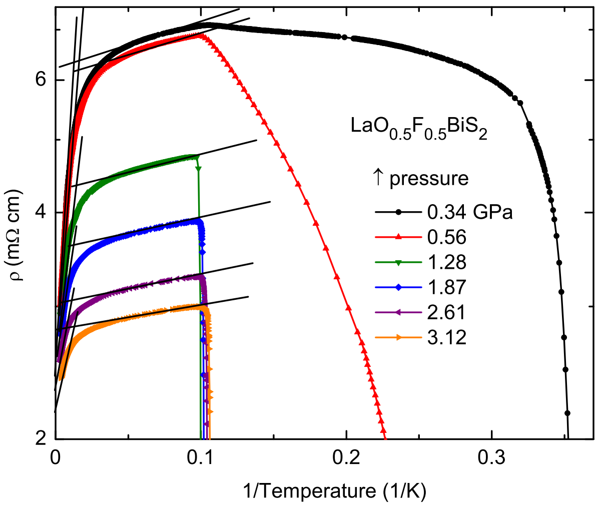

Figure 4.5: $\log(\rho)$ vs. $1/T$ up to 3.12 GPa for $LaO_{0.5}F_{0.5}BiS_2$. The solid lines represent linear fits of Eq. (4.1) from which the high and low temperature gaps Δ_1 and Δ_2, respectively, were determined.

tion at T_c^{onset}. The dotted lines in Fig. 4.4 are guides to the eye for the rates of suppression of $\log(\rho)$ with pressure.

There is a correlation between the pressure at which the maximum T_c occurs in the $T_c(P)$ phase diagram of Fig. 4.3 and the pressure where the suppression rate changes in the plot of $\log(\rho)$ vs. P in Fig. 4.4. For $LaO_{0.5}F_{0.5}BiS_2$, this "critical pressure" occurs at $\sim$ 1.2 GPa, while for $CeO_{0.5}F_{0.5}BiS_2$ it is located at $\sim$ 1.8 GPa. In both compounds, there is also an apparent pressure hysteresis as seen from the separation between the increasing pressure data (open symbols) and the decreasing pressure data (filled symbols). This pressure hysteresis becomes more pronounced where the suppression rate is higher; i.e., below the previously mentioned critical pressures.

The semiconducting behavior of the $\rho(T)$ data and its rapid suppression with pressure was noted in the work of Kotegawa *et al.*[7] on the $LaO_{0.5}F_{0.5}BiS_2$ compound synthesized under high pressure. They observed that the resistivity could be described over two distinct regions by the relation,

$$\rho(T) = \rho_0 e^{\Delta/2k_BT} \tag{4.1}$$

where ρ_0 is a constant and Δ is an energy gap. Analysis of the $\rho(T)$ data at atmospheric pressure in these two regions, 200 - 300 K and T_c - 20 K, yielded energy gaps $\Delta_1/k_B \approx 140$ K and $\Delta_2/k_B \approx 1.86$ K, respectively. Both energy gaps Δ_1 and Δ_2 were found to decrease with pressure. In this study, we have also determined values of the energy gaps Δ_1 and Δ_2 from linear fits of $\rho(T)$ data on a plot of log(ρ) vs. 1/T, as illustrated in Fig. 4.5, which displays our $\rho(T)$ data for $LaO_{0.5}F_{0.5}BiS_2$ upon increasing pressure. From similar plots for $LaO_{0.5}F_{0.5}BiS_2$ upon decreasing pressure as well as for $CeO_{0.5}F_{0.5}BiS_2$ upon increasing and decreasing pressure, the two energy gaps Δ_1 and Δ_2, corresponding to the high and low temperature regions, respectively, could also be extracted.

The behavior of both of the energy gaps Δ_1 and Δ_2 as a function of pressure for both $LaO_{0.5}F_{0.5}BiS_2$ and $CeO_{0.5}F_{0.5}BiS_2$ are shown in Fig. 4.6. The energy gaps decrease rapidly with pressure, similar to the behavior observed by Kotegawa *et al.*[7] However, it is interesting to note that the values of the energy gaps for $LaO_{0.5}F_{0.5}BiS_2$ at atmospheric pressure shown in Fig. 4.6 are considerably larger than the values obtained by Kotegawa *et al.*[7] The energy gaps Δ_1 and Δ_2 both exhibit hysteretic behavior below a critical pressure of $\sim$ 1.3 GPa for $LaO_{0.5}F_{0.5}BiS_2$ and $\sim$ 2 GPa for $CeO_{0.5}F_{0.5}BiS_2$; these critical pressures correlate with the pressures where the slope, dlog(ρ)/dP, changes (at temperatures in the normal state right above T_c) in the log(ρ) vs. P plots (Fig. 4.4) and also correlate with the transition pressures into the high T_c phase for both $LaO_{0.5}F_{0.5}BiS_2$ and $CeO_{0.5}F_{0.5}BiS_2$ (Fig. 4.3).

Specific heat C(T) measurements at ambient pressure have recently been made on both the $LaO_{0.5}F_{0.5}BiS_2$ and $CeO_{0.5}F_{0.5}BiS_2$ compounds.[12] The samples in Ref. Yazici [12] and in the present study were from the same batch. In the case of $LaO_{0.5}F_{0.5}BiS_2$,

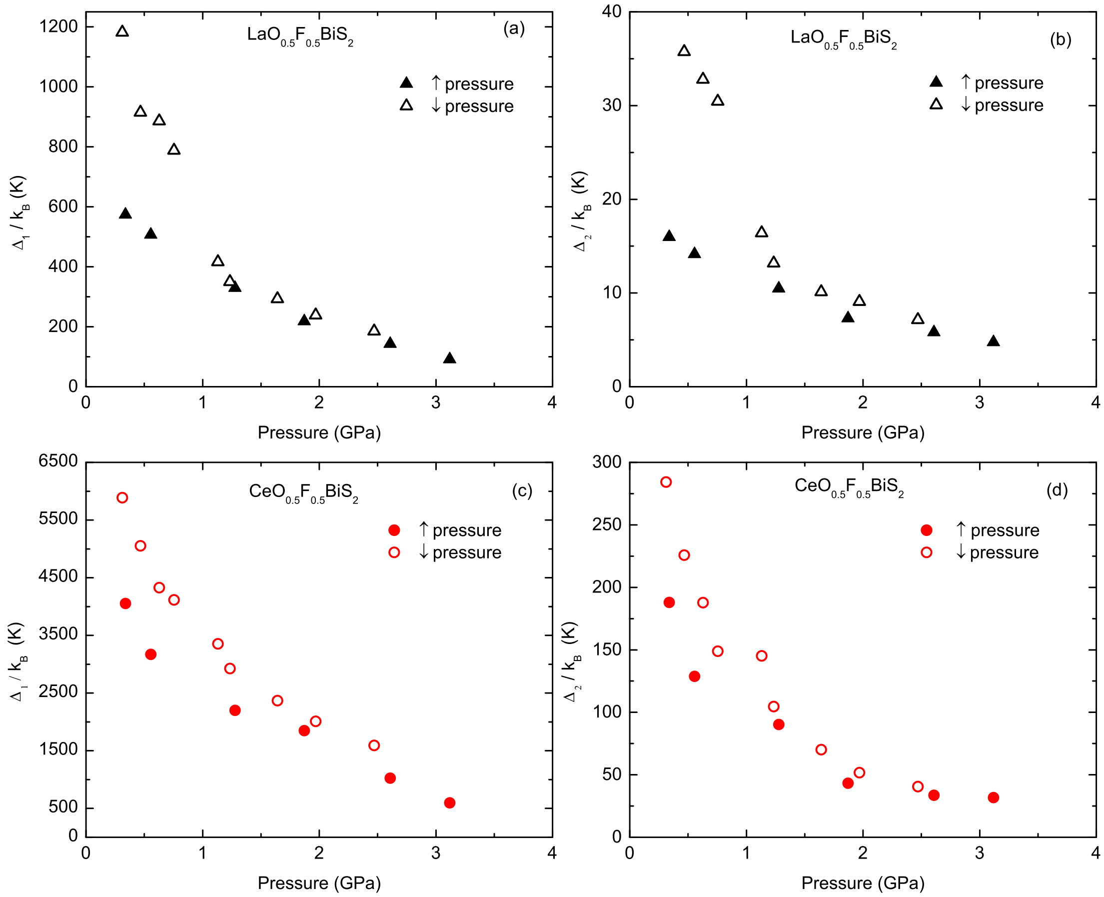

Figure 4.6: (a),(b) Energy gaps Δ_1 and Δ_2 plotted as a function of pressure for $LaO_{0.5}F_{0.5}BiS_2$; (c),(d) Energy gaps Δ_1 and Δ_2 plotted as a function of pressure for $CeO_{0.5}F_{0.5}BiS_2$. Energy gaps were fitted to Eq. (4.1) using the data shown in Fig. 4.5. Filled (open) symbols were obtained upon increasing (decreasing) pressure cycles.

these C(T) measurements suggest that the superconductivity observed at $\sim$ 3 K for pressures less than $\sim$ 0.5 GPa is a bulk phenomenon. In Fig. 5 of Ref. Yazici [12], there is a clear jump in C(T)/T at T_c = 2.93 K. This value of T_c is close to the temperature where ρ vanishes in $LaO_{0.5}F_{0.5}BiS_2$. We expect, therefore, that the $LaO_{0.5}F_{0.5}BiS_2$ sample in this study exhibits bulk superconductivity at lower pressures.

It is still unclear whether or not the higher T_c superconducting transitions at pressures above 0.5 GPa are associated with bulk superconductivity. The narrow widths of the superconducting transitions would seem to suggest that the superconductivity in this pressure range is a bulk phenomenon. However, the sharpness of the resistive transitions is also consistent with a filamentary zero resistance path through the sample with a narrow distribution of T_c values that could be due to small amounts of a superconducting phase, rather than bulk superconductivity. High pressure magnetization measurements in a SQUID magnetometer were performed on several pieces of $\mathrm{LaO_{0.5}F_{0.5}BiS_2}$ to determine the character of the 10 K superconducting phase by Taufour, Bud'ko and Canfield. [15] It was difficult to observe a diamagnetic signal against the large background from the pressure cell. This suggests possible inhomogeneity in the $\mathrm{LaO_{0.5}F_{0.5}BiS_2}$ sample.

In the case of $\mathrm{CeO_{0.5}F_{0.5}BiS_2}$, however, there is no indication in the ambient pressure C(T) measurements of bulk superconductivity.[12] The lack of a discernible jump in specific heat, however, could be due to sample inhomogeneity and/or the proximity of T_c = 1.9 K to the base temperature T = 1.8 K of the specific heat measurements and needs to be investigated further.

The rapid increase of T_c and broadening of the superconducting transition with pressure, as well as its reversibility with pressure for both compounds, suggest the existence of a gradual, pressure-induced transition between superconducting phases with a lower T_c at lower pressure and a higher T_c at higher pressure. The broadening of the superconducting transition feature in the transition region, $\sim$1 GPa wide for both compounds, could be a consequence of the large slope of $T_c(P)$ in that pressure range (*i.e.*, $\Delta T_c \simeq (dT_c(P)/dP)\Delta P$). It might also be due to a spatial distribution of the two phases in the transition region. In this latter scenario, as the applied pressure is increased in the transition region, the amount of the high pressure phase grows at the expense of the low pressure phase, until the sample is completely transformed into the high pressure phase at the end of the transition region. The markedly similar features in the T_c versus pressure diagrams shown in Fig. 4.3 for the two compounds $Ln\mathrm{O}_{1-x}\mathrm{F}_x\mathrm{BiS}_2$ (Ln = La, Ce) suggests that this behavior could be characteristic in general of the entire class of $Ln\mathrm{O}_{1-x}\mathrm{F}_x\mathrm{BiS}_2$ materials.

One possible explanation for this behavior is that there is a distribution of pressures at which the transformation between the two phases takes place within the transition region. This distribution could be associated with some type of inhomogeneity (either electronic or atomic) in the samples. Experiments are currently in progress to search for a possible pressure-induced structural transition in these materials and to see whether the pressure-induced transition can be sharpened by improving the synthesis methods. The synthesis of $\mathrm{LaO_{0.5}F_{0.5}BiS_2}$ under pressure with a T_c of $\sim$ 10 K suggests the possibility that the transformation pressure between the low and high pressure phases can be reduced to zero pressure by using a different synthesis route.[10]

4.4 Summary

We have observed a striking enhancement of superconductivity accompanying the suppression of semiconducting behavior with pressure in the $Ln\mathrm{O_{0.5}F_{0.5}BiS_2}$ compounds (Ln = La, Ce) at critical pressures of $\sim$ 1.1 GPa and $\sim$ 2.0 GPa for Ln = La and Ce, respectively. There is markedly similar behavior in the electrical resistivity measurements under applied pressure for these two $\mathrm{BiS_2}$-based superconductors $\mathrm{LaO_{0.5}F_{0.5}BiS_2}$ and $\mathrm{CeO_{0.5}F_{0.5}BiS_2}$. Electrical resistivity measurements reveal that for both compounds, the suppression of their semiconducting behavior is hysteretic upon application of pressure. The semiconducting behavior of the electrical resistivity is consistent with two energy gaps that are suppressed with pressure in a similar way. The pressure dependence of the electrical resistivity exhibits hysteresis below a critical pressure where there is a change in slope of $\log(\rho)$ vs. P and where the maximum value of T_c is observed. Furthermore, for both compounds, we have discovered a continuous and reversible transient region between regions of low and high T_c, which is characterized by a broadening of the superconducting transition; however, the mechanism behind the broadening of the superconducting transitions between the lower and higher T_c regions is unclear. The broadening could be a simple consequence of the sensitive pressure-dependence of T_c in this region, which, when coupled with even a modest pressure gradient, could result in broader measured superconducting transitions. Sample inhomogeneity might also be responsible for the distribution of transition pressures seen in the broadening region, and the possibility of pressure-induced structural phase transitions is currently being investigated with x-ray diffraction measurements under pressure. Given the striking similarity in behavior for these two BiS_2-based superconductors, further electrical resistivity measurements under pressure on other compounds could point to characteristic behavior of BiS_2-based superconductors in general.

In experiments currently underway we have observed the same qualitative behavior for the $NdO_{0.5}F_{0.5}BiS_2$ and $PrO_{0.5}F_{0.5}BiS_2$ compounds as were observed in the the $LaO_{0.5}F_{0.5}BiS_2$ and $CeO_{0.5}F_{0.5}BiS_2$ compounds suggesting this is indeed a general phenomenon in the class of $LnO_{0.5}F_{0.5}BiS_2$ compounds. Our results on the $NdO_{0.5}F_{0.5}BiS_2$ compound may be compared to the recently reported study of $NdO_{0.5}F_{0.5}BiS_2$ specimens prepared in a solid state reaction by Selvan *et al.*[16] For the compounds with *Ln* = La, Ce and Pr, there is a dramatic decrease in the electrical resistivity with pressure that reflects a continuous suppression of semiconducting behavior. Although the temperature coefficient of the electrical resistivity, $d\rho/dT$, at the highest pressures is small for these *Ln* = La, Ce and Pr compounds, the coefficient nevertheless remains negative ($d\rho/dT < 0$), so that we cannot definitely conclude that the metallic state has been achieved. We have, however, been able to reach a metallic state for *Ln* = Nd, indicated by a positive temperature coefficient of resistivity ($d\rho/dT > 0$), consistent with a semiconductor-metal transition. Experiments to pressures in excess of 3 GPa are currently under way to see if definitive metallic states (i.e., $d\rho/dT > 0$) can be attained for the *Ln* = La, Ce, and Pr compounds.

Acknowledgements

Chapter 4, in full, is a reprint of the article, “Pressure-induced enhancement of superconductivity and suppression of semiconducting behavior in $Ln\text{O}_{0.5}\text{F}_{0.5}\text{BiS}_2$ (Ln = La, Ce) compounds,” by C. T. Wolowiec, D. Yazici, B. D White, K. Huang, and M. B. Maple, as it appears in *Phys. Rev. B* **88**, 064503 (2013). The dissertation author was the primary investigator and author of this paper.

Blbliography

[1] Y. Mizuguchi, H. Fujihisa, Y. Gotoh, K. Suzuki, H. Usui, K. Kuroki, S. Demura, Y. Takano, H. Izawa, and O. Miura, “Novel BiS_2-based layered superconductor $Bi_4O_4S_3$”, Phys. Rev. B **86**, 220510(R) (2012).

[2] S. K. Singh, A. Kumar, B. Gahtori, S. Kirtan, G. Sharma, S. Patnaik, and V. P. S. Awana, “Bulk superconductivity in Bismuth oxy-sulfide $Bi_4O_4S_3$”, J. Am. Chem. Soc. **134**, 16504 (2012).

[3] B. Li, Z. W. Xing, and G. Q. Huang, “Phonon spectra and superconductivity of BiS_2-based compounds $LaO_{1-x}F_xBiS_2$”, Europhys. Lett. **101**, 47002 (2013).

[4] R. Jha, A. Kumar, S. K. Singh, and V. P. S. Awana, “Synthesis and superconductivity of new BiS_2 based superconductor $PrO_{0.5}F_{0.5}BiS_2$”, J. Sup. and Novel Mag. **26**, 499 (2013).

[5] R. Jha, A. Kumar, S. K. Singh, and V. P. S. Awana, “Superconductivity above 5 K in $NdO_{0.5}F_{0.5}BiS_2$”, J. Appl. Phys. **113**, 056102 (2013).

[6] K. Deguchi, Y. Mizuguchi, S. Demura, H. Hara, T. Watanabe, S. J. Denholme, M. Fujioka, H. Okazaki, T. Ozaki, H. Takeya, T. Yamaguchi, and Y. T. O. Miura, “Evolution of superconductivity in $LaO_{1-x}F_xBiS_2$ prepared by high pressure technique”, Europhys. Lett. **101**, 17004 (2013).

[7] H. Kotegawa, Y. Tomita, H. Tou, H. Izawa, Y. Mizuguchi, O. Miura, S. Demura, K. Deguchi, and Y. Takano, “Pressure Study of BiS_2-Based Superconductors $Bi_4O_4S_3$ and La(O,F)BiS_2”, J. Phys. Soc. Jpn. **81**, 103702 (2012).

[8] V. P. S. Awana, A. Kumar, R. Jha, S. Kumar, A. Pal, Shruti, J. Saha, and S. Patnaik, “Appearance of superconductivity in new BiS_2 based layered $LaO_{0.5}F_{0.5}BiS_2$”, Solid State Communication **157**, 23 (2013).

[9] S. Demura, Y. Mizuguchi, K. Deguchi, H. Okazaki, H. Hara, T. Watanabe, S. J. Denholme, M. Fujioka, T. Ozaki, H. Fujihisa, Y. Gotoh, O. Miura, T. Yamaguchi, H. Takeya, and Y. Takano, “New member of BiS_2 - based superconductor $NdOBiS_2$”, J. Phys. Soc. Jpn. **82**, 033708 (2013).

[10] Y. Mizuguchi, S. Demura, K. Deguchi, Y. Takano, H. Fujihisa, Y. Gotoh, H. Izawa, and O. Miura, “Superconductivity in novel BiS_2-based layered superconductor $LaO_{1-x}F_xBiS_2$”, J. Phys. Soc. Jpn. **81**, 114725 (2012).

[11] J. Xing, S. Li, X. Ding, H. Yang, and H.-H. Wen, “Superconductivity Appears in the Vicinity of an Insulating-Like Behavior in $CeO_{1-x}F_xBiS_2$”, Phys. Rev. B **86**, 214518 (2012).

[12] D. Yazici, K. Huang, B. D. White, A. H. Chang, A. J. Friedman, and M. B. Maple, "Superconductivity of F-substituted $LnOBiS_2$ (Ln=La, Ce, Pr, Nd, Yb) compounds", Philos. Mag. **93**, 673 (2012).

[13] D. Yazici, K. Huang, B. D. White, I. Jeon, V. W. Burnett, A. J. Friedman, I. K. Lum, M. Nallaiyan, S. Spagna, and M. B. Maple., "Superconductivity induced by electron doping in the system $La_{1-x}M_xOBiS_2$ (M= Ti, Zr, Hf, and Th)", Phys. Rev. B **87**, 174512 (2013).

[14] T. F. Smith, C. W. Chu, and M. B. Maple, "Superconducting manometers for high pressure measurement at low temperature", Cryogenics **9**, 53 (1969).

[15] V. Taufour, S. L. Bud'ko, and P. C. Canfield, private communication, 2013.

[16] G. Kalai Selvan, M. Kanagaraj, S. Esakki Muthu, R. Jha, V. P. S. Awana, and S. Arumugam, "Hydrostatic pressure effect on T_c of new BiS_2 based $Bi_4O_4S_3$ and $NdO_{0.5}F_{0.5}BiS_2$ layered superconductors", Phys. Status Solidi RRL **7**, 510 (2013).

Chapter 5

Enhancement of superconductivity near the pressure-induced semiconductor to metal transition in layered superconductors $LnO_{0.5}F_{0.5}BiS_2$ (Ln = La, Ce, Pr, Nd)

5.1 Introduction

The recent discovery of the BiS_2-based superconductor $Bi_4O_4S_3$ by Mizuguchi *et al.* [1, 2] with a superconducting critical temperature T_c^{onset} of 8.6 K has generated much interest in a new family of BiS_2-based superconductors. The members of the class of novel BiS_2-based superconductors have layered crystal structures that consist of superconducting BiS_2 layers separated by blocking layers which act as charge reservoirs that dope the BiS_2 layers with charge carriers.[1] Experimental efforts on the BiS_2-based materials have focused on increasing the charge carrier concentration via chemical substitution within the blocking layer [3–12] as well as through a reduction of the unit cell volume via the application of an external pressure.[13–16]

Recent studies of the BiS_2-based compounds involving chemical substitution within the blocking layers have lead to the discovery of the related class of superconductors $\mathit{Ln}O_{0.5}F_{0.5}BiS_2$ (Ln = La, Ce, Pr, Nd, Yb).[4, 8–11, 15] The compound $LaO_{0.5}F_{0.5}BiS_2$, synthesized under high pressure, has been reported by Mizuguchi *et al.* to have a T_c of 10.6 K which exceeds that of $Bi_4O_4S_3$.[9] In addition, the compounds with Ln = Ce, Pr, Nd, and Yb exhibit T_c^{onset} values of $\sim$3.0 , 5.6 , 4.3 , and 5.3 K, respectively.[4, 8, 10, 11] More recent work demonstrates that chemical substitution of the tetravalent ions Th^{+4}, Hf^{+4}, Zr^{+4} and Ti^{+4} for trivalent La^{+3} in $LaOBiS_2$ increases the charge-carrier density and induces superconductivity.[12]

Measurements of the pressure dependence of the electrical resistivity ρ and the superconducting critical temperature T_c have also recently been reported for several of these new compounds.[13–16] In this paper, we report the temperature dependence of the electrical resistivity ρ from 3 to 300 K for the $\mathit{Ln}O_{0.5}F_{0.5}BiS_2$ (Ln = Pr, Nd) compounds under applied quasi-hydrostatic pressure up to $\sim$2.8 GPa. Both compounds exhibit the same qualitative evolution of T_c in which they undergo a pressure-induced transition at P_t from a low T_c superconducting phase to a high T_c superconducting phase. This transition region is characterized by a rapid increase of T_c in a narrow range of pressure $\sim$0.3 GPa. In the high T_c phase at $\sim$2.5 GPa, we observed a maximum T_c of 7.6 K for $PrO_{0.5}F_{0.5}BiS_2$ and 6.4 K for $NdO_{0.5}F_{0.5}BiS_2$. In the normal state of both materials, there is a significant suppression of semiconducting behavior with pressure which is continuous up to the pressure P_t. A rapid increase of the charge carrier density is inferred from both the suppression of the semiconducting behavior and the rapid increase of T_c in this region.[17]

The pressure dependence of ρ and the evolution of T_c reported herein for the

LnO$_{0.5}$F$_{0.5}$BiS$_2$ (Ln = Pr, Nd) compounds are qualitatively similar to the behavior we recently reported for the LnO$_{0.5}$F$_{0.5}$BiS$_2$ (Ln = La, Ce) compounds.[14] For the four BiS$_2$-based layered superconductors, LnO$_{0.5}$F$_{0.5}$BiS$_2$ (Ln = La, Ce, Pr, Nd), the transition pressure P_t and the size of the "jump" in T_c between the two superconducting phases both scale with the lanthanide element Ln; specifically, as the atomic number of Ln increases, P_t increases while the "jump" in T_c decreases.

5.2 Experimental section

Polycrystalline samples of LnO$_{1-x}$F$_x$BiS$_2$ (Ln = Pr, Nd) with $x = 0.5$ were prepared by solid-state reaction using powders of Pr$_2$O$_3$ (99.9%), PrF$_3$ (99.9%), Pr$_2$S$_3$ (99.9%), and Bi$_2$S$_3$ (99.9%) for PrO$_{1-x}$F$_x$BiS$_2$, and powders of Nd$_2$O$_3$ (99.9%), NdF$_3$ (99.9%), Nd$_2$S$_3$ (99.9%), and Bi$_2$S$_3$ (99.9%) for NdO$_{1-x}$F$_x$BiS$_2$. Bi$_2$S$_3$ precursor powder was prepared in an evacuated quartz tube by reacting Bi (99.99%) and S (99.9%) at 500°C for 10 hours. The Ln_2S$_3$ (Ln = Pr, Nd) precursor powders were prepared in an evacuated quartz tube by reacting chunks of Pr and Nd with S grains at 800°C for 10 hours. The starting materials with nominal composition LnO$_{0.5}$F$_{0.5}$BiS$_2$ (Ln = Pr, Nd) were weighed, thoroughly mixed, pressed into pellets, sealed in evacuated quartz tubes, and annealed at 800°C for 48 hours. The products were ground, mixed for homogenization, pressed into pellets, and annealed again in evacuated quartz tubes at 800°C for 48 hours. This last step was repeated again to promote phase homogeneity. X-ray powder diffraction measurements (not shown) were made using an X-ray diffractometer with a Cu K$_\alpha$ source to assess phase purity and to determine the lattice parameters of the LnO$_{0.5}$F$_{0.5}$BiS$_2$ (Ln = Pr, Nd) compounds. The main diffraction peaks for the two samples can be well indexed to a tetragonal structure with space group *P4/nmm* conforming to the CeOBiS$_2$ structure. The lattice parameters for PrO$_{0.5}$F$_{0.5}$BiS$_2$ were determined to be $a = b = 4.0192$ Å and $c = 13.4238$ Å, while for

$NdO_{0.5}F_{0.5}BiS_2$ the lattice parameters are $a = b = 4.0102$ Å and $c = 13.4468$ Å.[11]

Measurements of $\rho(T)$ under applied pressure were performed up to $\sim$2.8 GPa in a clamped piston cylinder pressure cell between $\sim$3 K and 300 K in a pumped ^{4}He dewar. A 1:1 by volume mixture of *n*-pentane and isoamyl alcohol was used to provide a quasi-hydrostatic pressure transmitting medium. Annealed Pt leads were affixed to gold-sputtered contact surfaces on each sample with silver epoxy in a standard four-wire configuration. The pressure dependence of T_c for high purity Sn (99.999%) was measured inductively and used as a manometer for the experiments. The pressure was determined by calibrating our T_c data for Sn against data used in [18]. The width of the superconducting transition of the Sn manometer was used as a measure of the error in pressure, which was found to be on the order $\Delta P \sim \pm$ 0.05 GPa.

5.3 Results

The temperature dependence of the electrical resistivity ρ for $T < 300$ K for $PrO_{0.5}F_{0.5}BiS_2$ and $NdO_{0.5}F_{0.5}BiS_2$ at various pressures up to 2.8 GPa are shown in Figure 5.1 (a) and (b), respectively. Both compounds exhibit semiconducting behavior at low pressure (indicated by a negative temperature coefficient of resistivity ($d\rho/dT < 0$)). The semiconducting behavior is strongly suppressed at lower pressures. As pressure is increased, the electrical resistivity ρ of $PrO_{0.5}F_{0.5}BiS_2$ becomes weakly temperature dependent above $\sim$1.5 GPa, but remains semiconducting ($d\rho/dT < 0$). In contrast, the $NdO_{0.5}F_{0.5}BiS_2$ sample becomes metallic at $\sim$2 GPa (indicated by a positive temperature coefficient of resistivity ($d\rho/dT > 0$) in Figure 5.1(b)).

Superconducting transitions for $PrO_{0.5}F_{0.5}BiS_2$ and $NdO_{0.5}F_{0.5}BiS_2$ are displayed in Figure 5.1(c) and (d), respectively. At lower pressures up to $\sim$1 GPa, the superconducting transitions in $PrO_{0.5}F_{0.5}BiS_2$ are grouped near 3.5 K. As pressure is increased, there is

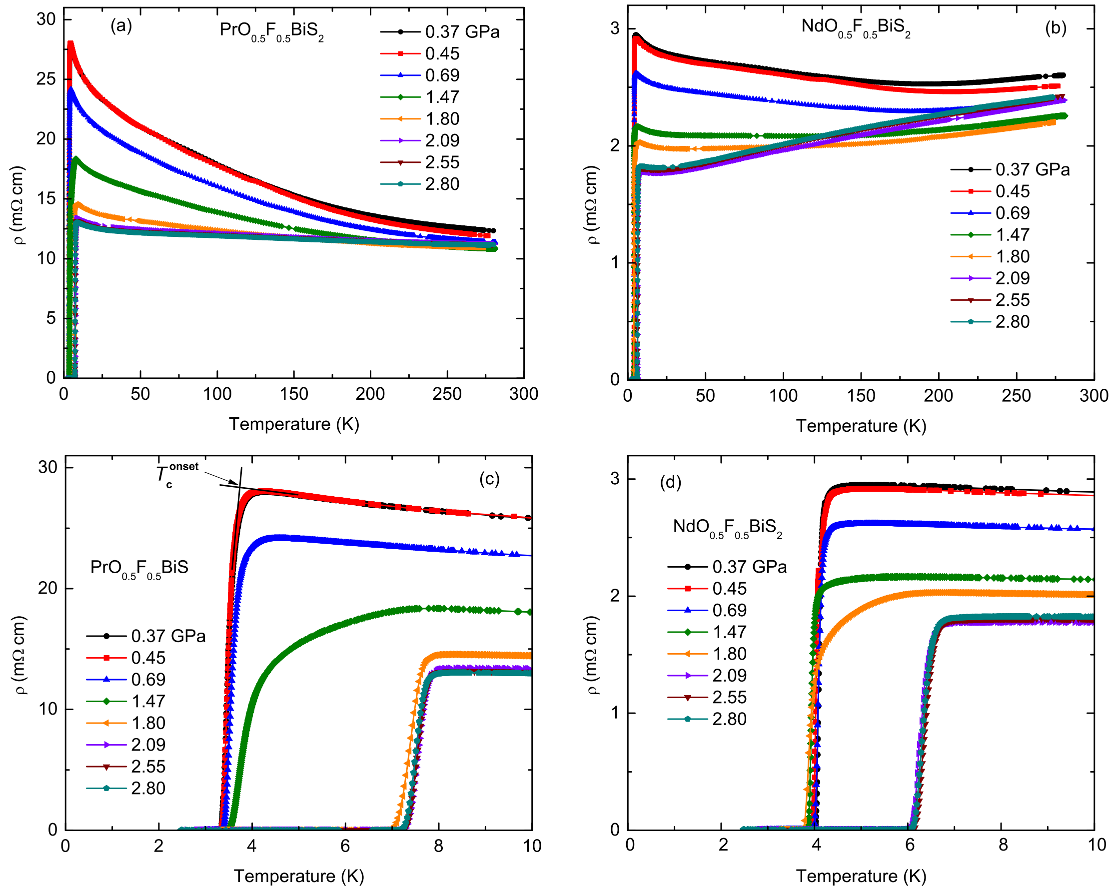

Figure 5.1: (a),(b) Temperature dependence of the electrical resistivity ρ at various pressures for (a) $PrO_{0.5}F_{0.5}BiS_2$ and (b) $NdO_{0.5}F_{0.5}BiS_2$. At lower pressures, both compounds exhibit semiconducting behavior which is suppressed with increasing pressure. $NdO_{0.5}F_{0.5}BiS_2$ becomes completely metallic at ∼2 GPa ($d\rho/dT > 0$). (c),(d) Resistive superconducting transition curves for (c) $PrO_{0.5}F_{0.5}BiS_2$ and (d) $NdO_{0.5}F_{0.5}BiS_2$ at various pressures. In $PrO_{0.5}F_{0.5}BiS_2$, T_c increases from 3.5 K to a maximum of 7.6 K while in $NdO_{0.5}F_{0.5}BiS_2$, T_c increases from 3.9 K to a maximum of 6.4 K.

a slight broadening of the width of the superconducting transition ΔT_c at ∼1.5 GPa which is immediately followed by a dramatic increase in T_c from ∼3.9 to 7.4 K in the narrow range ∼1.5 - 1.8 GPa. Above 1.8 GPa, T_c passes through a maximum of 7.6 K at ∼2.5 GPa and then gradually decreases with increasing pressure. We observed similar behavior in the $NdO_{0.5}F_{0.5}BiS_2$ compound. Sharp superconducting transitions near 4.0 K were observed at low pressures up to ∼1.5 GPa. The width ΔT_c of the superconducting transition then appears to broaden near ∼1.8 GPa. In the small range ∼1.8 - 2.1 GPa, there is a siz-

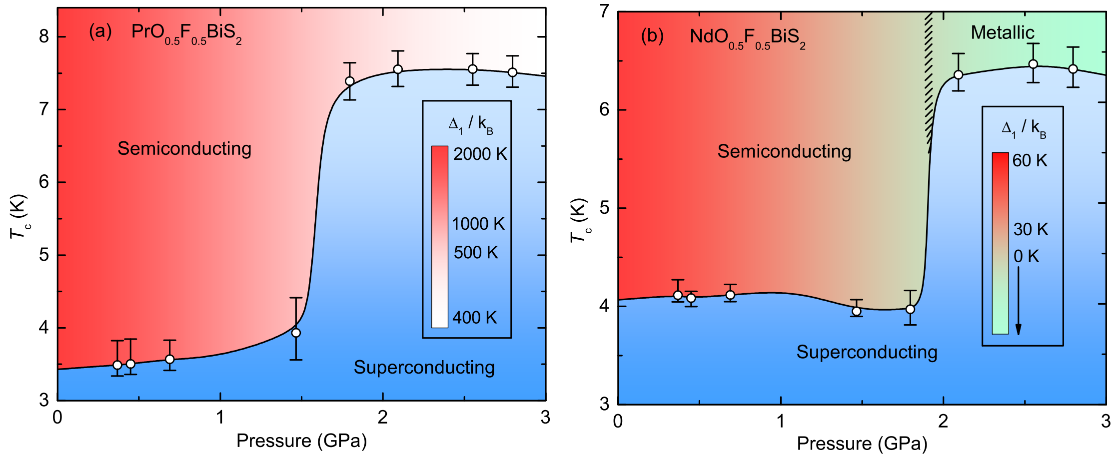

Figure 5.2: Temperature-pressure phase diagrams for (a) $PrO_{0.5}F_{0.5}BiS_2$ and (b) $NdO_{0.5}F_{0.5}BiS_2$ under pressure. Vertical bar lengths represent the transition width ΔT_c and vertical bar caps represent T_c^{onset} (upper) and T_0 (lower). The colour in the semiconducting region represents the energy gap Δ_1. Values for Δ_1 are indicated in the false colour legend. (b) The green region to the right of the crosshatching corresponds to the metallization of $NdO_{0.5}F_{0.5}BiS_2$ ($\Delta_1 = 0$). The solid black curves are guides to the eye.

able increase in T_c from ∼3.9 to 6.3 K. In $NdO_{0.5}F_{0.5}BiS_2$, T_c passes through a maximum of 6.4 K at ∼2.5 GPa and then gradually decreases at higher pressures up to ∼ 2.8 GPa, similar to the behavior observed for $PrO_{0.5}F_{0.5}BiS_2$.

The temperature-pressure phase diagrams for the two superconducting compounds $PrO_{0.5}F_{0.5}BiS_2$ and $NdO_{0.5}F_{0.5}BiS_2$ are displayed in Figure 5.2(a) and (b), respectively. In the superconducting state, both compounds exhibit a low T_c phase which is characterized by a gradual increase in T_c with pressure. In the $PrO_{0.5}F_{0.5}BiS_2$ sample, T_c increases monotonically from 3.5 to 3.9 K at pressures up to ∼1.5 GPa ($dT_c/dP = 0.40$ K GPa^{-1}). In the $NdO_{0.5}F_{0.5}BiS_2$ sample, there was a non-monotonic decrease in T_c from 4.1 to 3.9 K at pressures up to ∼1.8 GPa. As pressure is increased, both compounds exhibit a rapid increase in T_c within a narrow range ∼0.3 GPa. For the $PrO_{0.5}F_{0.5}BiS_2$ compound, T_c increases dramatically from 3.9 to 7.4 K as pressure is increased from ∼1.5 to 1.8 GPa ($dT_c/dP = 11.7$ K GPa^{-1}). In the $NdO_{0.5}F_{0.5}BiS_2$ compound, there is a significant jump in T_c from 3.9 to 6.3 K as pressure is increased from ∼1.8 to 2.1 GPa ($dT_c/dP =$

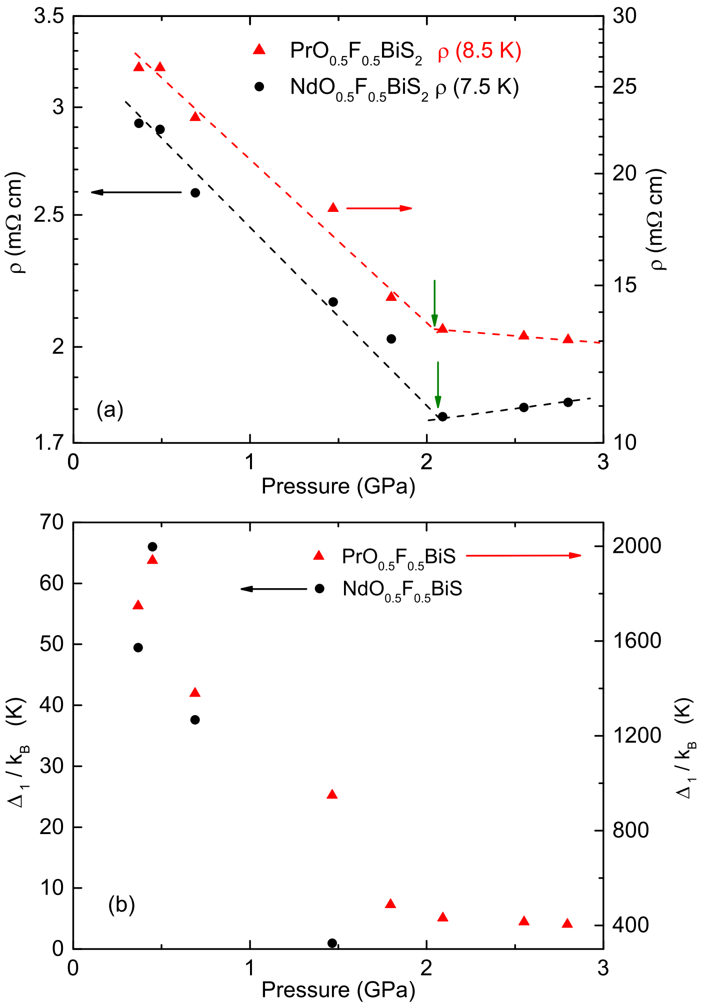

Figure 5.3: (a) Electrical resistivity ρ vs pressure in the normal state (plotted on a log scale). Values of ρ for PrO$_{0.5}$F$_{0.5}$BiS$_2$ and NdO$_{0.5}$F$_{0.5}$BiS$_2$ were taken at T = 8.5 and 7.5 K, respectively. Dotted lines reflect the slopes (suppression rates), and arrows point to changing slopes at ~2.1 GPa. The breaks in slope occur at the transition pressure P_t. (b) Energy gap Δ_1 (~100 - 200 K) vs pressure for both compounds. The rate of decrease in Δ_1 with pressure flattens at ~2 GPa in both compounds. Above ~1.9 GPa, Δ_1/k_B = 0 K in NdO$_{0.5}$F$_{0.5}$BiS$_2$.

8.0 K GPa^{-1}). Following the rapid increase in T_c, both compounds exhibit a high T_c superconducting phase, in which the evolution of T_c exhibits a domelike behavior; i.e., T_c gradually increases to its maximum value and then slowly decreases with pressure. In the PrO$_{0.5}$F$_{0.5}$BiS$_2$ compound, T_c increases to a maximum value of 7.6 K at 2.5 GPa and then steadily decreases with pressure, while in the NdO$_{0.5}$F$_{0.5}$BiS$_2$ compound, T_c increases to a maximum T_c of 6.4 K at $\sim$2.5 GPa and then decreases slowly with pressure.

In the normal state (above the $T_c(P)$ curves shown in Figure 5.2), the semiconducting behavior in both compounds is continuously suppressed with pressure as manifested by the decrease of the energy gap Δ_1 (defined below) with pressure, the values of which are indicated in the false colour legend of Figure 5.2(a) and (b) for $PrO_{0.5}F_{0.5}BiS_2$ and $NdO_{0.5}F_{0.5}BiS_2$, respectively. The $NdO_{0.5}F_{0.5}BiS_2$ sample exhibits a fully metallic state at $\sim$2 GPa (where Δ_1 vanishes), represented by the green region to the right of the crosshatching in Figure 5.2(b).

From the plot of $\log(\rho)$ vs. P displayed in Figure 5.3(a), there is a noticeable change in the magnitude of the suppression rate, $d\log(\rho)/dP$, for both the $PrO_{0.5}F_{0.5}BiS_2$ and $NdO_{0.5}F_{0.5}BiS_2$ compounds. The $\rho(P)$ data for $PrO_{0.5}F_{0.5}BiS_2$ and $NdO_{0.5}F_{0.5}BiS_2$ were taken in the normal state at 8.5 K and 7.5 K, respectively. These temperatures occur just above the onset of the superconducting transition at T_c^{onset}. In both compounds, there is a strong suppression of electrical resistivity up to $\sim$2.1 GPa, followed by a weaker suppression at higher pressures. The dotted lines in Figure 5.3(a) are guides to the eye for the rates of suppression. The change in the suppression rate near 2.1 GPa (emphasized by the vertical arrows in Figure 5.3(a)) is coincident with P_t.

The semiconducting behavior of the $\rho(T)$ data and its rapid suppression with pressure was noted by Kotegawa *et al.* in their study of the $LaO_{0.5}F_{0.5}BiS_2$ compound synthesized under high pressure.[13] They observed that $\rho(T)$ could be described over two distinct temperature regions by the relation $\rho(T) = \rho_0 e^{\Delta/2k_BT}$ where ρ_0 is a constant and Δ is an energy gap. In a recent paper, we applied this analysis to extract the high and low temperature energy gaps Δ_1 and Δ_2 for the $LnO_{0.5}F_{0.5}BiS_2$ (*Ln* = La, Ce) compounds.[14] We used the same analysis in the current study to determine the value of the high temperature energy gap Δ_1 for both compounds $LnO_{0.5}F_{0.5}BiS_2$ (*Ln* = Pr, Nd). The energy gap Δ_1 in $NdO_{0.5}F_{0.5}BiS_2$ was determined using the $\rho(T)$ data from the region 100 - 200 K for lower pressures 0.37 - 0.69 GPa and $\rho(T)$ data from the region 20 - 100 K for higher pressures 1.47 - 2.80 GPa. For $PrO_{0.5}F_{0.5}BiS_2$, the energy gap Δ_1 was extracted using $\rho(T)$ data in the region 200 - 280 K for all pressures up to 2.80 GPa.

The pressure dependence of the energy gap Δ_1 for both compounds is shown in Figure 5.3(b). The energy gap Δ_1 decreases rapidly with pressure up to $\sim$2 GPa. Above $\sim$2 GPa, Δ_1 exhibits relatively little pressure dependence. This is consistent with the transition to a weaker suppression rate shown in Figure 5.3(a) which also sets in at $\sim$2 GPa. In $NdO_{0.5}F_{0.5}BiS_2$, the energy gap $\Delta_1/k_B = 0$ K above 1.8 GPa. This is consistent with the semiconductor-metal transition near 2 GPa indicated by a positive temperature coefficient of electrical resistivity ($d\rho/dT > 0$) seen in the $\rho(T)$ data shown in Figure 5.3(b). The rapid decrease in the energy gap Δ_1 for $P < P_t$ in both the LnO$_{0.5}$F$_{0.5}$BiS$_2$ (Ln = Pr, Nd) compounds is similar to behavior observed previously in the LnO$_{0.5}$F$_{0.5}$BiS$_2$ (Ln = La, Ce) compounds.[13, 14]

5.4 Discussion

Both the temperature dependence of the electrical resistivity ρ and the evolution of T_c under applied pressure for the LnO$_{0.5}$F$_{0.5}$BiS$_2$ (Ln = Pr, Nd) samples reported in section 5.3 of this paper are markedly similar to the results we recently reported for the LnO$_{0.5}$F$_{0.5}$BiS$_2$ (Ln = La, Ce) compounds.[14] As shown in the phase diagrams displayed in Figure 5.4(a), each of the four compounds LnO$_{0.5}$F$_{0.5}$BiS$_2$ (Ln = La, Ce, Pr, Nd) exhibits an abrupt pressure-induced transition from a low T_c superconducting phase at lower pressure to a high T_c superconducting phase at higher pressure.

In the four compounds, the pressure-induced transition observed in the superconducting state is coincident with changes in the suppression of the electrical resistivity ρ in the normal state. The rate of suppression of semiconducting behavior (Figure 5.3(a))

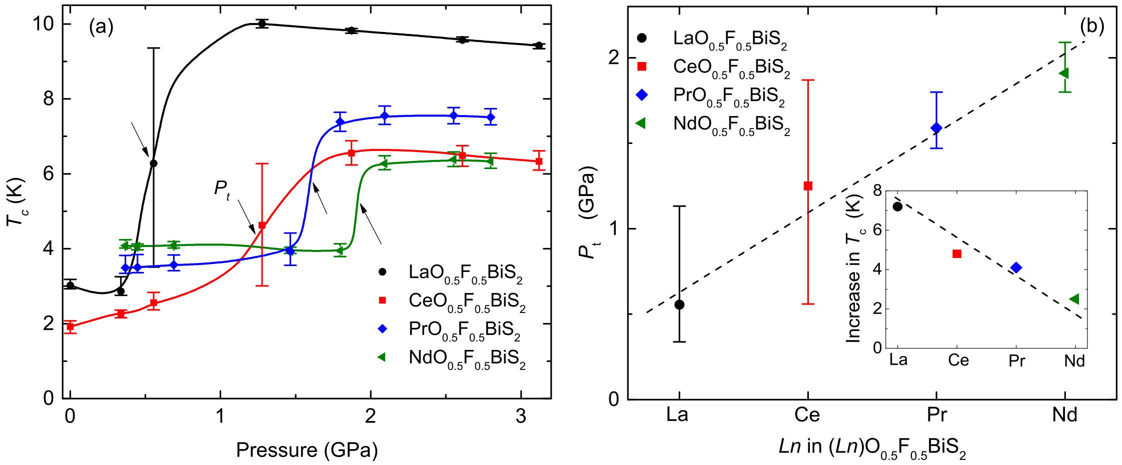

Figure 5.4: (a) T_c vs pressure plotted for the four compounds $LnO_{0.5}F_{0.5}BiS_2$ (Ln = La, Ce, Pr, Nd). The black arrows emphasize the transition pressure P_t which is defined in the text. (b) Transition pressure P_t plotted as a function of Ln in $LnO_{0.5}F_{0.5}BiS_2$. The inset displays the increase in T_c at P_t as a function of Ln. Dashed lines are guides to the eye.

and the rate of decrease in the energy gap Δ_1 (Figure 5.3(b)) both saturate at pressures that correlate with the transition pressure into the high T_c superconducting phase. In the specific case of the $NdO_{0.5}F_{0.5}BiS_2$ compound, a semiconductor-metal transition occurs at P_t. These changes in the normal state electrical resistivity indicate there may be significant increases in the charge carrier density during the rapid increase in T_c that occurs between the two superconducting phases.[17]

The transition pressures P_t, indicated by the black arrows in the temperature vs pressure phase diagrams of Figure 5.4(a), were defined as the pressure corresponding to the value of T_c at the midpoint between the values of T_c in the low and high T_c phases immediately preceding and following the transition. P_t is plotted as a function of lanthanide element (Ln = La, Ce, Pr, Nd) in $LnO_{0.5}F_{0.5}BiS_2$ in Figure 5.4(b). There is a clear linear relationship between the increasing atomic number of Ln and an increase in P_t. The magnitude of the "jump" in T_c also scales with the atomic number of the Ln element in $LnO_{0.5}F_{0.5}BiS_2$ as clearly shown in the inset of Figure 5.4(b). The pressure-induced increase in T_c decreases in magnitude as the atomic number of the lanthanide element in-

Table 5.1: T_c data for $LnO_{0.5}F_{0.5}BiS_2$ (Ln = La, Ce, Pr, Nd).

Ln	low T_c (K)	max. T_c (K)	increase in T_c (K)	P_t (GPa)
La	2.9	10.1	7.2	0.56
Ce	1.9	6.7	4.8	1.25
Pr	3.5	7.6	4.1	1.59
Nd	3.9	6.4	2.5	1.91

creases. The lengths of the vertical bars in Figure 5.4(b) represent the respective pressure windows over which the transitions from the low T_c phase to the high T_c phase occurred in each of the four compounds. The pressure range over which the transition occurs also decreases with increasing atomic number of *Ln* in $LnO_{0.5}F_{0.5}BiS_2$. Table 5.1 contains values of low T_c, maximum T_c, overall increase in T_c (max. T_c - low T_c), and transition pressure P_t, for each compound.

The evolution of T_c with pressure in the low T_c phase has recently been reported for the $LnO_{0.5}F_{0.5}BiS_2$ (Ln = Pr, Nd) compounds in two studies by Selvan *et al.*[15, 16] For $PrO_{0.5}F_{0.5}BiS_2$, they observed a gradual increase of T_c from 3.7 to 4.7 K with pressure up to $\sim$2.2 GPa.[16] For $NdO_{0.5}F_{0.5}BiS_2$, they found a gradual evolution of T_c with pressure from 4.6 to 5.0 K up to a pressure of $\sim$1.3 GPa and then down from 5.0 to 4.8 K upon further application of pressure up to $\sim$1.8 GPa.[15] In both reports, however, there was no evidence of a transition characterized by a rapid increase in T_c. It is possible that slight variations in the chemical composition of the samples in their studies compared to those studied by us may be responsible for differences in the material's response to applied pressure. Furthermore, the pressure transmitting media used in this study (see section 5.2) and the transmitting fluid used in their studies [15, 16] may have different properties with regard to pressure gradients that can affect the measured pressure at which a transition occurs.[19] It is also possible that the pressures reached in their studies were lower than the pressure required to induce the transitions that we observed in this report.

5.5 Concluding remarks

We have observed markedly similar behavior in the temperature dependence of the normal state electrical resistivity and evolution of the superconducting critical temperature T_c under applied pressure for the two BiS$_2$-based superconductors LnO$_{0.5}$F$_{0.5}$BiS$_2$ (Ln = Pr, Nd). The qualitative behavior observed for the two compounds in this study is strikingly similar to the results we recently reported for the two BiS$_2$-based superconductors LnO$_{0.5}$F$_{0.5}$BiS$_2$ (Ln = La, Ce).[14] In each of the four compounds LnO$_{0.5}$F$_{0.5}$BiS$_2$ (Ln = La, Ce, Pr, Nd), there is a sizable enhancement of T_c in the superconducting state accompanying the suppression of semiconducting behavior with pressure in the normal state. The suppression of the semiconducting behavior in the normal state saturates at a critical pressure P_t which corresponds to the pressure where there is a transition between a low T_c superconducting phase and a high T_c superconducting phase. The semiconducting behavior of the electrical resistivity in the normal state is consistent with an energy gap that is suppressed with pressure in a similar way. In the particular case of the NdO$_{0.5}$F$_{0.5}$BiS$_2$ compound, there is a pressure-induced semiconductor-metal transition at $P_t \approx 2$ GPa.

The coincidence of the saturation of the suppression of semiconducting behavior in the normal state electrical resistivity with the rapid increase in T_c indicates there may be significant increases in the charge carrier density in the vicinity of the pressure-induced transition. We found that the transition pressure P_t (see section 5.4) increases with increasing atomic number of the lanthanide element (Ln = La, Ce, Pr, Nd) in LnO$_{0.5}$F$_{0.5}$BiS$_2$. However, the size of the increase in T_c between the two superconducting phases decreases as lanthanide atomic number increases. The scaling of both the transition pressure P_t and the size of the "jump" in T_c with the atomic number of the lanthanide element suggests that the pressure-induced transition between the two superconducting phases may be a structural transition; however, at present, the precise mechanism driving the enhancement of T_c with pressure is unknown. X-ray diffraction experiments under pressure on the

$LaO_{0.5}F_{0.5}BiS_2$ compound are currently underway to help determine whether the pressure-induced enhancement of T_c and the suppression of semiconducting behavior are related to a structural transition.

Acknowledgements

Chapter 5, in full, is a reprint of the article, “Enhancement of superconductivity near the pressure-induced semiconductor-metal transition in the BiS_2-based superconductors $LnO_{0.5}F_{0.5}BiS_2$ (*Ln* = La, Ce, Pr, Nd) compounds,” by C. T. Wolowiec, B. D White, I. Jeon, D. Yazici, K. Huang, and M. B. Maple, as it appears in *J. Phys.: Condens. Matter* **25**, 422201 (2013). The dissertation author was the primary investigator and author of this paper.

Blbliography

[1] Y. Mizuguchi, H. Fujihisa, Y. Gotoh, K. Suzuki, H. Usui, K. Kuroki, S. Demura, Y. Takano, H. Izawa, and O. Miura, “Novel BiS_2-based layered superconductor $Bi_4O_4S_3$”, Phys. Rev. B **86**, 220510(R) (2012).

[2] S. K. Singh, A. Kumar, B. Gahtori, S. Kirtan, G. Sharma, S. Patnaik, and V. P. S. Awana, “Bulk superconductivity in bismuth oxy-sulfide $Bi_4O_4S_3$”, J. Am. Chem. Soc. **134**, 16504 (2012).

[3] B. Li, Z. W. Xing, and G. Q. Huang, “Phonon spectra and superconductivity of BiS_2-based compounds $LaO_{1-x}F_xBiS_2$”, Europhys. Lett. **101**, 47002 (2013).

[4] R. Jha, A. Kumar, S. K. Singh, and V. P. S. Awana, “Synthesis and superconductivity of new BiS_2 based superconductor $PrO_{0.5}F_{0.5}BiS_2$”, J. Sup. and Novel Mag. **26**, 499 (2013).

[5] R. Jha, A. Kumar, S. K. Singh, and V. P. S. Awana, “Superconductivity above 5 K in $NdO_{0.5}F_{0.5}BiS_2$”, J. Appl. Phys. **113**, 056102 (2013).

[6] K. Deguchi, Y. Mizuguchi, S. Demura, H. Hara, T. Watanabe, S. J. Denholme, M. Fujioka, H. Okazaki, T. Ozaki, H. Takeya, T. Yamaguchi, and Y. T. O. Miura, “Evolution of superconductivity in $LaO_{1-x}F_xBiS_2$ prepared by high pressure technique”, Europhys. Lett. **101**, 17004 (2013).

[7] V. P. S. Awana, A. Kumar, R. Jha, S. Kumar, A. Pal, Shruti, J. Saha, and S. Patnaik, “Appearance of superconductivity in new BiS_2 based layered $LaO_{0.5}F_{0.5}BiS_2$”, Solid State Communication **157**, 23 (2013).

[8] S. Demura, Y. Mizuguchi, K. Deguchi, H. Okazaki, H. Hara, T. Watanabe, S. J. Denholme, M. Fujioka, T. Ozaki, H. Fujihisa, Y. Gotoh, O. Miura, T. Yamaguchi, H. Takeya, and Y. Takano, “New member of BiS_2 - based superconductor $NdOBiS_2$”, J. Phys. Soc. Jpn. **82**, 033708 (2013).

[9] Y. Mizuguchi, S. Demura, K. Deguchi, Y. Takano, H. Fujihisa, Y. Gotoh, H. Izawa, and O. Miura, “Superconductivity in novel BiS_2-based layered superconductor $LaO_{1-x}F_xBiS_2$”, J. Phys. Soc. Jpn. **81**, 114725 (2012).

[10] J. Xing, S. Li, X. Ding, H. Yang, and H.-H. Wen, “Superconductivity Appears in the Vicinity of an Insulating-Like Behavior in $CeO_{1-x}F_xBiS_2$”, Phys. Rev. B **86**, 214518 (2012).

[11] D. Yazici, K. Huang, B. D. White, A. H. Chang, A. J. Friedman, and M. B. Maple, “Superconductivity of F-substituted LnOBiS2 (Ln=La, Ce, Pr, Nd, Yb) compounds”, Philos. Mag. **93**, 673 (2012).

[12]D. Yazici, K. Huang, B. D. White, I. Jeon, V. W. Burnett, A. J. Friedman, I. K. Lum, M. Nallaiyan, S. Spagna, and M. B. Maple., "Superconductivity induced by electron doping in the system $La_{1-x}M_xOBiS_2$ (M= Ti, Zr, Hf, and Th)", Phys. Rev. B **87**, 174512 (2013).

[13]H. Kotegawa, Y. Tomita, H. Tou, H. Izawa, Y. Mizuguchi, O. Miura, S. Demura, K. Deguchi, and Y. Takano, "Pressure study of BiS_2-based superconductors $Bi_4O_4S_3$ and La(O,F)BiS_2", J. Phys. Soc. Jpn. **81**, 103702 (2012).

[14]C. T. Wolowiec, D. Yazici, B. D. White, K. Huang, and M. B. Maple, "Pressure-induced enhancement of superconductivity and suppression of semiconducting behavior in $LnO_{0.5}F_{0.5}BiS_22$ (Ln = La, Ce) compounds", Phys. Rev. B **88**, 064503 (2013).

[15]G. Kalai Selvan, M. Kanagaraj, S. Esakki Muthu, R. Jha, V. P. S. Awana, and S. Arumugam, "Hydrostatic pressure effect on Tc of new BiS_2-based $Bi_4O_4S_3$ and $NdO_{0.5}F_{0.5}BiS_22$ layered superconductors", Phys. Status Solidi RRL **7**, 510 (2013).

[16]G. Kalai Selvan, M. Kanagaraj, R. Jha, V. P. S. Awana, and S. Arumugam, "Hydrostatic pressures dependence of superconductivity in $PrO_{0.5}F_{0.5}BiS_22$ superconductor", arXiv, 1307.4877 (2013).

[17]K. Igawa, H. Okada, H. Takahashi, S. Matsuishi, Y. Kamihara, M. Hirano, H. Hosono, K. Matsubayashi, and Y. Uwatoko, "Pressure-induced superconductivity in iron pnictide compound $SrFe_2As_2$", J. Phys. Soc. Jpn **78**, 025001 (2009).

[18]T. F. Smith, C. W. Chu, and M. B. Maple, "Superconducting manometers for high pressure measurement at low temperature", Cryogenics **9**, 53 (1969).

[19]N. P. Butch, J. R. Jeffries, D. A. Zocco, and M. B. Maple, "Hydrostaticity and hidden order: effects of experimental conditions on the temperature-pressure phase diagram of URu_2Si_2", High Pressure Research **29**, 335 (2009).

Chapter 6

Evolution of the critical pressure with increasing Fe substitution in the heavy fermion system $\mathrm{URu}_{2-x}\mathrm{Fe}_x\mathrm{Si}_2$

6.1 Introduction

Subsequent to the initial bulk property measurements that were performed on the heavy fermion superconductor $\mathrm{URu_2Si_2}$ in the mid 1980s, [1–3] researchers have yet to identify the order parameter (OP) associated with the so called "hidden order" (HO) phase observed at the transition temperature $T_0 \approx 17.5$ K. In the bulk, the key signatures of the second-order symmetry-breaking transition are (1) the anomalous upturn in the electrical resistivity, $\rho(T)$, that is reminiscent of a spin density wave (SDW) feature as observed, for instance, in the $\rho(T)$ data for elemental chromium near T_N = 311 K, [4] and (2) the large Bardeen-Cooper-Schrieffer (BCS)-like feature observed in the specific heat, $C(T)$, below T_0 = 17.5 K. From the specific heat anomaly, it was originally determined that a considerable amount of entropy, $\Delta S \approx 0.2R\ln(2)$, is released during the transition.[1, 2]

From the exponential temperature dependence of the specific heat and the reduction of the electronic contribution to the specific heat, [2] γT, a partial gapping scenario was proposed in which an energy gap, $\Delta \approx 130$ K, [1, 2] is attributed to a charge- or spin- density wave (CDW or SDW) that forms over $\sim$40 % of the Fermi surface with the remainder of the Fermi surface gapped by the superconductivity that occurs below $T_c \approx 1.5$ K. [2, 5] For the past three decades, the intense search for the OP in the HO phase has been accompanied by a large effort to explain the reduction in entropy that occurs during the transition to the HO phase as well as to determine the origin of the energy gap, Δ, near the transition temperature T_0. For a comprehensive survey of the experimental and theoretical research regarding the URu_2Si_2 compound, the reader is referred to Refs. [6] and[7].

Research at ambient pressure on the URu_2Si_2 compound reveals the existence of a second-order phase transition from a highly correlated paramagnetic (PM) phase above T_0 to the HO phase below T_0 that exhibits antiferromagnetic (AFM) order with a very small ordered moment of $\mu \sim (0.03 \pm 0.02)\mu_B$ per U atom that is aligned parallel to the c axis (in the simple tetragonal structure).[8, 9] It is interesting to note that this small value for the magnetic moment in the HO phase is two orders of magnitude smaller than values for the magnetic moment of $\mu \sim 1.6 - 2.9\mu_B$ per U atom observed in other magnetically ordered compounds from the UT_2Si_2 series where T is a d-electron transition element.[10, 11] This uniquely tiny magnetic moment observed in the HO phase in URu_2Si_2 is too small to account for the loss of entropy, ΔS, during the PM $\rightarrow$ HO transition. It is now believed that the small moment antiferromagnetic (AFM) order is not intrinsic to the HO phase but rather due to the existence of small pockets of the high pressure large-moment antiferromagnetic (LMAFM) phase that are stabilized by the extrinsic strain that can occur in preparing the sample for measurement.[12, 13] This small concentration of the LMAFM phase can produce an average moment of a few one-hundreths of a Bohr magneton (μ_B) per U atom. An extensive amount of pressure research on HO in URu_2Si_2 reveals, in

Table 6.1: Values of the critical pressure, P_c, and the pressure dependence ($\partial T_{HO}/\partial P$) in the HO phase along with the type of measurement for the URu_2Si_2 (x = 0) parent compound from previous reports.

Year	Reference	Critical Pressure (GPa)	$\partial T_{HO}/\partial P$ (K GPa^{-1})	Measurement type
1987	McElfresh[16]	$P_c > 1.3$	1.3 ± 0.1	$\rho(T)$
1999	Amitsuka[14]	P_c = 1.5	1.3 ± 0.1	elastic NS
2001	Matsuda[15]	P_c = 1.5	–	^{29}Si NMR
2003	Motoyama[17]	P_c = 1.1 - 1.5	1.0 ± 0.1	dilatometry
2004	Amato[18]	$P_c \sim 1.4$	–	μSR
2007	Jeffries[19]	$P_c = 1.5$	1.0 ± 0.1	$\rho(T)$
2008	Hassinger[20]	$P_c \sim 1.3$	1.1 ± 0.1	$\rho(T)$
2010	Butch[21]	$1.3 < P_c < 1.5$	1.3 ± 0.1	elastic NS, $\rho(T)$

addition to the second-order PM → HO transition, the existence of a first-order (symmetry-breaking) transition from the small moment HO phase to the LMAFM phase which has a larger magnetic moment of $\mu \sim 0.4\mu_B$ per U atom that is also aligned parallel to the c axis.[12–15] The first-order transition into the high pressure LMAFM phase is observed to occur at critical pressures that range from $P_c \approx 0.5$ GPa (as $T \to 0$) to $P_c \approx 1.5$ GPa (for $T = T_0$).

Table 7.1 provides a sampling of the variety of pressure research which includes measurements of electrical resistivity ($\rho(T)$),[16, 19–21] elastic neutron scattering (NS), [14, 21] thermal expansion (dilatometry),[17] muon spin resonance (μSR),[18] and nuclear magnetic resonance (^{29}Si NMR).[15] Together, the previous reports seem to indicate that $P_c \sim 1.5$ GPa is perhaps an upper bound value on the applied critical pressure that induces the first-order phase transition from the HO phase to the LMAFM phase.

Recent results from a number of ambient pressure experiments reveal that by tuning either polycrystalline [22] or single crystal [23, 24] samples of URu_2Si_2 with the isoelectronic substitution of Fe for Ru, it is possible to reach the same high pressure LMAFM phase in which the first-order HO → LMAFM phase transition at ambient pressure now occurs at some critical value of Fe concentration, $x_c^* \approx 0.1-0.2$. Furthermore, there is a remarkable correspondence observed in the evolution of T_0 with increasing Fe concentration for the range $x = 0$ to 0.3, when compared with the results of experiments in which $\mathrm{URu_2Si_2}$ is tuned with increasing applied pressure, P. [19] It has been suggested that the similarities between the T_0 vs. x and T_0 vs. P phase boundaries are a consequence of the effective reduction in the volume of the unit cell in which the substitution of the smaller Fe ions for Ru acts as a "chemical pressure", P_{ch}, that tracks well with the effects of applied pressure, P. [22–24]

In the research reported herein, we simultaneously tuned the $\mathrm{URu_2Si_2}$ compound with both Fe substitution, x, and applied external pressure, P, in an effort to further explore the suggestion, as made initially in Ref. [22], that there is an equivalence between the application of pressure, P, and chemical pressure, $P_{ch}(x)$, in inducing the HO → LMAFM phase transition. We found that we could bias the parent compound with "chemical pressure" toward the LMAFM phase by systematically introducing small levels of Fe into the $\mathrm{URu_2Si_2}$ compound, such that a smaller amount of applied external pressure is required to induce the transition to the high pressure LMAFM phase. Remarkably, we observed the consistent manner in which chemical pressure, $P_{ch}(x)$, and applied pressure, P, are "additive" such that $P_{ch}(x_c) + P_c \approxeq 1.5$ GPa at the first-order HO → LMAFM phase transition. (Herein, the symbol x_c is used to denote those "critical" concentrations of Fe that induce the HO → LMAFM phase transition in $\mathrm{URu_{2-x}Fe_xSi_2}$ compounds under pressure.) Hence, the predictability in which $P_{ch}(x_c)$ and applied critical pressure P_c combine to induce the HO → LMAFM phase transition can serve as a guide for future research on the $\mathrm{URu_{2-x}Fe_xSi_2}$ system under pressure. We also note that tuning the $\mathrm{URu_2Si_2}$ compound simultaneously with both x and P may serve as a workaround to some of the limitations encountered in pressure experiments so that larger regions of phase space might be studied. To this point, we were able to track the suppression of the critical pressure, P_c, and hence the tricritical point, ($T_0(P_c)$, P_c), in the T_0 vs. P phase diagram, as a function of Fe concentration, x, for the five $URu_{2-x}Fe_xSi_2$ (x = 0.025, 0.05, 0.10, 0.15, and 0.20) compounds.

The T_0 vs. P phase diagrams presented in this work are based on measurements of electrical resistivity, $\rho(T)$, under quasi-hydrostatic pressure up to P = 2.2 GPa for the five $URu_{2-x}Fe_xSi_2$ (x = 0.025, 0.05, 0.10, 0.15, and 0.20) compounds. Additionally, we employed a theoretical model of electrical resistivity [25] which we were able to fit to the $\rho(T)$ data for $T < T_0$ in order to extract values of the charge energy gap, Δ, as a function of pressure, P. The changes observed in the pressure dependence of the charge energy gap, $\Delta(P)$, are consistent with the values of the critical pressure P_c that were determined from the T_0 vs. P phase diagrams.

6.2 Experimental Details

Single crystals of $URu_{2-x}Fe_xSi_2$ were grown according to the Czochralski method in a Techno Search TCA 4-5 Tetra-Arc furnace under a zirconium-gettered argon atmosphere. The quality of the single crystal samples were determined by Laue X-ray diffraction patterns performed with a Photonic Science PXS11 X-ray measurement system together with X-ray powder diffraction (XRD) measurements performed with a Bruker D8 Discover X-ray diffractometer that uses Cu-$K\ \alpha$ radiation. The XRD patterns were fitted via the Rietveld refinement technique using the GSAS + EXPGUI software package.

Annealed Pt wire leads were affixed with silver epoxy to gold-sputtered contact surfaces on each sample in a standard four-wire configuration. The single crystal samples were cleaved along the basal plane of the tetragonal structure of the sample and the measurements of $\rho(T)$ were made with current running parallel to the a axis. The orientation of the single-crystal samples of $URu_{2-x}Fe_xSi_2$ were confirmed from Laue X-ray diffraction patterns.

Electrical resistivity $\rho(T)$ measurements were performed on single crystal samples of $URu_{2-x}Fe_xSi_2$ under applied pressure up to P = 2.2 GPa for Fe concentrations x = 0.025, 0.05, 0.10, 0.15, and 0.2. A 1:1 mixture by volume of *n*-pentane and isoamyl alcohol was used to provide a quasi-hydrostatic pressure transmitting medium and the pressure was locked in with the use of a beryllium copper clamped piston-cylinder pressure cell. The pressure dependence of the superconducting transition temperature, T_c, of high purity Sn was used as a manometer. The superconducting transition of the Sn manometer was measured inductively and the pressure dependence of T_c was calibrated against data from Ref. [26]. Measurements of $\rho(T)$ were performed upon warming from $\sim$ 1 to 300 K in a pumped ^{4}He dewar and the temperature was determined from the four-wire resistivity of a calibrated Cernox sensor which was thermally sunk to the beryllium copper pressure clamp. For the $URu_{2-x}Fe_xSi_2$ compounds with x = 0.05 and 0.15, a second set of $\rho(T)$ measurements were performed in reverse by releasing pressure from the pressurized cell from 2.2 GPa down to atmospheric pressure.

6.3 Results and Discussion

Enhancement of T_0 with Fe substitution

The effect of Fe substitution on the PM → HO/LMAFM transition temperature, T_0, in the $URu_{2-x}Fe_xSi_2$ system for x = 0.025, 0.05, 0.10, 0.15, and 0.20 was determined from measurements of $\rho(T)$ at ambient pressure. The temperature dependence of the electrical resistivity, $\rho(T)$, in the vicinity of T_0 for the five compounds $URu_{2-x}Fe_xSi_2$ (x = 0.025, 0.05, 0.10, 0.15, and 0.20) is shown in the inset of Fig. 6.1. The PM → HO/LMAFM transition temperature, T_0, is defined in this report as the temperature at which there is a minimum in $\rho(T)$ (which occurs just prior to cooling through the small upturn in $\rho(T)$)

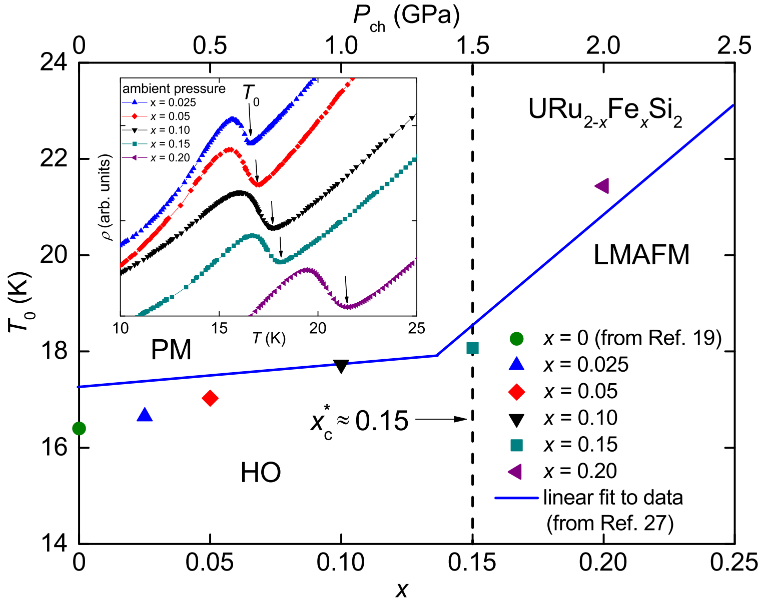

Figure 6.1: (Color online) The T_0 vs. x phase diagram at ambient pressure constructed from measurements of $\rho(T)$ for the URu$_{2-x}$Fe$_x$Si$_2$ system. The two sloped solid-blue lines which intersect near the critical concentration at $x_c^* = 0.15$ represent the $T_0(P)$ boundary line between the PM phase and the HO/ LMAFM phase and are linear fits to the T_0 vs. x data taken from Ref. [27] (see text). The six symbols in color superimposed on the T_0 vs. x phase diagram are the ambient pressure values of T_0 (see inset) determined from measurements of $\rho(T)$ under pressure for the single crystal samples of URu$_{2-x}$Fe$_x$Si$_2$ with x = 0, 0.025, 0.05, 0.10, 0.15, and 0.20. (The green data point shown at $x = 0$ was taken from a previous study of the URu$_2$Si$_2$ parent compound under pressure. [19]) The values of x in the lower x-axis have been converted to values of "chemical pressure" $P_{ch}(x)$ which appear in the upper x-axis. Inset: Measurements of electrical resistivity, $\rho(T)$, at ambient pressure in the vicinity of the HO/LMAFM transition for the URu$_{2-x}$Fe$_x$Si$_2$ (x = 0.025, 0.05, 0.10, 0.15, and 0.20) compounds. The curves have been shifted vertically for clarity in illustrating the evolution of T_0 with increasing x. The HO/LMAFM transition temperature, T_0, is defined as the temperature at which there is a minimum in $\rho(T)$ as indicated by the black arrows.

as indicated by the black arrows shown in the inset of Fig. 6.1. (In this report, we denote the PM → HO transition temperature as T_{HO}, the PM → LMAFM transition temperature as T_N, and traditionally reserve the use of T_0 to refer to T_{HO} and T_N, collectively.) The enhancement of T_0 with increasing Fe concentration is apparent from the shift of the minimum in $\rho(T)$ to higher temperatures such that for x = 0.025, 0.05, 0.10, 0.15, and 0.20, the values of T_0 are 16.6, 17.0, 17.7, 18.1, and 21.4 K, respectively. The values of T_0 at ambient pressure for the compounds $URu_{2-x}Fe_xSi_2$ (x = 0, 0.025, 0.05, 0.10, 0.15, and 0.20) are represented by the six symbols in color that are superimposed on the T_0 vs. x phase diagram as displayed in Fig. 6.1. (The single data point in green at T = 16.5 K, which corresponds to the URu_2Si_2 (x = 0) compound, was taken from Ref. [19].)

From the T_0 vs. x phase diagram, the evolution of T_0 is shown to increase with Fe concentration, x, at a constant rate up until $x \approx 0.15$ at which point the rate of increase in T_0 with x abruptly increases. The two solid-blue lines, which meet near the critical concentration at $x_c^* = 0.15$, represent the $T_0(x)$ boundary line between the PM phase and the HO/ LMAFM phase and are linear fits to the T_0 vs. x data taken from Ref. [27]. The observed "kink" in the $T_0(x)$ data near $x_c^* = 0.15$ marks the point at which the compound undergoes a first-order phase transition from the HO phase to the LMAFM phase at ambient pressure. The critical value of Fe concentration, $x_c^* = 0.15$, was determined in this report to be the smallest concentration of Fe in the $URu_{2-x}Fe_xSi_2$ system at ambient pressure for which there is a (nearly) homogenous manifestation of the LMAFM phase throughout the sample. Here, we use the symbol x_c^* to denote the ambient pressure critical concentration of Fe to distinguish it from the symbol x_c, which will be reserved for those "critical" concentrations of Fe that induce the HO $\rightarrow$ LMAFM phase transition in $URu_{2-x}Fe_xSi_2$ compounds under pressure. Our determination of $x_c^* = 0.15$ is directly based on measurements of $\rho(T)$ for the $URu_{2-x}Fe_xSi_2$ (x = 0.025, 0.05, 0.10, 0.15, and 0.20) system under pressure and will be revisited later in our discussion regarding the effect of pressure on the HO $\rightarrow$ LMAFM phase transition for the $URu_{2-x}Fe_xSi_2$ series with x = 0.025, 0.05, 0.10, 0.15, and 0.20.

For now, we note that bulk property measurements of electrical resistivity (and also specific heat) performed on the URu_2Si_2 (x = 0) parent compound under applied pressure, P, or on the Fe-substituted compounds $URu_{2-x}Fe_xSi_2$ that are tuned with x, do not easily distinguish between the HO and LMAFM phases. The value of the critical concentration, $x_c^* = 0.15$, reported herein as the location of the "kink" in the T_0 vs. x phase diagram that marks the first-order phase transition from the HO phase to the LMAFM phase is consistent with values reported for the critical concentration that were determined from other types of measurements. Magnetic neutron diffraction experiments performed on the $URu_{2-x}Fe_xSi_2$ system for $x \leq 0.7$ reveal an abrupt increase in the uranium magnetic moment at $x = 0.1$.[23] A notable "kink" in the T_0 vs. x phase diagram at $x \approx 0.15$ was determined from both the magnetic neutron diffraction experiments and also measurements of specific heat. [23] Optical conductivity experiments performed on the $URu_{2-x}Fe_xSi_2$ system for x = 0, 0.05, 0.10 and 0.3 reveal that at $x = 0.10$ and below $T_0 = 18.5$ K, the compound may exist as a mixture of the HO and LMAFM phases suggesting that a full manifestation of the LMAFM phase occurs for some level of Fe concentration $x > 0.10$. [24]

The reduction in the unit cell volume associated with the substitution of smaller isoelectronic Fe ions for Ru ions in URu_2Si_2 can be interpreted as the result of "chemical pressure", P_{ch}, which can be determined from a conversion of x to $P_{ch}(x)$. [22] The chemical pressure, $P_{ch}(x)$, was determined from a calculation using the isothermal compressibility, κ_T, which, in general, relates the reduction in the volume, V, to the pressure, P, that is applied to a material. In the present context, the "chemical pressure", $P_{ch}(x)$, is determined from the linear decrease in the unit cell volume, V, that occurs with increasing levels of Fe concentration, x. The Fe concentration, x, that appears in the lower x-axis of Fig. 6.1 has been converted to $P_{ch}(x)$, which is displayed in the upper x-axis of the same figure. The conversion of x to $P_{ch}(x)$ is discussed in more detail below and will facilitate the discussion regarding the evolution of T_0 in the compounds under applied pressure. For now, we note that the value of the slope in the HO phase (for $x \leq 0.15$) is $\partial T_{HO}/\partial P_{ch} = 1.1$ K GPa^{-1}. This slope was determined from a linear fit to the $T_0(x)$ data that is represented

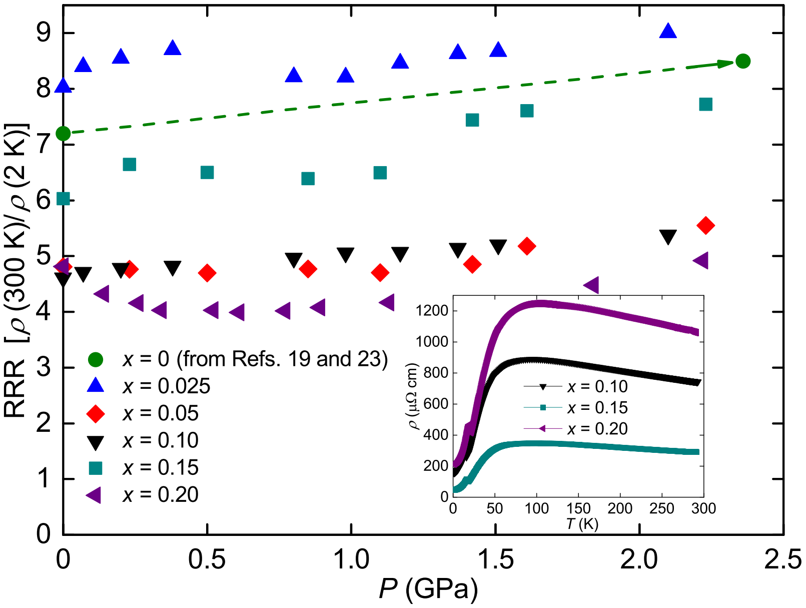

Figure 6.2: A plot of the residual resistivity ratio (RRR = ρ(300 K)/ρ(2 K)) as a function of pressure, P, for single crystal samples of $\mathrm{URu}_{2-x}\mathrm{Fe}_x\mathrm{Si}_2$ at x = 0, 0.025, 0.05, 0.10, 0.15, and 0.20. The two green data points for the x = 0 sample at P = 0 and 2.4 GPa connected by the dashed green arrow are taken from Refs. [19, 28]. Inset: A plot of the "unshifted" ρ vs. T curves at ambient pressure for the $\mathrm{URu}_{2-x}\mathrm{Fe}_x\mathrm{Si}_2$ (x = 0.10, 0.15, and 0.20) compounds, which displays the drop in the nominal electrical resistivity for the x = 0.15 compound relative to the neighboring concentrations of x = 0.10 and 0.20.

by the symbols in color at the Fe concentrations of x = 0 (green circle), x = 0.025 (blue diamond), x = 0.05 (red diamond), x = 0.10 (black triangle) and x = 0.15 (cyan square).

In this study, we are primarily concerned with the results obtained from the measurements of $\rho(T)$ performed under pressure for the five compounds $\mathrm{URu}_{2-x}\mathrm{Fe}_x\mathrm{Si}_2$ with x = 0.025, 0.05, 0.1, 0.15, and 0.2. However, it should be mentioned that in a related study of the $\mathrm{URu}_{2-x}\mathrm{Fe}_x\mathrm{Si}_2$ system as reported in Ref. [27], bulk property measurements, which included measurements of $\rho(T)$ of single crystals of $\mathrm{URu}_{2-x}\mathrm{Fe}_x\mathrm{Si}_2$ for $x \leq 0.7$, yielded a critical concentration of $x_c^* \approx 0.10$ at the HO → LMAFM transition and a "kink" in the T_0 vs. x phase diagram very similar to the T_0 vs. x phase diagram displayed in Fig. 6.1. However, in that study, the x dependence of the transition temperature T_{HO} (represented by the solid blue line in the HO phase as shown in Fig. 6.1) for small increases in the Fe concentration up to $x \approx 0.10$ is somewhat smaller than the positive slope reported herein for the $T_0(x)$ data which are represented by the symbols in color at the Fe concentrations of $x = 0$ (green circle), $x = 0.025$ (blue diamond), $x = 0.05$ (red diamond), $x = 0.10$ (black triangle) and $x = 0.15$ (cyan square). The discrepancy in the x dependence of T_{HO} at low concentrations of Fe between these two studies is largely due to the difference between the initial values of T_{HO} = 16.5 K and 17.3 K reported for the parent compound URu_2Si_2 (x = 0). While the value of T_{HO} = 17.3 K for the (x = 0) single crystal was obtained directly from measurements of $\rho(T)$ in Ref. [27], the value of T_{HO} = 16.5 K for the (x = 0) single crystal was determined from measurements of $\rho(T)$ as reported in Ref. [19].

Since we did not perform measurements of $\rho(T)$ on the parent compound URu_2Si_2 ($x = 0$) under pressure, the value of T_{HO} = 16.5 K from Ref. [19] was included in the present study in order to provide a reference for the $\rho(T,P)$ measurements on the Fe-substituted single crystals of $URu_{2-x}Fe_xSi_2$ with x = 0.025, 0.05, 0.10, 0.15, and 0.20. The details regarding both the synthesis of the single crystal of URu_2Si_2 (x = 0) in Ref. [19] as well as the experimental conditions for the measurements of $\rho(T)$ of the URu_2Si_2 (x = 0) sample under pressure as reported in Ref. [19] are nearly identical to the method of synthesis and experiments reported herein for the measurements of $\rho(T)$ of the Fe-substituted $URu_{2-x}Fe_xSi_2$ single crystal samples under pressure.

However, the fact that the transition temperature of T_{HO} = 16.5 K for the URu_2Si_2 parent compound at ambient pressure from Ref. [19] is low compared to T_{HO} values reported in other works as shown in Table 6.2 deserves some comment. The various values for T_{HO} listed in Table 6.2 are based on measurements of $\rho(T)$ for samples of the URu_2Si_2 parent compound at ambient pressure. The value of T_{HO} may be defined differently from one report to another; for example, in Refs. [19, 21], T_{HO} is defined to be at the minimum of the anomaly in the $\rho(T)$ curve (as we have defined it in this manuscript); in Refs. [16, 27], T_{HO} is defined to be at the “inflection point” of the anomaly in the $\rho(T)$ curve, or equivalently, at the minimum in the temperature derivative, $d\rho/dT$, of the $\rho(T)$ curve; in Ref. [22], T_{HO} is defined to be at the maximum in the anomaly in the $\rho(T)$ curve.

The low value of T_{HO} = 16.5 K from Ref. [19] as compared to the other values of T_{HO} = 17.8 K,[16] 17.5 K,[21] 18.0 K,[22] and 17.7 K,[27] (values which are determined from the minimum in the $\rho(T)$ curve), is likely due to issues related to sample quality as well as to extrinsic experimental issues related to differences in the thermometry that can occur during the measurement of $\rho(T)$. Drawing from the conclusions reached in Ref. [29] regarding those issues related to the quality of single crystal samples of URu_2Si_2, it appears that "small" discrepancies in the value of T_{HO} on the order of $\sim$ 0.5 K may result from differences in the residual resistivity ratio (RRR = ρ(300 K)/ρ(2 K)) that can occur from one sample to another. While high quality samples with larger values of RRR $\sim$ 100 tend to yield values of $T_{HO} \sim$ 17.8 K (defined at the minimum in the $\rho(T)$ curve), samples with smaller values of RRR $\sim$ 10 tend to yield values of $T_{HO} \sim$ 17.3 K. [29] Values of RRR that are listed in Table 6.2 indicate that the lowest value of RRR = 7.2 corresponds to the lowest value of the T_{HO} = 16.5 K, [19] while the largest value of RRR = 100 corresponds to the highest value of the T_{HO} = 18.0 K. [22]

The RRR values as a function of pressure, P, are displayed in Fig. 6.2 for both the single crystal samples of the Fe-substituted $URu_{2-x}Fe_xSi_2$ compounds with x = 0.025, 0.05, 0.10, 0.15, and 0.20 reported herein as well as the single crystal sample of URu_2Si_2 (x = 0) from Ref. [19].[19, 28] For each compound, there is a slight overall increase in the RRR value with an increase in pressure, P: for the $x = 0$ compound, there is an increase in the RRR value from 7.2 at 0 GPa to 8.5 at 2.4 GPa; for the $x = 0.025$ compound, there is an increase in the RRR value from 8.0 at 0 GPa to 9.0 at 2.1 GPa; for the $x = 0.05$ compound, there is an increase in the RRR value from 4.8 at 0 GPa to 5.5 at 2.2 GPa; for the $x = 0.10$ compound, there is an increase in the RRR vlaue from 4.6 at 0 GPa to 5.4 at 2.1 GPa; for the $x = 0.15$ compound, there is an increase in the RRR value from 6.0 at

0 GPa to 7.7 at 2.2 GPa; and for the $x = 0.20$ compound, there is an increase in the RRR value from 4.8 at 0 GPa to 4.9 at 2.2 GPa. We briefly note that there is a large amount of anisotropy observed in the room temperature electrical resistivity for single crystals of the URu_2Si_2 (x = 0) parent compound such that ρ(300 K) is roughly two times larger for a measurement of $\rho(T)$ parallel to the a-axis (or basal plane) when compared to a measurement with the current parallel to the c-axis.[30] Hence, the RRR value is sensitive to the orientation of the crystal during the measurement of $\rho(T)$. The RRR values as a function of pressure that are reported in Ref. [28] (which are based on the measurements of $\rho(T)$ for the URu_2Si_2 (x = 0) sample from Ref. [19]) were determined from measurements of $\rho(T)$ with the current parallel to the a-axis. The quality and orientation of the URu_2Si_2 (x = 0) sample from Ref. [19] were determined from Laue X-ray diffraction patterns.

As displayed in Fig. 6.2, there is also an overall reduction in the RRR value with increasing Fe concentration from x = 0.025 to 0.20. However, there is a jump in the RRR value at x = 0.15 which is due to the drop in the overall nominal value of the electrical resistivity, $\rho(T)$, for the sample with x = 0.15 relative to samples with neighboring concentrations of x = 0.10 and 0.20 as dispayed in the inset of Fig. 6.2. Sudden shifts in the nominal values of the electrical resistivity, $\rho(T)$, may occur during measurements of $\rho(T)$ in a hydrostatic piston-cylinder cell that can affect the electrical contacts between the platinum wire leads that are affixed with silver epoxy to the gold-sputtered samples. The unintended and not entirely understood effects on sample contacts in a four-wire electrical resistivity configuration that result from repeated thermal cycling between T = 300 K and 1 K while under applied pressure in a quasi-hydrostatic pressure medium (of isoamyl-alcohol and n-pentane) that freezes at $T \approx 100$ K may cause shifts of the nominal value of $\rho(T)$ from one measurement to the next.

Although the RRR = 7.2 and T_{HO} = 16.5 K values for the single crystal sample of URu_2Si_2 from Ref. [19] are low, it is important to note that both the critical pressure, P_c

Table 6.2: Values of the PM→HO phase transition temperature (T_{HO}) and the residual resistivtiy ratio (RRR) at ambient pressure along with the pressure dependence ($\partial T_{HO}/\partial P$) in the HO phase (if applicable), for samples of the URu_2Si_2 (x = 0) parent compound as reported in various works.

Year	Reference	RRR	Crystal	T_{HO} (K)	$\partial T_{HO}/\partial P$ (K GPa^{-1})
1987	McElfresh[16]	37.5	polycrystal	$17.4^{\dagger}$ (17.8^{*})	1.3 ± 0.1
2007	Jeffries[19]	7.2	single crystal	16.5^{*}	1.0 ± 0.1
2010	Butch[21]	22.5	single crystal	17.5^{*}	1.3 ± 0.1
2011	Kanchanavatee[22]	100	polycrystal	$17.5^{\ddagger}$ (18.0^{*})	–
2015	Ran[27]	11.9	single crystal	$17.3^{\dagger}$ (17.7^{*})	–

* T_{HO} defined at minimum in $\rho(T)$
† T_{HO} defined at inflection point in $\rho(T)$ or at minimum in $d\rho/dT$
‡ T_{HO} defined at maximum in $\rho(T)$

= 1.5 GPa, and the pressure dependence in the HO phase, $\partial T_{HO}/\partial P$ = 1.0 K GPa^{-1}, as determined from measurements of $\rho(T)$ for the URu_2Si_2 (x = 0) sample under pressure in Ref. [19] are consistent with other reports[14–18, 20, 21] (as shown in Table 7.1). The importance of this point will be addressed below when discussing the additive behavior of chemical pressure, P_{ch}, and applied critical pressure, P_c, such that $P_{ch}(x_c) + P_c \approx 1.5$ GPa for the $URu_{2-x}Fe_xSi_2$ system.

Enhancement of T_0 with pressure

Measurements of electrical resistivity $\rho(T)$ were performed under pressure for each of the compounds $URu_{2-x}Fe_xSi_2$ (x = 0.025, 0.05, 0.10, 0.15, and 0.20). The temperature dependence of $\rho(T)$ at various pressures up to $P \sim 2.2$ GPa in the region near T_0 for the $URu_{2-x}Fe_xSi_2$ (x = 0.025 and 0.20) compounds is shown in Fig. 6.3 (a) and (b), respectively. In the interest of space and to avoid redundancy, data for only two (x = 0.025 and 0.20) of the five (x = 0.025, 0.05, 0.10, 0.15, and 0.20) compounds investigated in this report are shown in Fig. 6.3. The compound with x = 0.025, which has the smallest Fe con-

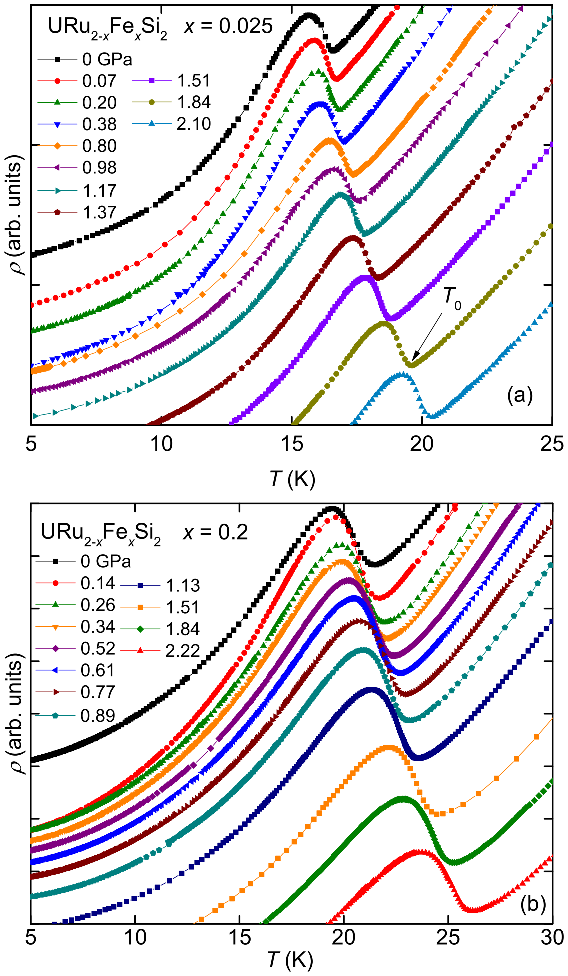

Figure 6.3: Temperature dependence of electrical resistivity $\rho(T)$ near the transition temperature T_0 at various pressures for $URu_{2-x}Fe_xSi_2$ (a) x=0.025 and (b) x=0.2. The $\rho(T)$ curves have been shifted vertically for clarity in illustrating the evolution of the resistivity feature near T_0. (Electrical resistivity curves for the other Fe concentrations, x = 0.05, 0.10, 0.15, are not shown but exhibit similar behavior). The transition temperature T_0 is defined as the temperature at which there is a minimum in $\rho(T)$ as indicated by the black arrow in the upper panel.

centration studied, is an example of a $URu_{2-x}Fe_xSi_2$ compound in the HO phase (for $T \leq T_0$) at ambient pressure that undergoes a first-order phase transition to the LMAFM phase as pressure is increased; the compound with $x = 0.20$, which is the largest Fe concentration in this study, represents an example of a $URu_{2-x}Fe_xSi_2$ compound that is already in the LMAFM phase (for $T \leq T_0$) at ambient pressure and remains in that phase as pressure is increased up to the maximum pressure reached in this experiment at $P \sim 2.2$ GPa.

The curves for $\rho(T)$ in both Fig. 6.3 (a) and (b) have been shifted vertically in order to better illustrate the behavior of the HO/LMAFM transition temperature T_0 as pressure is increased. The enhancement of T_0 can be seen in the shift of the feature in $\rho(T)$ to higher values of temperature as pressure is increased. Electrical resistivity (ρ vs. T) curves for the compounds with Fe concentrations of x = 0.05, 0.10, and 0.15 are not shown but exhibit similar behavior under applied pressure. Measurements of $\rho(T)$ under applied pressure for the two $URu_{2-x}Fe_xSi_2$ (x = 0.05, 0.15) compounds were also performed upon decreasing the pressure in the cell. The pressure was released by unloading the cell stepwise from $\sim$2.1 GPa to 0 GPa so that additional measurements of $\rho(T)$ could be performed for the purpose of confirming the reversibility of certain portions of the T_0 vs. P phase boundary. We briefly comment here that the results obtained for the evolution of T_0 with increasing pressure were completely reversible upon the release of pressure which can be seen in the $T_0(P)$ data (open symbols) for the $x = 0$, 0.05, and 0.15 compounds in the T_0 vs. P phase boundary displayed in Fig. 6.4.

The suppression of the critical pressure P_c with increasing Fe substitution

A composite plot of the T_0 vs. P phase boundaries for various values of x is displayed in Fig. 6.4. The T_0 vs. P phase boundaries were constructed from features in the $\rho(T)$ curves for the $URu_{2-x}Fe_xSi_2$ (x = 0, 0.025, 0.05, 0.10, 0.15, and 0.20) compounds under pressure, as illustrated in Fig. 6.3. (The green data points corresponding to the URu_2Si_2 (x = 0) compound were taken from a previous study of URu_2Si_2 under pressure by Jeffries *et al.* in Ref. [19].) The most striking aspect of the T_0 vs. P phase boundaries is the “shift” of the “kink” in the $T_0(P)$ data to lower values of pressure, P, in those $URu_{2-x}Fe_xSi_2$ compounds with higher concentrations of Fe, x. The “kink” in the $T_0(P)$

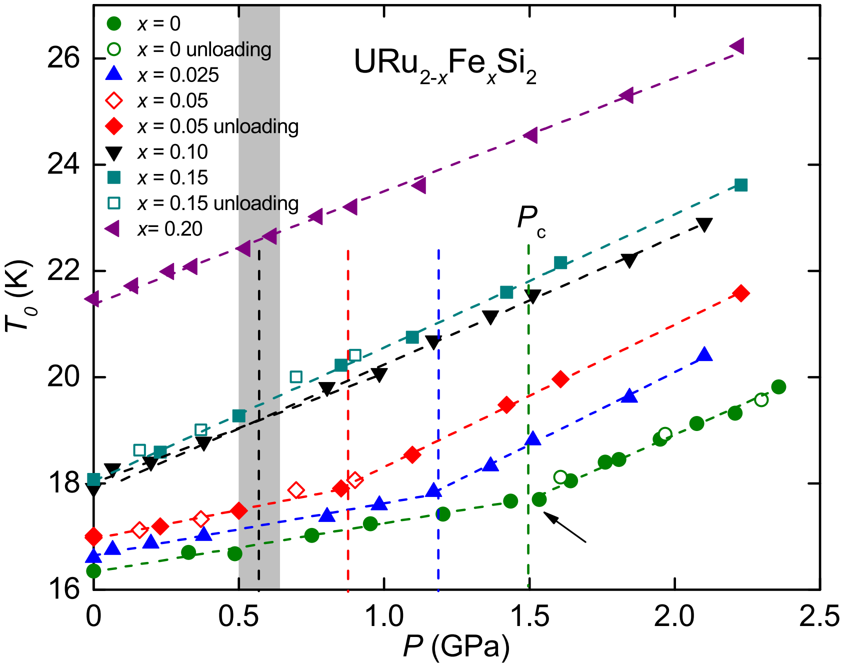

Figure 6.4: The T_0 vs. P phase diagram for $URu_{2-x}Fe_xSi_2$ (x = 0, 0.025, 0.05, 0.10, 0.15, 0.20). The open symbols for the x = 0, 0.05 and 0.15 data represent data taken upon releasing the pressure. The sloped dashed lines are linear fits to the data. The vertical dashed lines indicate the values of the critical pressure P_c = 1.5, 1.17, 0.85, and 0.57 GPa for x = 0, 0.025, 0.05, and 0.10, respectively. The dashed line for the critical pressure P_c = 0 GPa for x = 0.15 has been omitted. The gray rectangle represents the error in determining the critical pressure, P_c = 0.57, for the x = 0.1 compound. The value of P_c is defined as the pressure at the discontinuity in the dT_0/dP curve as indicated, for example, by the black arrow pointing to the kink in the green data. (The green data points shown for x = 0 were taken from Ref. [19].)

data signifies the first-order phase transition from the HO phase to the LMAFM phase occurring in the $URu_{2-x}Fe_xSi_2$ compounds with x = 0, 0.025, 0.05, and 0.10. The HO $\rightarrow$ LMAFM phase transition occurs at a critical pressure, P_c, which is defined as the pressure at the location of the discontinuity in the slope, $\partial T_0/\partial P$, i.e., at the “kink" in the $T_0(P)$ data.

We identify the “kink” in the T_0 vs. P phase boundary as the location of a tricritical point at which point the phase boundary between the HO and LMAFM phases (for $T \leq T_0$) joins with the $T_{HO}(P)$ phase boundary between the PM and HO phases and the $T_N(P)$ phase boundary between the PM phase and high pressure LMAFM phase. In this report,

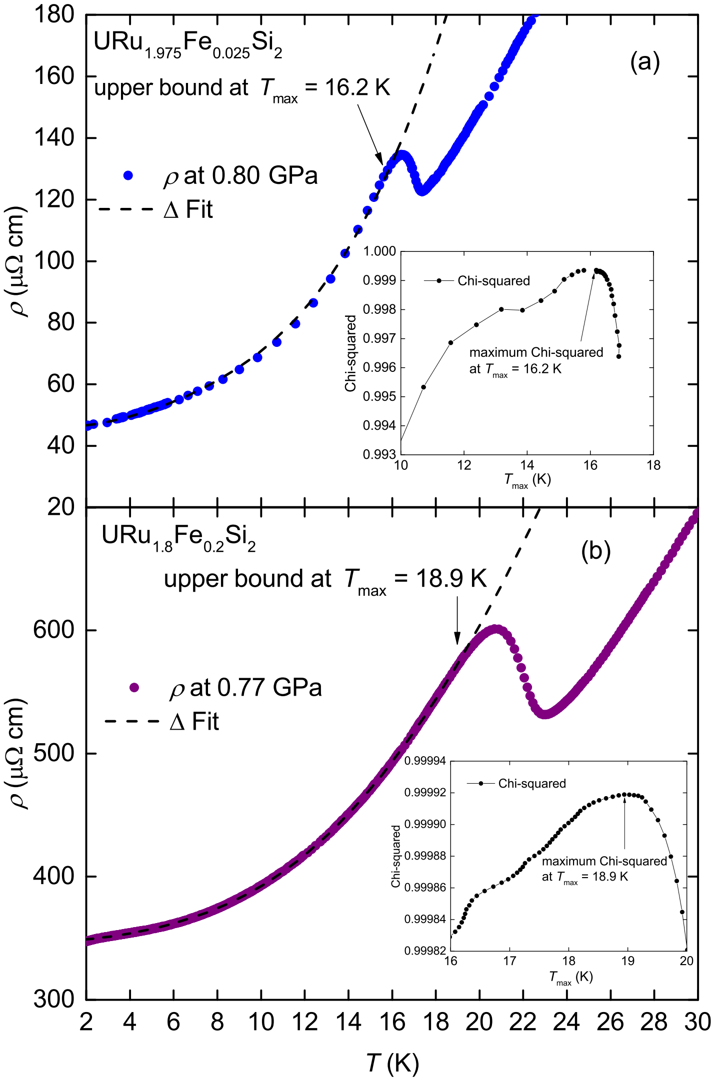

Figure 6.5: Low temperature electrical resistivity $\rho(T)$ for the (a) $x = 0.025$ compound at 0.8 GPa and (b) $x = 0.20$ compound at 0.77 GPa plotted along with a theoretical model for the resistivity (see Equation (6.1) in text), represented by the dashed black curves. The best fit to the $\rho(T)$ data below T_0 was determined by a fitting algorithm as described in the text that allowed for the extraction of the value of the energy gap Δ at various pressures P. Insets: Examples of a plot of Chi-squared vs. T_{max} showing the maximum value of Chi-squared that determined the best fit to the $\rho(T)$ data below T_0.

we were not able to witness any additional features in the electrical resistivity (below T_{HO}) that would allow for the determination of the HO $\rightarrow$ LMAFM phase boundary.

According to theoretical models, [31, 32] it is possible that there may exist a critical end point on the HO $\rightarrow$ LMAFM phase boundary, rather than a tricritical point, if the two ordered phases HO and LMAFM (below T_0) exhibit the same antiferromagnetic symmetry. However, in such a case, the $T_0(P)$ phase boundary between the PM and HO/LMAFM phases would be smooth and absent of a “kink”.[31] Recently, neutron scattering experiments reveal that the magnetic and lattice excitations below T_{HO} in the HO phase do not share the broken symmetries observed in the PM $\rightarrow$ LMAFM phase transition at T_N. [33] To the contrary, the excitations in the HO phase appear to reflect the symmetry observed in the PM phase above T_{HO}. We suggest that the suppression of the “kink” with increasing x in $URu_{2-x}Fe_xSi_2$ as observed in the $T_0(P)$ boundary provides additional evidence for the existence of a true tricritical point in the T_0 vs. P phase diagram in which the ordering in the HO phase exhibits a different symmetry than the ordering in the LMAFM phase. [20, 31]

From the composite plot of the T_0 vs. P phase boundaries for various values of x shown in Fig. 6.4, it is clear that there is a complete suppression of the HO phase in favor of the LMAFM phase with increasing Fe concentration, x, such that the critical pressure decreases from P_c = 1.5 GPa at x = 0 to P_c = 0 GPa at x = 0.15. The shift of this tricritical point to lower critical pressure, P_c, in compounds with higher concentrations of Fe, x, is perhaps the defining and most interesting result of this report and suggests a simple additive relation between chemical pressure, P_{ch}, and applied pressure, P, as tuning parameters for investigating the ordered phases in the $URu_{2-x}Fe_xSi_2$ system.

Referring back to the T_0 vs. x phase boundary shown in Fig. 6.1, it is apparent that the $URu_{2-x}Fe_xSi_2$ compounds, for which $x \geq 0.15$, have already entered the LMAFM phase; in particular, for the $URu_{2-x}Fe_xSi_2$ compound with x = 0.15, the value of the critical pressure is P_c = 0 GPa. Hence, there are no observable kinks in the $T_0(P)$ data shown in Fig. 6.4 for the $URu_{2-x}Fe_xSi_2$ compounds with x = 0.15 and 0.20. However, there are clear discontinuities in the slope $\partial T_0/\partial P$ for $URu_{2-x}Fe_xSi_2$ compounds with x = 0, 0.025, and 0.05 which occur at values of P_c = 1.5, 1.17, and 0.85 GPa, respectively. At low pressure in the HO phase, the rate of change in T_{HO} with P is $\partial T_{HO}/\partial P \sim 1$ K GPa^{-1} (see Table 6.3 below), which is in good agreement with the variation predicted from thermal expansion and specific heat measurements via the Ehrenfest relation. [20, 27, 34] Note that the pressure coefficient, $\partial T_{HO}/\partial P \sim 1$ K GPa^{-1}, is remarkably consistent with the calculated chemical pressure coefficient, $\partial T_{HO}/\partial P_{ch}$ = 1.1 K GPa^{-1}, which further suggests the similarity between these two types of experimental tuning, x and P.

The discontinuity in $\partial T_0/\partial P$ for the $URu_{2-x}Fe_xSi_2$ compound with x = 0.10 is more difficult to identify and requires some comment. First, there is a smaller difference between the slope $\partial T_{HO}/\partial P$ = 2.06 K GPa^{-1} in the HO phase when compared to the slope $\partial T_N/\partial P$ = 2.42 K GPa^{-1} in the LMAFM phase; one explanation for the elevated value of $\partial T_{HO}/\partial P$ for the $URu_{2-x}Fe_xSi_2$ (x = 0.10) compound is that, below T_{HO}, the sample may consist of a mixture of the HO and LMAFM phases. ^{29}Si NMR, [15] ac susceptibility, and elastic neutron scattering experiments [12] performed on the parent compound URu_2Si_2 under pressure revealed a phase separated spatial inhomogeneity in which the HO phase was populated with regions of LMAFM phase. Elastic neutron scattering measurements performed on single crystals of $URu_{2-x}Fe_xSi_2$ prepared in our lab reveal an increase in the U ordered moment with increasing x in the HO phase, consistent with a scenario in which regions of the LMAFM phase coexist with the HO phase. [23] More recently, muon spin rotation (μSR) measurements on samples of $URu_{2-x}Fe_xSi_2$ prepared in another laboratory demonstrated that the HO phase contains phase separated regions of the LMAFM phase in $URu_{2-x}Fe_xSi_2$ compounds with low levels of Fe concentrations. [35] Second, there is an absence of data in the region where P_c is likely to occur. Hence, $P_c \approx 0.57$ GPa was determined from the intersection of the line of fit to the $T_0(P)$ data in the HO phase (the first four black triangles as shown in Fig. 6.4) with the line of fit to the $T_0(P)$ data in the LMAFM phase (the remaining seven black triangles as shown in Fig. 6.4). For ease of comparison, the values of P_c and $\partial T_0/\partial P$ for the $URu_{2-x}Fe_xSi_2$ compounds (x = 0.025, 0.05, 0.10, 0.15, and 0.20) are presented in Table 6.3. Note that the slope ($\partial T_N/\partial P$) in the LMAFM phase is approximately 2.5 times larger than the slope ($\partial T_0/\partial P$) in the HO phase (with the exception of the $URu_{2-x}Fe_xSi_2$ compound with $x = 0.10$).

It is apparent from the slope ($\partial T_0/\partial P$) in the HO and LMAFM phases, that the $URu_{2-x}Fe_xSi_2$ ($x = 0.10$) compound is not fully expressed in the LMAFM phase at ambient pressure. Hence, of the five compounds $URu_{2-x}Fe_xSi_2$ (x = 0, 0.025, 0.05, 0.10, 0.15, and 0.20) that were measured in this study, we determined that $x = 0.15$ is the smallest concentration of Fe in which the $URu_{2-x}Fe_xSi_2$ system is completely in the LMAFM phase, at ambient pressure. The measured value of $x_c^* = 0.15$ for the critical concentration of Fe is close to the estimated value of x_c^* that was determined from the location of the "kink" in the the T_0 vs. x phase boundary shown in Fig. 6.1. Further analysis in the last section of this paper shows that $x = 0.15$ is a reasonable determination of the ambient pressure critical concentration of Fe, x_c^*.

Pressure dependence of the energy gap Δ

The first bulk property measurements of the specific heat and electrical resistivity for the parent compound URu_2Si_2 ($x = 0$) at ambient pressure suggest that the second-order mean-field-like transition from the paramagnetic (PM) phase to the HO/LMAFM phase results in the opening of a charge gap (Δ) over a portion of the Fermi surface. [1, 2, 30] Originally, the gapped portion of the Fermi surface for URu_2Si_2 at ambient pressure had been attributed to the formation of a static charge- or spin-density wave (CDW or SDW) below $T_0 \sim 17.5$ K while the remaining non-gapped portion of the Fermi surface

Table 6.3: Values of the applied critical pressure P_c (for various levels of Fe concentration, x, in the $URu_{2-x}Fe_xSi_2$ system) at the HO → LMAFM phase transition along with the pressure dependence ($\partial T_0/\partial P$) in the HO and LMAFM phases.

x	P_c (GPa)	$\partial T_0/\partial P$ (K GPa^{-1})	
		HO phase	LMAFM phase
0^*	1.50	1.0 ± 0.1	2.5 ± 0.1
0.025	1.17	1.0 ± 0.1	2.7 ± 0.1
0.05	0.85	1.1 ± 0.1	2.7 ± 0.1
0.10	0.57	2.1 ± 0.1	2.4 ± 0.1
0.15	0.00	–	2.5 ± 0.1
0.20	–	–	2.1 ± 0.1

* from Ref. [19]

was thought to be available to superconducting electron states with $T_c \sim 1.5$ K. [2, 30] In this scenario, the coexistence of superconductivity and HO could be thought of as ordered phases that compete for Fermi surface fraction. [2, 19, 36] It is now known that the superconductivity is suppressed with chemical substitution x or applied pressure P, and is eventually destroyed during the first-order phase transition from the HO phase to the LMAFM phase. [2, 16, 37] Additional investigations of the parent compound URu_2Si_2 ($x = 0$) employing various experimental probes such as infrared spectroscopy, [38] Hall effect, [39–41] quantum oscillation measurements, [42] angle-resolved photoemission spectroscopy (ARPES), [43, 44] optical conductivity, [38, 45, 46] and scanning tunneling microscopy (STM), [47, 48] confirm a reorganization of the electronic structure below T_0 which results in a partial gapping of the Fermi surface.

Surprisingly, experiments under pressure, including de Haas-van Alphen (dHvA), [20, 49] Shubnikov-de Haas (SdH), [50] and inelastic neutron scattering experiments, [51] reveal that there is no significant change in the gapped structure of the Fermi surface as the URu_2Si_2 compound undergoes a first-order transition from the HO phase to the LMAFM phase. The electronic reconstruction and partial gapping of the Fermi surface for $T < T_{HO}$ has become one of the more salient features of the HO phase. Although there is still no consensus on a physical explanation for the gapping of the Fermi surface below T_{HO}, a significant amount of experimental work has provided detailed information regarding the electronic structure above and below T_0 in URu_2Si_2.

The formation of a similar energy gap (Δ) over the Fermi surface in the system of Fe-substituted compounds $URu_{2-x}Fe_xSi_2$ is evident from recent measurements of electrical resistivity $\rho(T)$, specific heat $C(T)$, [22, 23, 52] and optical conductivity [24] experiments. Here, we report on values for Δ at the Fermi surface in the HO/LMAFM phase as a function of pressure for the various Fe-substituted compounds $URu_{2-x}Fe_xSi_2$ (x = 0.025, 0.05, 0.10, 0.15, and 0.20). The values of Δ were extracted from fits of the $\rho(T)$ data in the temperature region $T < T_0$ to the expression for electrical resistivity, $\rho(T)$:

$$\rho(T) = \rho_0 + AT^2 + B\Delta^2 \sqrt{\frac{T}{\Delta}} \left[1 + \frac{2}{3}\left(\frac{T}{\Delta}\right) + \frac{2}{15}\left(\frac{T}{\Delta}\right)^2\right] e^{-\frac{\Delta}{T}}. \tag{6.1}$$

The exponential term in Equation (6.1) is the dominant contribution to the electrical resistivity $\rho(T)$ in this temperature region ($T < T_0$) and represents the scattering contribution from the gapped spin excitations that are characteristic of antiferromagnetic ordering.[25] Other scattering contributions to $\rho(T)$ in this temperature region include the residual resistivity ρ_0 and the scattering associated with electron-electron interactions that are characteristic of a Fermi liquid, AT^2. We briefly note that earlier reports on measurements of $\rho(T)$ for high purity URu_2Si_2 (x = 0) samples with values of RRR $\sim$ 100 suggest that the AT^2 dependence fails to describe the HO phase which is better described by a power law behavior of AT^{α}, where α = 1.6. [29, 53] Furthermore, a power law exponent AT^{α}, where $\alpha < 2$, is typically required to represent the electrical resistivity $\rho(T)$ in the temperature range just above T_c. [20] However, Fermi liquid behavior is assumed to be valid in the low temperature region down to 2 K in this study owing to substantial levels of Fe solutes present in single crystal samples from the $URu_{2-x}Fe_xSi_2$ system with x = 0.025, 0.05, 0.10, 0.15, and 0.20 which exhibited low values of RRR $<$ 10 (see Fig. 6.2). In addition, there was no evidence for the onset of superconductivity in the $\rho(T)$ curves down to 1 K for any of the Fe-substituted $URu_{2-x}Fe_xSi_2$ (x = 0.025, 0.05, 0.10, 0.15, and 0.20) samples measured in this study. Hence, while a $T^{1.6}$ dependence is likely to apply at low temperatures near 2 K for high-purity parent compounds that exhibit superconductivity with a T_c $\sim$ 1.5K or below, we note that a T^2 dependence is applicable down to $T \sim 2$ K for the "dirty" Fe-substituted compounds measured in this study. The assumption of the existence of Fermi liquid behavior below T_0 in our samples of $URu_{2-x}Fe_xSi_2$ (x = 0.025, 0.05, 0.10, 0.15, and 0.20) is supported by the recent optical conductivity experiments performed on $URu_{2-x}Fe_xSi_2$ compounds which demonstrated that scattering processes typical of a Fermi liquid were present in both the HO and LMAFM phases.[24]

Examples of curves that were fitted to the $\rho(T)$ data based on Equation (6.1) for the two $URu_{2-x}Fe_xSi_2$ (x = 0.025 and 0.20) compounds at 0.80 and 0.77 GPa, respectively, are displayed in Fig. 6.5. The $\rho(T)$ data and the fitted curve (dashed black line) in Fig. 6.5 (a) correspond to the $URu_{2-x}Fe_xSi_2$ (x = 0.025) compound under pressure at P = 0.80 GPa which is an example of a $URu_{2-x}Fe_xSi_2$ compound that is in the HO phase for the temperature region of the fit. Similarly, the $\rho(T)$ data and the fitted curve (dashed black line) in Fig. 6.5 (b) correspond to the $URu_{2-x}Fe_xSi_2$ (x = 0.2) compound under pressure at P = 0.77 GPa which is an example of a $URu_{2-x}Fe_xSi_2$ compound that is in the LMAFM phase for the temperature region of the fit.

The fit of Equation (6.1) to the $\rho(T)$ data was performed over the temperature range from T = 2 K to T_{max}, where T_{max} represents the upper bound on the temperature range of the $\rho(T)$ data used for the fit. The value of T_{max} was allowed to vary in order to determine the region of data (below T_0) that yielded the best fit. Hence, the best fit of the $\rho(T)$ data to Equation (6.1) was determined by plotting Chi-squared vs. T_{max} (as displayed in the inset of Fig. 6.5 (a)). From the Chi-squared vs. T_{max} plot, the determination of T_{max} that yielded the best fit to the $\rho(T)$ data is the value of T_{max} at which Chi-squared

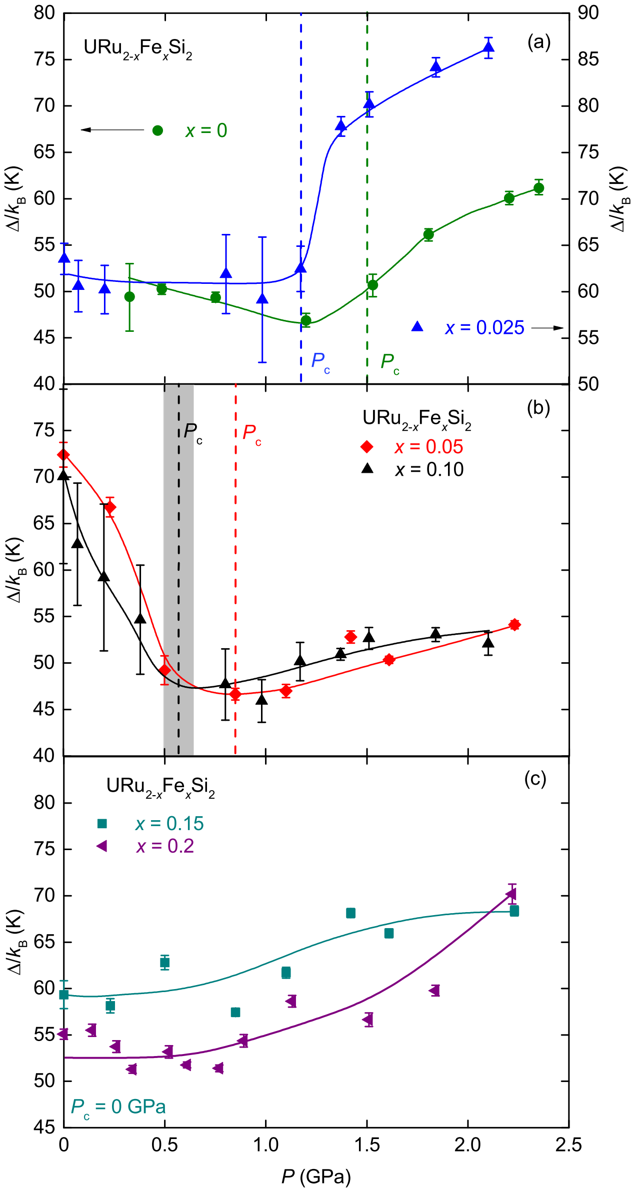

Figure 6.6: Energy gap Δ vs. pressure P for (a) $x = 0$ and 0.025, (b) $x = 0.05$ and 0.10, and (c) $x = 0.15$ and 0.20. The value of Δ was determined by fitting a theoretical model of electrical resistivity $\rho(T)$ (see Equation (6.1) in text) to the low temperature electrical resistivity $\rho(T)$ data. The critical pressure P_c and the occurrence of the first-order phase transition from the HO phase to the LMAFM phase are denoted by the dashed vertical lines. The gray rectangle in panel (b) is the error associated in determining the value of P_c for the $x = 0.1$ sample (see text). The values of P_c were determined from the T_0 vs. P phase boundaries shown in Fig. 6.4. Error bars were determined by the fitting algorithm and the solid curved lines are guides to the eye. (The green data points shown for $x = 0$ were taken from Ref. [19].)

is maximized. In the case of the $\rho(T)$ data displayed in Fig. 6.5 (a), the upper bound in temperature corresponding to the best fit was determined to be T = 16.2 K. In the case of the $\rho(T)$ data displayed in Fig. 6.5 (b), the upper bound in temperature corresponding to the best fit was determined to be T = 18.9 K.

The pressure dependence ($\partial\Delta/\partial P$) of the extracted values of the charge gap (Δ) based on the fits of Equation (6.1) to the $\rho(T)$ data for the $\mathrm{URu_{2-x}Fe_xSi_2}$ (x = 0.025, 0.05, 0.10, 0.15, and 0.20) compounds is displayed in Fig. 6.6. The $\Delta(P)$ behavior for the $\mathrm{URu_2Si_2}$ (x = 0) parent compound from Ref. [19], as displayed in Fig. 6.6 (a), was determined in a similar fashion; however, a slightly different theoretical model for the electrical resistivity that is based on scattering from gapped ferromagnetic (rather than antiferromagnetic) spin excitations [54, 55] was used in the fit to the $\rho(T)$ data in Ref. [19]. The differences in the magnitude of Δ extracted from the two different theoretical models of $\rho(T)$ are small and the overall qualitative behavior of the pressure dependence of the gap was shown to be unaffected. [22]

The behavior of $\Delta(P)$ for the six compounds $\mathrm{URu_{2-x}Fe_xSi_2}$ (x = 0, 0.025, 0.05, 0.10, 0.15, and 0.20) have been grouped and plotted in pairs: (x = 0, 0.025), (0.05, 0.10), and (0.15, 0.20) are displayed in Fig. 6.6 (a), (b), and (c), respectively. The dashed vertical lines in Fig. 6.6 indicate locations of the critical pressure, P_c, in the $\Delta(P)$ plots and were determined from the T_0 vs. P phase diagram displayed in Fig. 6.4. For the $\mathrm{URu_{2-x}Fe_xSi_2}$ (x = 0.15) compound, the vertical dashed line corresponding to a critical pressure at P_c = 0 GPa has been omitted. There is a noticeable change in the pressure dependence ($\partial\Delta/\partial P$) of the gap ($\Delta$) at $P \sim$ 1.2, 0.8, and 0.6 GPa for the $\mathrm{URu_{2-x}Fe_xSi_2}$ compounds with x = 0.025, 0.05, and 0.10, respectively. These values of pressure are remarkably consistent with the critical pressures, P_c = 1.17, 0.85, and 0.57 GPa (represented by the vertical dashed lines in Fig. 6.6). As determined in Ref. [19], there is also a turnaround in the $\Delta(P)$ behavior for the $\mathrm{URu_2Si_2}$ parent compound (green circles in Fig. 6.6 (a)). The turnaround (or the minimum in $\Delta(P)$) occurs at a pressure of $P \sim 1.3$ GPa, which is slightly lower than the critical pressure, P_c = 1.5 GPa. The pressure dependence of the gap ($\partial\Delta/\partial P$) for the two $URu_{2-x}Fe_xSi_2$ compounds with x = 0.15 and 0.20, both of which already exhibit the LMAFM phase at ambient pressure, is displayed in Fig. 6.6 (c). For these two compounds, there is no non-zero critical pressure, P_c, and hence there is only the monotonic dependence ($\partial\Delta/\partial P > 0$ for $P > 0$) observed in $\Delta(P)$. The monotonic dependence of $\Delta(P)$ is consistent with the monotonic behavior of $\Delta(P)$ above the critical pressure in the LMAFM phase observed for the other four compounds $URu_{2-x}Fe_xSi_2$ (x = 0, 0.025, 0.05, 0.10). (For ease of comparison, there is a correspondence in the color scheme (with regard to Fe concentration, x) between the $\Delta(P)$ curves displayed in Fig. 6.6 and the $T_0(P)$ data in the plot of the T_0 vs. P phase boundaries displayed in Fig. 6.4.)

From the plots of $\Delta(P)$ that are displayed in Fig. 6.6 for the six $URu_{2-x}Fe_xSi_2$ compounds with (x = 0, 0.025, 0.05, 0.10, 0.15, and 0.20), there is a clear qualitative difference in the $\Delta(P)$ behavior observed in the (low presssure) HO phase, where $\partial\Delta/\partial P < 0$, and the (high pressure) LMAFM phase, where there is a positive pressure coefficient, $\partial\Delta/\partial P > 0$. This behavior seems to be consistent with previous reports on the evolution of the energy gap, Δ, with increases in either x or P. Electrical resistivity measurements performed in an earlier study of single crystals of the parent compound URu_2Si_2 (x = 0) under pressure reveal a monotonic decrease in the Fermi surface gap Δ from $\sim$ 77 to 70 K in the HO phase followed by a jump in Δ to a saturated value of $\sim$ 100 K in the LMAFM phase at $P_x \sim 0.5$ GPa. [56] Similar behavior was observed in the evolution of the energy gap, Δ, as a function of Fe concentration, x. The values for Δ were extracted from a theoretical fit to the specific heat data, $C(T)$, for single crystal samples of $URu_{2-x}Fe_xSi_2$ in which there is a slight suppression of Δ from 93 K down to 80 K in the HO phase for increasing Fe concentration up to $x \sim 0.10$ at which point there is a jump in the value of Δ to $\sim$ 110 K in the LMAFM phase. [23]

It is interesting to note that as the temperature is lowered below T_0, the commensurate $\mathbf{Q_0}$ = (1,0,0) and incommensurate $\mathbf{Q_1}$ = (1 ± 0.4,0,0) spin excitations in the parent compound URu_2Si_2, exhibit well defined peaks in the energy spectrum which are gapped at energies below $\sim$ 2 meV (or 22 K) and $\sim$ 4.5 meV (or 50 K), respectively. [8, 45, 57] It has been suggested that below T_0, the two spin excitations at $\mathbf{Q_0}$ and $\mathbf{Q_1}$ are strongly coupled to the charge degree of freedom, suggesting that there is a fundamental relationship between the SDW gaps at $\mathbf{Q_0}$ and $\mathbf{Q_1}$ and the charge (CDW) gap Δ that opens up over the Fermi surface. [45, 57, 58]

It is now known that the partial gapping of the Fermi surface below T_0 is anisotropic with respect to the *a* and *c* axes. [24, 45] Furthermore, a comparison of the gapped spin excitations observed in neutron scattering experiments [57] with the energy gaps observed in optical conductivity experiments [24, 45] strongly suggests that the anisotropy observed in the charge gap, Δ, over the Fermi surface is such that the *a*-axis charge gap is linked to the $\mathbf{Q_0}$ spin excitation while the *c*-axis charge gap is linked to the $\mathbf{Q_1}$ spin excitation. [24, 45]

The two different spin excitation gaps, Δ_0 (commensurate) and Δ_1 (incommensurate), are further distinguished in their behavior under applied pressure. While increasing applied pressure has the effect of increasing the energy gap Δ_1, it has the opposite effect of decreasing the energy gap Δ_0. [59] The Δ_0 behavior was confirmed in a later report where the energy gap Δ_0 for the commensurate excitation at $\mathbf{Q_0}$ was observed to monotonically decrease with increasing pressure up until the critical pressure, P_c, at which point the $\mathbf{Q_0}$ excitation completely disappears at the HO → LMAFM phase transition. [51] In contrast, the Δ_1 energy gap was observed to increase with pressure in the HO phase below P_c and then survive the first-order HO → LMAFM transition at which point Δ_1 jumps discontinuously to a larger value and then remains constant with increasing pressure into the LMAFM phase. [56, 60] Here, we simply note the correspondence in the HO phase between the behavior of $\Delta_0(P)$ and the behavior we obtained for $\Delta(P)$ as well as the correspondence in the LMAFM phase between the behavior of $\Delta_1(P)$ and the behavior we observed for $\Delta(P)$.

Our determination of the Fermi surface gap, Δ, which is based on a theoretical model of electrical resistivity fitted to the $\rho(T)$ data from bulk transport measurements under pressure surely cannot capture all of the subtle details that are becoming known regarding the response of the Fermi surface to experimental tuning at temperatures below T_0. Nevertheless, it appears that such a theoretical model of electrical resistivity used in the analysis of bulk measurements of $\rho(T)$ may still capture some of the important features of the charge gap (Δ) that are observed in more direct measurements of the Fermi surface in the HO and LMAFM phases. Namely, the gap analysis performed here seems to capture the differences in the pressure variation, $\partial\Delta/\partial P$, for the HO and LMAFM phases and also finds the magnitude of the charge gap, Δ, to be consistent with previous reports.

The simultaneous tuning of URu_2Si_2 with chemical and applied pressure

Perhaps the most interesting aspect of this report is the systematic and predictable manner in which Fe substitution, x, combines with applied pressure, P, to affect the ordered phases and phase transitions observed in URu_2Si_2. The three-dimensional plot of the T_0 vs. P phase boundaries for various values of x displayed in Fig. 6.7 summarizes the response of the transition temperature, T_0, to the simultaneous tuning of the URu_2Si_2 compound with Fe substitution at x = 0.025, 0.05, 0.1, 0.15, and 0.2 while under applied pressure up to P = 2.2 GPa. The sloped dashed black lines are linear fits to the six sets of $T_0(P)$ data for the $URu_{2-x}Fe_xSi_2$ compounds at the various Fe concentrations, x = 0, 0.025, 0.05, 0.10, 0.15, and 0.20. (The x = 0 data were taken from Ref. [19].) There are obvious "kinks" in the $T_0(P)$ data for the $URu_{2-x}Fe_xSi_2$ compounds with $x \leq 0.10$. The

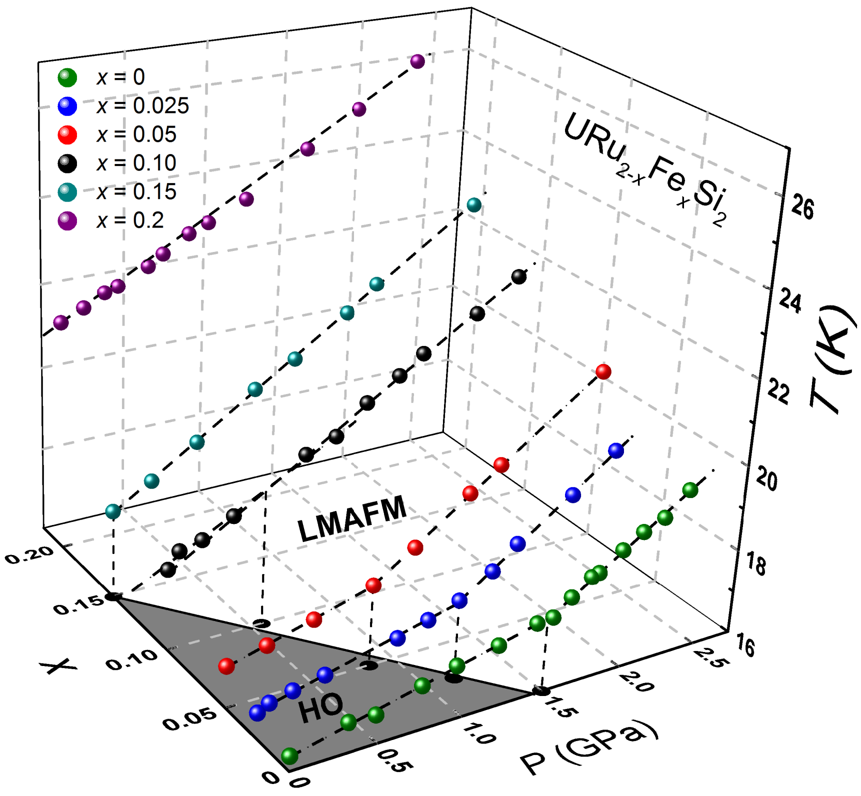

Figure 6.7: Plot of the T_0 vs. P phase boundaries for various values of x for $URu_{2-x}Fe_xSi_2$ (x = 0, 0.025, 0.05, 0.10, 0.15, and 0.20). The vertical dashed lines drop down to the x-P plane at the respective critical pressures P_c and help determine the boundary between the HO and LMAFM phases in the x-P plane. The HO/LMAFM phase boundary is represented by the solid black line in the x-P plane which is a linear fit of the black circles. At the critical concentration of x_c^* = 0.15 and above, the compounds have already entered the LMAFM phase at ambient pressure. (The green data points shown for x = 0 are not part of this study and were taken from an earlier study of $URu_{2-x}Fe_xSi_2$ under pressure by Jeffries *et al.* in Ref. [19].)

"kinks" correspond to the discontinuities in the slope, $\partial T_0/\partial P$, which mark the first-order HO $\rightarrow$ LMAFM phase transition. The slopes, $\partial T_0/\partial P$, of the various $T_0(P)$ curves are presented in Table 6.3 along with the values of the critical pressure, P_c, for the respective first-order HO $\rightarrow$ LMAFM phase transitions.

The filled black circles in the x-P plane are the planar projections of the "kinks" (or points of discontinuity in $\partial T_0/\partial P$) that appear in the $T_0(P)$ data (filled colored spheres) of the three dimensional phase diagram. The vertical dashed black lines are drawn to illus-

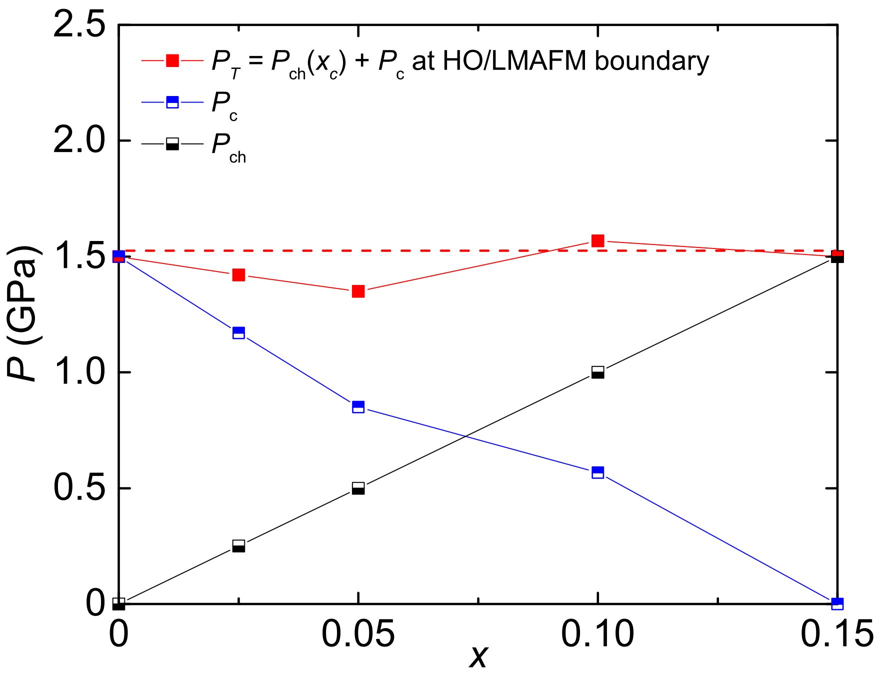

Figure 6.8: A plot of the chemical pressure P_{ch} (black symbols), critical applied pressure P_c (blue symbols), and the total pressure P_T (red symbols) = $P_{ch}(x_c) + P_c$. The additive behavior of P_{ch} and P_c such that $P_{ch}(x_c) + P_c \approx 1.5$ GPa is consistent with earlier reports on the "kink" in the $T_0(P)$ phase diagram at $P = 1.5$ GPa for the parent compound URu_2Si_2 ($x = 0$). [19]

trate the planar projections onto the x-P plane. The solid black line in the x-P plane, which represents the phase boundary between the HO phase (gray region) and the LMAFM phase (white region), is a linear fit to the projected points (filled black circles) in the x-P plane. The extrapolation of this linear fit in the x-P plane to the $P = 0$ GPa line indicates that the ambient pressure critical concentration of Fe that forces the transition into the LMAFM phase is $x_c^* = 0.15$. Similarly, the extrapolation of the same linear fit in the x-P plane to the $x = 0$ line indicates that, in the absence of Fe substitution ($x = 0$), the critical pressure that forces the transition into the LMAFM phase is very nearly $P_c = 1.5$ GPa, which is the value of the critical pressure, P_c, that was determined in several reports of other types of measurements of the URu_2Si_2 ($x = 0$) parent compound under pressure (see Table 7.1).

Hence, the ambient pressure critical concentration of Fe that was determined in this report to be $x_c^* = 0.15$ can be thought to be equivalent to the critical value of applied pressure, $P_c = 1.5$ GPa, that induces the HO $\rightarrow$ LMAFM phase transiton. This allowed us to determine the linear dependence of the chemical pressure, $P_{ch}(x)$, on the Fe concentration x, such that the $P_{ch}(x)$ line, the solid black line shown in Fig. 6.8, passes through the two points: (P, x) = (0 GPa, 0) and (1.5 GPa, 0.15). We were then able to compare the slope of the $P_{ch}(x)$ line as shown in Fig. 6.8 with an x to $P_{ch}(x)$ conversion that is based on a bulk modulus β calculation that relates the relative change in the unit cell volume, d(V/V_0), to the change in pressure, dP: $\beta = 1/\kappa_T = -\mathrm{d}(V/V_0)/\mathrm{d}P$, where V_0 is the initial volume of the unit cell at ambient pressure and κ_T is the isothermal compressibility. From this comparison, we determined the value of the isothermal compressibility for $\mathrm{URu_2Si_2}$: $\kappa_T = 4.5 \times 10^{-3}$ GPa^{-1}. It should be mentioned that a bulk modulus calculation of $P_{ch}(x)$ can vary depending on which value of κ_T is used from the range of values that are reported in the literature. Interestingly, our determination of the value for $\kappa_T = 4.5 \times 10^{-3}$ GPa^{-1} is the mean value of the extreme values of 2×10^{-3} and 7.3×10^{-3} GPa^{-1} reported in the literature. [14, 61]

Based on our determination of the $P_{ch}(x)$ line, we note the consistency in which $P_{ch}(x_c) + P_c \approxeq 1.5$ GPa as displayed in Fig. 6.8. The blue and black half-filled squares represent the chemical pressure, P_{ch}, and critical pressure, P_c, respectively, whereas the filled red squares represent the combined effect of experimental tuning or "total" pressure, $P_T = P_{ch}(x_c) + P_c$, that resulted in a first-order transition from the HO to LMAFM phase. The dashed red line at $P = 1.5$ GPa is for reference and allows for a comparison to the P_T values. Remarkably, for each combination of x and P, the chemical pressure and applied pressure consistently sum to the value of 1.5 GPa to force the HO $\rightarrow$ LMAFM phase transition. The consistency with which the combination of x and P affect the ordered phases in $\mathrm{URu_2Si_2}$ reinforces the idea that the substitution of smaller Fe ions for Ru acts as a "chemical pressure", whereby a reduction in the unit-cell volume affects the compound in a nearly (disregarding disorder) equivalent manner as applying external pressure.

It is clear from the T_0 vs. x phase boundary shown in Fig. 6.1 that a decrease in the concentration of Fe, which effectively expands the volume of the unit-cell in compounds from the $URu_{2-x}Fe_xSi_2$ series, results in a suppression of T_0. Hence, assuming that "chemical pressure" is the effective mechanism responsible for changes in T_0, an isoelectronic substitution involving a larger ion relative to Ru, such as Os, that results in an expansion of the unit cell volume, should also result in a suppression of T_0. However, experiments on both polycrystalline [52] and single crystal [24] samples of $URu_{2-y}Os_ySi_2$ reveal that as the Os concentration, y, is increased in the $URu_{2-y}Os_ySi_2$ series, there is an enhancement, rather than a suppression, in T_0, that is observed in both the HO and LMAFM phases. This behavior is very similar to the evolution of T_0 that is observed with increasing Fe concentration x in the $URu_{2-x}Fe_xSi_2$ series or with increasing pressure, P, for the parent compound URu_2Si_2. Hence, for the Os substituted compounds from the $URu_{2-y}Os_ySi_2$ series, the evolution of T_0 appears to depend on more than "chemical pressure" alone. An investigation involving the experimental tuning of URu_2Si_2 with Os substitution under applied pressure would be interesting in order to answer the question of how a "negative chemical pressure" and an externally applied pressure work together in a system where other mechanisms seem to be at play in affecting T_0 and the HO $\rightarrow$ LMAFM transition. Such an investigation is currently in progress in our laboratory.

6.4 Concluding Remarks

By tuning the parent compound, URu_2Si_2, with an isoelectronic substitution of Fe for Ru, we found that we could bias the material with "chemical pressure" so that a lesser amount of applied external pressure is required to induce the transition to the high pressure LMAFM phase. The results presented here indicate that one can consistently induce the high pressure LMAFM phase in URu_2Si_2 with the appropriate x and P combination that yields $P_{ch}(x) + P_c \approxeq 1.5$ GPa. The critical values of x and P determined in this report seem to be consistent with previous studies in which the URu_2Si_2 compound was experimentally tuned independently with either x or P. [19, 22–24] However, the extra degree of freedom gained in experimentally tuning the URu_2Si_2 compound simultaneously with both x and P offers a number of advantages. Namely, key aspects of the phase diagrams such as the tricritical point (or critical pressure) become dynamic rather than static features that can be tracked with variations in x or P. As an unexpected consequence of the simultaneous tuning of the URu_2Si_2 compound with x and P, we were also able to “measure” the isothermal compressibility, κ_T, for this material and compare its value with others reported in the literature. [14, 61]

The suggestion that the response of the URu_2Si_2 compound to “chemical pressure” is nearly equivalent to that of applied pressure presents new opportunities for experiments to be performed on the $URu_{2-x}Fe_xSi_2$ system using STM and ARPES techniques that traditionally cannot be performed under pressure. We further suggest here that the simultaneous tuning of URu_2Si_2 with both Fe substitution and external pressure can serve as a workaround to the current limitations on the amount of pressure that can be applied with the various pressure cells that are used in certain neutron scattering experiments. By experimentally tuning the URu_2Si_2 compound with x, it would be possible to bias the compound with chemical pressure at the outset of the neutron experiment so that larger regions of phase space could be studied in the upper pressure limit where quantum criticality might be explored.

Acknowledgements

Chapter 6, in full, is a reprint of the article, “Evolution of critical pressure with increasing Fe substitution in the heavy-fermion system $URu_{2-x}Fe_xSi_2$,” by C. T. Wolowiec, N. Kanchanavatee, K. Huang, S. Ran, and M. B. Maple, as it appears in *Phys. Rev. B* **94**, 085145 (2016). The dissertation author was the primary investigator and author of this paper.

BIbliography

[1] T. T. M. Palstra, A. A. Menovsky, J. v. d. Berg, A. J. Dirkmaat, P. H. Kes, G. J. Nieuwenhuys, and J. A. Mydosh, "Superconducting and Magnetic Transitions in the Heavy-Fermion System URu_2Si_2", Phys. Rev. Lett. **55**, 2727–2730 (1985).

[2] M. B. Maple, J. W. Chen, Y. Dalichaouch, T. Kohara, C. Rossel, M. S. Torikachvili, M. W. McElfresh, and J. D. Thompson, "Partially Gapped Fermi Surface in the Heavy-Electron Superconductor URu_2Si_2", Phys. Rev. Lett. **56**, 185–188 (1986).

[3] W. Schlabitz, J. Baumann, B. Pollit, U. Rauchschwalbe, H. M. Mayer, U. Ahlheim, and C. D. Bredl, "Superconductivity and Magnetic Order in a Strongly Interacting Fermi-System: URu_2Si_2", Z. Phys. B - Condensed Matter **62**, 171–177 (1986).

[4] E. Fawcett, "Spin-density-wave antiferromagnetism in chromium", Rev. Mod. Phys. **60**, 209–283 (1988).

[5] R. A. Fisher, S. Kim, Y. Wu, N. E. Phillips, M. W. McElfresh, M. S. Torikachvili, and M. B. Maple, "Specific heat of URu_2Si_2: Effect of pressure and magnetic field on the magnetic and superconducting transitions", Physica B **163**, 419–423 (1990).

[6] J. A. Mydosh and P. M. Oppeneer, "*COLLOQUIUM* : HIDDEN ORDER, SUPERCONDUCTIVITY, AND MAGNETISM: THE UNSOLVED CASE OF URU_2SI_2", Rev. Mod. Phys. **83**, 1301–1322 (2011).

[7] J. A. Mydosh and P. M. Oppeneer, "Hidden order behaviour in URu_2Si_2 (A critical review of the status of hidden order in 2014)", Philos. Mag. **94**, 3642–3662 (2014).

[8] C. Broholm, J. K. Kjems, W. J. L. Buyers, P. Matthews, T. T. M. Palstra, A. A. Menovsky, and J. A. Mydosh, "Magnetic Excitations and Ordering in the Heavy-Electron Superconductor URu_2Si_2", Phys. Rev. Lett. **58**, 1467–1470 (1987).

[9] E. D. Isaacs, D. B. McWhan, R. N. Kleiman, D. J. Bishop, G. E. Ice, P. Zschack, B. D. Gaulin, T. E. Mason, J. D. Garrett, and W. J. L. Buyers, "X-Ray Magnetic Scattering in Antiferromagnetic URu_2Si_2", Phys. Rev. Lett. **65**, 3185–3188 (1990).

[10] H. Ptasiewicz-Bak, J. Leciejewicz, and A. Zygmunt, "Neutron diffraction study of magnetic ordering in UPd_2Si_2 , UPd_2Ge_2, URh_2Si_2 and URh_2Ge_2", J. Phys. F **11**, 1225 (1981).

[11] L. CheŁmicki, J. Leciejewicz, and A. Zygmunt, "Magnetic properties of UT_2Si_2 and UT_2Ge_2 (T = Co, Ni, Cu) intermetallic systems", J. Phys. Chem. Solids **46**, 529–538 (1985).

[12] H. Amitsuka, K. Matsuda, I. Kawasaki, K. Tenya, M. Yokoyama, C. Sekine, N. Tateiwa, T. Kobayashi, S. Kawarazaki, and H. Yoshizawa, "Pressure-temperature phase diagram of the heavy-electron superconductor URu_2Si_2", J. of Magn. and Magn. Mater. **310**, 214–220 (2007).

[13] P. G. Niklowitz, C. Pfleiderer, T. Keller, M. Vojta, Y.-K. Huang, and J. A. Mydosh, "Parasitic Small-Moment Antiferromagnetism and Nonlinear Coupling of Hidden Order and Antiferromagnetism in URu_2Si_2 Observed by Larmor Diffraction", Phys. Rev. Lett. **104**, 106406 (2010).

[14] H. Amitsuka, M. Sato, N. Metoki, M. Yokoyama, K. Kuwahara, T. Sakakibara, H. Morimoto, S. Kawarazaki, Y. Miyako, and J. A. Mydosh, "Effect of Pressure on Tiny Antiferromagnetic Moment in the Heavy-Electron Compound URu_2Si_2", Phys. Rev. Lett. **83**, 5114–5117 (1999).

[15] K. Matsuda, Y. Kohori, T. Kohara, K. Kuwahara, and H. Amitsuka, "Spatially Inhomogeneous Development of Antiferromagnetism in URu_2Si_2: Evidence from ^{29}Si NMR under Pressure", Phys. Rev. Lett. **87**, 087203 (2001).

[16] M. W. McElfresh, J. D. Thompson, J. O. Willis, M. B. Maple, T. Kohara, and M. S. Torikachvili, "Effect of pressure on competing electronic correlations in the heavy-electron system URu_2Si_2", Phys. Rev. B **35**, 43–47 (1987).

[17] G. Motoyama, T. Nishioka, and N. K. Sato, "Phase Transition between Hidden and Antiferromagnetic Order in URu_2Si_2", Phys. Rev. Lett. **90**, 166402 (2003).

[18] A. Amato, M. J. Graf, A. de Visser, H. Amitsuka, D. Andreica, and A. Schenck, "Weak-magnetism phenomena in heavy-fermion superconductors: selected μSR studies", J. of Phys.: Condens. Matter **16**, S4403 (2004).

[19] J. R. Jeffries, N. P. Butch, B. T. Yukich, and M. B. Maple, "Competing Ordered Phases in URu_2Si_2: Hydrostatic Pressure and Rhenium Substitution", Phys. Rev. Lett. **99**, 217207 (2007).

[20] E. Hassinger, G. Knebel, K. Izawa, P. Lejay, B. Salce, and J. Flouquet, "Temperature-pressure phase diagram of URu_2Si_2 from resistivity measurements and ac calorimetry: Hidden order and Fermi-surface nesting", Phys. Rev. B **77**, 115117 (2008).

[21] N. P. Butch, J. R. Jeffries, S. Chi, J. B. Leão, J. W. Lynn, and M. B. Maple, "Antiferromagnetic critical pressure in URu_2Si_2 under hydrostatic conditions", Phys. Rev. B **82**, 060408 (2010).

[22] N. Kanchanavatee, M. Janoschek, R. E. Baumbach, J. J. Hamlin, D. A. Zocco, K. Huang, and M. B. Maple, "Twofold enhancement of the hidden-order/large-moment

antiferromagnetic phase boundary in the $URu_{2-x}Fe_xSi_2$ system", Phys. Rev. B **84**, 245122 (2011).

[23] P. Das, N. Kanchanavatee, J. S. Helton, K. Huang, R. E. Baumbach, E. D. Bauer, B. D. White, V. W. Burnett, M. B. Maple, J. W. Lynn, and M. Janoschek, "Chemical pressure tuning of URu_2Si_2 via isoelectronic substitution of Ru with Fe", Phys. Rev. B **91**, 085122 (2015).

[24] J. S. Hall, M. R. Movassagh, M. N. Wilson, G. M. Luke, N. Kanchanavatee, K. Huang, M. Janoschek, M. B. Maple, and T. Timusk, "Electrodynamics of the antiferromagnetic phase in URu_2Si_2", Phys. Rev. B **92**, 195111 (2015).

[25] M. B. Fontes, J. C. Trochez, B. Giordanengo, S. L. Bud'ko, D. R. Sanchez, E. M. Baggio-Saitovitch, and M. A. Continentino, "Electron-magnon interaction in *R*NiBC ($R =$ Er, Ho, Dy, Tb, and Gd) series of compounds based on magnetoresistance measurements", Phys. Rev. B **60**, 6781–6789 (1999).

[26] T. F. Smith, C. W. Chu, and M. B. Maple, "Superconducting manometers for high pressure measurement at low temperature", Cryogenics **9**, 53 (1969).

[27] S. Ran, C. T. Wolowiec, I. Jeon, N. Pouse, N. Kanchanavatee, K. Huang, D. Martien, T. DaPron, D. Snow, M. Williamsen, S. Spagna, P. S. Riseborough, and M. B. Maple, "Phase diagram and thermal expansion measurements on the system of $URu_{2-x}Fe_xSi_2$", (2016).

[28] J. R. Jeffries, N. P. Butch, B. T. Yukich, and M. B. Maple, "The evolution of the ordered states of single-crystal URu_2Si_2 under pressure", J. of Phys.: Condens. Matter **20**, 095225 (2008).

[29] T. D. Matsuda, E. Hassinger, D. Aoki, V. Taufour, G. Knebel, N. Tateiwa, E. Yamamoto, Y. Haga, Y. Ōnuki, Z. Fisk, and J. Flouquet, "Details of Sample Dependence and Transport Properties of URu_2Si_2", J. Phys. Soc. Jpn. **80**, 114710 (2011).

[30] T. T. M. Palstra, A. A. Menovsky, and J. A. Mydosh, "Anisotropic electrical resistivity of the magnetic heavy-fermion superconductor URu_2Si_2", Phys. Rev. B **33**, 6527–6530 (1986).

[31] V. P. Mineev and M. E. Zhitomirsky, "Interplay between spin-density wave and induced local moments in URu_2Si_2", Phys. Rev. B **72**, 014432 (2005).

[32] N. Shah, P. Chandra, P. Coleman, and J. A. Mydosh, "Hidden order in URu_2Si_2", Phys. Rev. B **61**, 564–569 (2000).

[33] N. P. Butch, M. E. Manley, J. R. Jeffries, M. Janoschek, K. Huang, M. B. Maple, A. H. Said, B. M. Leu, and J. W. Lynn, "Symmetry and correlations underlying hidden order in URu_2Si_2", Phys. Rev. B **91**, 035128 (2015).

[34] A. de Visser, F. E. Kayzel, A. A. Menovsky, J. J. M. Franse, J. van den Berg, and G. J. Nieuwenhuys, "Thermal expansion and specific heat of monocrystalline URu_2Si_2", Phys. Rev. B **34**, 8168–8171 (1986).

[35] M. N. Wilson, T. J. Williams, Y.-P. Cai, A. M. Hallas, T. Medina, T. J. Munsie, S. C. Cheung, B. A. Frandsen, L. Liu, Y. J. Uemura, and G. M. Luke, "Antiferromagnetism and hidden order in isoelectronic doping of URu_2Si_2", Phys. Rev. B **93**, 064402 (2016).

[36] G. Bilbro and W. L. McMillan, "Theoretical model of superconductivity and the martensitic transformation in *A*15 compounds", Phys. Rev. B **14**, 1887–1892 (1976).

[37] Y. Dalichaouch, M. B. Maple, J. W. Chen, T. Kohara, C. Rossel, M. S. Torikachvili, and A. L. Giorgi, "Effect of transition-metal substitutions on competing electronic transitions in the heavy-electron compound URu_2Si_2", Phys. Rev. B **41**, 1829–1836 (1990).

[38] D. A. Bonn, J. D. Garrett, and T. Timusk, "Far-Infrared Properties of URu_2Si_2", Phys. Rev. Lett. **61**, 1305–1308 (1988).

[39] J. Schoenes, C. Schönenberger, J. J. M. Franse, and A. A. Menovsky, "Hall-effect and resistivity study of the heavy-fermion system URu_2Si_2", Phys. Rev. B **35**, 5375–5378 (1987).

[40] Y. S. Oh, K. H. Kim, P. A. Sharma, N. Harrison, H. Amitsuka, and J. A. Mydosh, "Interplay between Fermi Surface Topology and Ordering in URu_2Si_2 Revealed through Abrupt Hall Coefficient Changes in Strong Magnetic Fields", Phys. Rev. Lett. **98**, 016401 (2007).

[41] Y. Kasahara, T. Iwasawa, H. Shishido, T. Shibauchi, K. Behnia, Y. Haga, T. D. Matsuda, Y. Onuki, M. Sigrist, and Y. Matsuda, "Exotic Superconducting Properties in the Electron-Hole-Compensated Heavy-Fermion "Semimetal" URu_2Si_2", Phys. Rev. Lett. **99**, 116402 (2007).

[42] M. M. Altarawneh, N. Harrison, S. E. Sebastian, L. Balicas, P. H. Tobash, J. D. Thompson, F. Ronning, and E. D. Bauer, "Sequential Spin Polarization of the Fermi Surface Pockets in URu_2Si_2 and Its Implications for the Hidden Order", Phys. Rev. Lett. **106**, 146403 (2011).

[43] A. F. Santander-Syro, M. Klein, F. L. Boariu, A. Nuber, P. Lejay, and F. Reinert, “Fermi-surface instability at the ‘hidden-order’ transition of URu_2Si_2”, Nat. Phys. **5**, 637 (2009).

[44] C. Bareille, F. L. Boariu, H. Schwab, P. Lejay, F. Reinert, and A. F. Santander-Syro, “Momentum-resolved hidden-order gap reveals symmetry breaking and origin of entropy loss in URu_2Si_2”, Nat. Commun. **5**, 637 (2009).

[45] J. S. Hall, U. Nagel, T. Uleksin, T. Rõõm, T. Williams, G. Luke, and T. Timusk, “Observation of multiple-gap structure in hidden order state of URu_2Si_2 from optical conductivity”, Phys. Rev. B **86**, 035132 (2012).

[46] R. P. S. M. Lobo, J. Buhot, M. A. Méasson, D. Aoki, G. Lapertot, P. Lejay, and C. C. Homes, “Optical conductivity of URu_2Si_2 in the Kondo liquid and hidden-order phases”, Phys. Rev. B **92**, 045129 (2015).

[47] A. R. Schmidt, M. H. Hamidian, P. Wahl, F. Meier, A. V. Balatsky, J. D. Garrett, T. J. Williams, G. M. Luke, and J. C. Davis, “Imaging the Fano lattice to ‘hidden order’ transition in URu_2Si_2”, Nature **465**, 570 (2010).

[48] P. Aynajian, E. H. da Silva Neto, C. V. Parker, Y. Huang, A. Pasupathy, J. Mydosh, and A. Yazdani, “Visualizing the formation of the Kondo lattice and the hidden order in URu_2Si_2”, Proc. Natl. Acad. Sci. **107**, 10383–10388 (2010).

[49] M. Nakashima, H. Ohkuni, Y. Inada, R. Settai, Y. Haga, E. Yamamoto, and Y. Onuki, “The de Haas-van Alphen effect in URu_2Si_2 under pressure”, J. of Phys.: Condens. Matter **15**, S2011 (2003).

[50] E. Hassinger, G. Knebel, T. D. Matsuda, D. Aoki, V. Taufour, and J. Flouquet, “Similarity of the Fermi Surface in the Hidden Order State and in the Antiferromagnetic State of URu_2Si_2”, Phys. Rev. Lett. **105**, 216409 (2010).

[51] A. Villaume, F. Bourdarot, E. Hassinger, S. Raymond, V. Taufour, D. Aoki, and J. Flouquet, “Signature of hidden order in heavy fermion superconductor URu_2Si_2: Resonance at the wave vector $Q_0 = (1,0,0)$”, Phys. Rev. B **78**, 012504 (2008).

[52] N. Kanchanavatee, B. White, V. Burnett, and M. Maple, “Enhancement of the hidden order/large moment antiferromagnetic transition temperature in the $URu_{2-x}Os_xSi_2$ system”, Philos. Mag. **94**, 3681–3690 (2014).

[53] N. Tateiwa, T. D. Matsuda, Y. Ōnuki, Y. Haga, and Z. Fisk, “Strong correlation between anomalous quasiparticle scattering and unconventional superconductivity in the hidden-order phase of URu_2Si_2”, Phys. Rev. B **85**, 054516 (2012).

[54] N. H. Andersen and H. Smith, “Electron-magnon interaction and the electrical resistivity of Tb”, Phys. Rev. B **19**, 384–387 (1979).

[55] N. Hessel Andersen, in *Crystalline Electric Field and Structural Effects in f-Electron Systems*, edited by J. E. Crow, R. P. Guertin, and T. W. Mihalisin (Plenum, New York, 1980), p. 373.

[56] F. Bourdarot, E. Hassinger, S. Raymond, D. Aoki, V. Taufour, L.-P. Regnault, and J. Flouquet, “Precise Study of the Resonance at Q_0=(1,0,0) in URu_2Si_2”, J. Phys. Soc. Jpn. **79**, 064719 (2010).

[57] C. R. Wiebe, J. A. Janik, G. J. MacDougall, G. M. Luke, J. D. Garrett, H. D. Zhou, Y.-J. Jo, L. Balicas, Y. Qiu, J. R. D. Copley, Z. Yamani, and W. J. L. Buyers, “Gapped itinerant spin excitations account for missing entropy in the hidden-order state of URu_2Si_2”, Nat. Phys **3**, 96 (2007).

[58] C. Broholm, H. Lin, P. T. Matthews, T. E. Mason, W. J. L. Buyers, M. F. Collins, A. A. Menovsky, J. A. Mydosh, and J. K. Kjems, “Magnetic excitations in the heavy-fermion superconductor URu_2Si_2”, Phys. Rev. B **43**, 12809–12822 (1991).

[59] F. Bourdarot, A. Bombardi, P. Burlet, M. Enderle, J. Flouquet, P. Lejay, N. Kernavanois, V. Mineev, L. Paolasini, M. Zhitomirsky, and B. Fåk, “Hidden order in URu_2Si_2”, Physica B **359-361**, 986 (2005).

[60] F. Bourdarot, S. Raymond, and L.-P. Regnault, “Neutron scattering studies on URu_2Si_2”, Philos. Mag. **94**, 3702–3722 (2014).

[61] K. Kuwahara, H. Sagayama, K. Iwasa, M. Kohgi, S. Miyazaki, J. Nozaki, J. Nogami, M. Yokoyama, H. Amitsuka, H. Nakao, and Y. Murakami, “High pressure X-ray diffraction study of URu_2Si_2”, Acta Phys. Pol. B **34**, 4307 (2003).

Chapter 7

Pressure effects in the itinerant antiferromagnetic metal TiAu

7.1 Introduction

There are relatively few examples of materials that approximate a purely itinerant (or delocalized) electron magnet. Only the delocalized $3d$-electron bands of the transition metal elements have the requisite energy bandwidth W and wavevector magnitude k, that can create a large density of states (DOS) at the Fermi energy ε_F, that is unstable to the formation of a magnetically ordered ground state. The few transition metal materials that approach the extreme case of pure itinerant electron magnets include the weak itinerant ferromagnets (IFMs) $ZrZn_2$ [1] and Sc_3In [2] and the recently discovered weak itinerant antiferromagnet (IAFM) TiAu. [3]

It is expected that significant effects are to be observed in the magnetic properties of weak IFMs under the application of pressure.[4–6] The application of pressure usually results in a reduction in magnetic order owing to a broadening of the electron bands and an associated decrease in the DOS(ε_F). This reduction in the DOS(ε_F) often dominates the expected increase in magnetization that results from an enhancement of the exchange interaction J as pressure is increased. [6, 7] In the weak IFM $ZrZn_2$, the Curie temperature $T_C \sim 25$ K at ambient pressure is suppressed rapidly to $T_C = 0$ K toward a quantum critical point (QCP) at a modest critical pressure of $P_c = 0.85$ GPa. [8–10] However, it has been shown that the application of pressure can stabilize the band magnetism over a certain range of pressure as observed in the anomalous behavior for the weak IFM Sc_3In, in which the magnetic ordering temperature is enhanced with the application of hydrostatic pressure up to $P \sim 3$ GPa.[7, 11]

In this report, we explore the effect of pressure on the Néel temperature T_N, in the IAFM TiAu, as a follow up to the recent study on the suppression of T_N with chemical doping in the $Ti_{1-x}Sc_xAu$ system toward a QCP. [12] The initial report on the synthesis and characterization of polycrystalline samples of phase-pure, orthorhombic TiAu indicates that the intermetallic compound behaves as an IAFM with an ambient pressure Néel temperature $T_N = 36$ K. [3] Neutron diffraction measurements revealed a magnetic peak at the $\mathbf{Q} = (0, \pi/b, 0)$ modulation vector well below T_N, with an estimated magnetic moment of 0.15 μ_B per formula unit (compared to the relatively large paramagnetic (PM) moment above T_N of $\mu_{PM} \simeq 0.8$ μ_B per formula unit as derived from the linear fit of the high-temperature inverse susceptibility *vs* temperature). In addition, muon spin relaxation (μSR) measurements revealed the existence of strong spin fluctuations in the PM phase above $T_N \simeq 35$ K, which quickly vanish throughout the sample volume over a small temperature range (~ 5 K) at the transition temperature.[3]

Upon substitution of trivalent Sc^{3+} ions for Ti^{4+} ions, there is a rapid and monotonic suppression of the Néel temperature for the $Ti_{1-x}Sc_xAu$ system from $T_N = 36$ K at $x = 0$ toward a two-dimensional (2D) AFM QCP at a critical concentration of $x_c = 0.13$. [12] The quantum phase transition to a two-dimensional antiferromagnet is reflected in both the linear temperature dependence of the electrical resistivity and the logarithmic divergence with decreasing temperature of the specific heat divided by temperature close to the QCP. [12]

In the present study, the pressure dependence of T_N was determined from measurements of electrical resistivity ρ, for several polycrystalline samples of TiAu as performed in various pressure cells over a range in pressure from $P = 0$ to 27 GPa. The features observed in the measurements of $\rho(T,P)$ allowed us to track the evolution of the Néel temperature T_N as a function of pressure, P. In contrast to the $T(x)$ dependence, we initially observe a positive pressure coefficient $dT_N/dP > 0$ at low pressure up to a maximum in T_N at $P \sim 5.5$ GPa which is followed by a monotonic suppression of T_N with a further increase in pressure. The temperature dependence of the electrical resistivity was determined from power law fits of the electrical resistivity $\rho = \rho_0 + A_n T^n$ to the $\rho(T)$ data above and below T_N. During the enhancement of T_N at low pressure ($P \leq 5.5$ GPa), $\rho(T)$ exhibits a T^3 temperature dependence in the antiferromagnetic phase. Interestingly, there is an abrupt change in the temperature dependence of $\rho(T)$ from T^3 to T^2 that is coincident with the peak in the $T_N(P)$ phase boundary at $P \sim 5.5$ GPa. As pressure is increased beyond 6 GPa and T_N is suppressed down to 22 K, $\rho(T)$ continues to exhibit a T^2 dependence up to $P \sim 25$ GPa. At this pressure, the anomalous drop in $\rho(T)$ is no longer detectable and $\rho(T)$ returns to a nearly T^3 behavior.

7.2 Experimental Details

Polycrystalline samples of TiAu were prepared by arcmelting Au and Ti as described previously in Ref. [3]. The measurements of electrical resistance R under pressure were performed for 5 different samples of TiAu in one of three types of pressure cells: (1) a piston cylinder cell (PCC), (2) a Bridgman anvil cell (BAC), and (3) a designer diamond anvil cell (DAC). The polycrystalline sample of TiAu (sample 0) measured in the PCC and

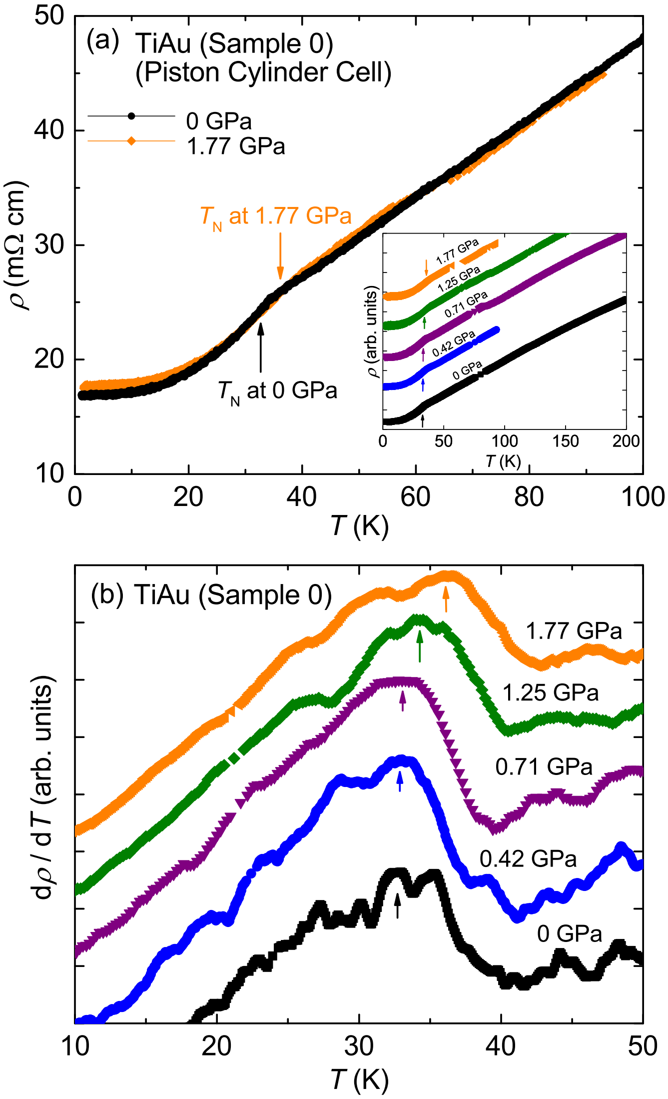

Figure 7.1: (a) Electrical resistivity ρ *vs* temperature T at $P = 0$ and 1.8 GPa as measured in a piston cylinder cell (PCC). The arrows indicate the features in ρ that correspond to values of $T_N = 32.7$ K and 35.5 K at $P = 0$ and 1.77 GPa, respectively. Inset: Electrical resistivity ρ *vs* T up to $T = 200$ K at various pressures up to $P = 1.8$ GPa displaying the nearly linear temperature dependence and metallic behavior of ρ in the PM phase. The ρ *vs* T curves have been shifted vertically for clarity in illustrating the increase in T_N with increasing pressure. (b) The temperature derivative of the electrical resistivity $\mathrm{d}\rho/\mathrm{d}T$ *vs* temperature T at various pressures (shifted vertically for clarity). The Néel temperature at each pressure was determined from the maximum in $\mathrm{d}\rho/\mathrm{d}T$ as indicated by the arrows and the values of T_N are listed in Table 7.1.

Table 7.1: The values of the Néel temperature T_N, at pressure P, for the TiAu Samples 0, 1, 2, 3, and 4 measured in the various pressure cells.

TiAu Sample 0		TiAu Sample 1		TiAu Sample 2		TiAu Sample 3		TiAu Sample 4	
P (GPa)	T_N (K)	P (GPa)	T_N (K)	P (GPa)	T_N (K)	P (GPa)	T_N (K)	P (GPa)	T_N (K)
0	32.7	2.2	33.1	2.7	31.7	2.7	31.7	2.2	30.7
0.42	32.9	3.7	34.7	5.4	32.7	5.4	32.3	5.0	32.2
0.71	33.1	5.8	35.2	12.7	28.9	7.3	31.9	9.7	28.5
1.25	34.2	6.2	33.2	13.4	28.8	12.7	29.0	15.0	25.9
1.77	35.5			14.3	26.9	13.4	28.6	18.1	24.7
				14.8	26.8			26.7	22.1
				16.3	26.5				

the polycrystalline sample of TiAu (sample 1) measured in the first BAC are from the same synthesis performed at Rice University, while polycrystalline samples of TiAu (samples 2 and 3) measured simultaneously in the second BAC along with the polycrystalline sample of TiAu (sample 4) measured in the DAC are from a second synthesis performed at Rice University. While the geometrical factor for TiAu sample 0 measured in the PCC was easily determined, we note that the geometical factor of the TiAu samples measured in the BACs and the DAC was too uncertain to yield a reasonable determination of the electrical resistivity ρ. Hence, we are only able to report the scaled electrical resistivity $\rho/\rho_{300\mathrm{K}}$, for the samples measured in the two BACs and the DAC, where ρ_{300K} is the value of electrical resistivity measured at 300 K.

In order to minimize the contact resistance for the sample measured in the PCC, a standard four-wire electrical resistivity measurement technique was used in which platinum wire leads were attached to the surface of the sample with two-part silver epoxy. The measurements of ρ in the PCC were performed at pressures ranging from ambient pressure ($P \sim 0$ GPa) up to a pressure $P \sim 1.8$ GPa in an equal parts by volume mixture of n-pentane and isoamyl alcohol as a pressure-transmitting medium. The load was applied to the PCC at room temperature ($T \sim 300$ K) which is much higher than the melting point of the pressure-transmitting medium ($T \sim 120$ K) to ensure a nearly hydrostatic pressure environment. The pressure in the PCC at low temperature ($T < 4$ K) was determined by an inductive measurement of the superconducting transition temperature T_c, of high-purity Sn (99.999%) and then compared with the established pressure dependence of T_c for Sn. [13]

The measurements of electrical resistance R, for three different samples (TiAu samples 1, 2, 3) in two different BACs were performed at pressures ranging from $P \sim 2.5$ to 16 GPa. TiAu sample 1 was measured independently in a BAC and TiAu samples 2 and 3 were measured together in a second BAC. The pressure dependent measurements of

R in the BACs were made by using nonmagnetic tungsten carbide anvils to compress the sample in solid steatite used as a quasi-hydrostatic pressure-transmitting medium. Electrical resistance R was measured in a four-wire configuration in which electrical contact between the platinum leads and the surface of the TiAu samples was made by applying pressure with the tungsten carbide anvils. The pressure in the BAC was based on a four-wire electrical resistance measurement of T_c of a Pb sample placed inside the pressure cell which was compared with the established pressure dependence of the superconducting transition ($T_c(P)$) for Pb in the literature.[13]

The measurements of R in the designer diamond anvil cell (DAC) were also performed using solid steatite as a quasi-hydrostatic pressure-transmitting medium for pressures ranging from $P \sim 2$ to 27 GPa. The designer DAC consisted of a 6-probe designer diamond anvil with a 250-μm culet that was paired with a standard diamond anvil with a slightly larger sized culet of 300 μm. A thin shard of polycrystalline TiAu was positioned on the culet of the 6-probe designer diamond in order to make contact with the tungsten pads connected to the electrical probes. The sample space between the two culets, which contains the polycrystalline sample of TiAu, the solid steatite pressure-transmitting medium, and the ruby spheres used as manometers was sealed within a 100-μm hole that was drilled into the center of the indentation of a non-magnetic gasket made of MP35N, an age-hardened Nickel-Cobalt base alloy. [14] The gasket was pre-indented to a thickness of $\sim$ 40-μm and the hole was drilled into the gasket with an electric discharge machine (EDM). The pressure in the DAC was determined by tracking the shift in the R1 fluorescence line of the ruby spheres as pressure was increased at room temperature. [15, 16] At low pressure, the R1 line was measured for two different ruby chips on opposing parts of the culet to rule out the presence of large gradients in pressure across the sample space. During the four-wire measurements of electrical resistance in each pressure cell, excitation currents were consistently set to be at 1 mA using an LR-700 Linear Research ac resistance bridge.

7.3 Results and Discussion

Electrical resistivity measurements under pressure

The temperature dependence of the electrical resistivity $\rho(T)$ for TiAu as measured in the piston cylinder cell (PCC) at P = 0 and 1.8 GPa is shown in Fig. 7.1 (a). At lower temperatures (for $T < 40$ K), there is a distinct feature or characteristic drop in the $\rho(T)$ data at T_N (as indicated by the vertical arrows), which is typical of a phase transition from a spin-disordered PM phase above T_N to a spin-ordered AFM phase below T_N. Typical metallic behavior with a positive temperature coefficient ($\mathrm{d}\rho/\mathrm{d}T > 0$) and a nearly linear temperature dependence is apparent in the $\rho(T)$ data for $T > 40$ K. Based on μSR measurements, the spin disorder in the PM phase is characterized by strong spin fluctuations that rapidly decay at the onset of the AFM order. [3] It is worth mentioning that in the IAFM TiAu, there is no gapping of the Fermi surface during the AFM transition. The abrupt decrease observed in the $\rho(T)$ data with decreasing temperature through T_N most likely reflects the disappearance of the short-range spin fluctuations during the phase transition from the PM phase to the AFM phase. This is in contrast to the anomalous jump in ρ, for example, as observed in elemental Cr just below $T_N \simeq 311$ K at which point the formation of a gap over the Fermi surface results in a reduction in the carrier concentration and is associated with the emergence of an incommensurate long-range AFM spin fluctuation. [17]

In order to illustrate the increase in T_N with increasing pressure, the $\rho(T)$ curves at various pressures up to P = 1.8 GPa have been shifted vertically for clarity as shown in the inset of Fig. 7.1 (a). Notice that the AFM ordering temperature increases monotonically with increasing pressure up to $P \sim 1.8$ GPa, as measured in the PCC such that T_N = 32.7,

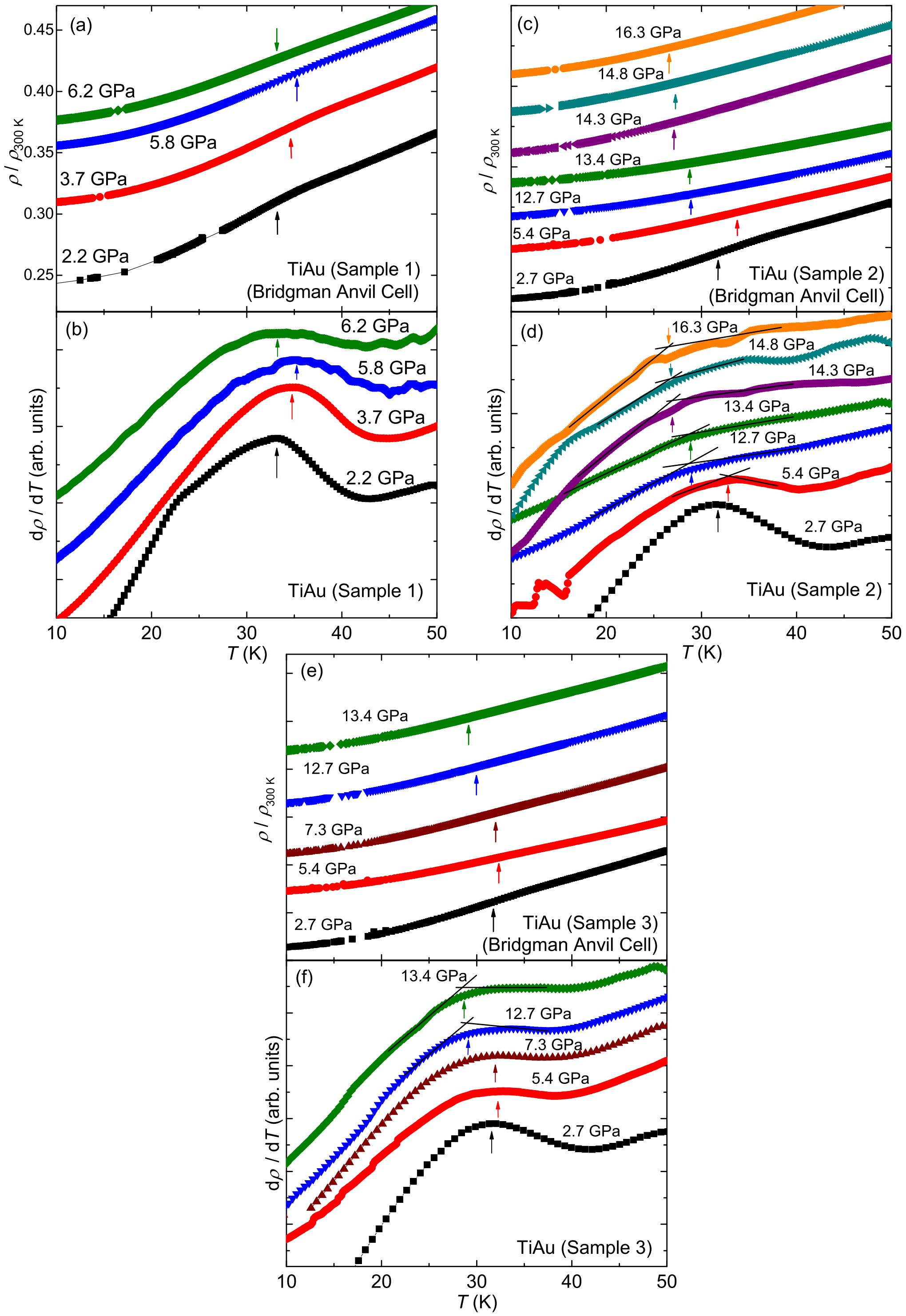

Figure 7.2: Electrical resistivity $\rho/\rho_{300\mathrm{K}}$ (a, c, e) and $\mathrm{d}\rho/\mathrm{d}T$ (b, d, f) for TiAu samples 1, 2, and 3 at various P. The arrows point to the location of T_N occuring at the maximum in $\mathrm{d}\rho/\mathrm{d}T$ or the intersection of the linear extrapolations (solid black lines) of the $\mathrm{d}\rho/\mathrm{d}T$ *vs* T curves. The values of T_N at various P for TiAu samples 1, 2, and 3 are shown in Table 7.1.

32.9, 33.0, 34.2, and 35.5 K at P = 0, 0.42, 0.71, 1.25, and 1.77 GPa, respectively, at a rate of dT_N/dP = 1.64 K GPa^{-1}. As shown in Fig. 7.1 (b), there are clear maxima observed in the the temperature derivative of the electrical resistivity dρ/dT at low pressures up to $P \sim 2$ GPa and the values of the AFM ordering temperature T_N, were easily resolved and determined from locating the maximum in dρ/dT.

At ambient pressure, the shape of the peak in the dρ/dT *vs* T curve (black data at P = 0 GPa in Fig. 7.1 (b)) is similar to the peak in the dρ/dT *vs* T previously reported in Ref. [3]. The maximum in the dρ/dT *vs* T curve at ambient pressure is reminiscent of the small peak at T_N observed in the specific heat (C_p/T *vs* T) also reported in Ref. [3]. Based on the analysis from previous studies of the specific heat curves for second order transitions associated with (anti-)ferromagnetic materials, [18, 19] it is clear from the C_p/T *vs* T curve in Ref. [3] that a subtraction of the non-magnetic contributions to the specific heat, i.e., the lattice and electronic contributions, would yield a magnetic contribution to the specific heat C_m, with a peak similar to that observed in the ambient pressure dρ/dT *vs* T curve. This correspondence between the peak-like curve of dρ/dT *vs* T and the peak-like behavior of the magnetic specific heat (represented by the shaded gray region in Fig. 2 of Ref. [3]) is consistent with a second order phase transition in a system in which short-range spin fluctuations are the dominant contribution to the magnetic resistivity ρ_{mag}, in an itinerant-electron system. [20]

It is important to note that at low pressures ($P < 2$ GPa), the width of the peak in dρ/dT is already showing signs of broadening as pressure is increased. As discussed below, this becomes problematic in determining the exact value of T_N at higher pressures above $P \sim 6$ GPa.

Figure 7.2 displays the temperature dependence of the electrical resistivity $\rho/\rho_{300\text{K}}$, in the vicinity of T_N for three different polycrystalline samples of TiAu under pressure, as measured in two different BACs. The electrical resistance $R(T)$ for TiAu polycrystalline sample 1, was measured independently in a BAC up to $P \sim 6$ GPa and is displayed as $\rho/\rho_{300\mathrm{K}}$ in Fig. 7.2 (a). The characteristic drop in ρ that occurs at T_N, as indicated by the vertical arrows, becomes less pronounced with increasing pressure. However, the values of T_N were easily determined from the location of the maxima in the temperature derivative of electrical resistivity ($\mathrm{d}\rho/\mathrm{d}T$) as shown in Fig. 7.2 (b). The AFM ordering temperature is enhanced with increasing pressure from T_N = 33.1 K at P = 2.2 GPa up to a maximum of T_N = 35.2 K at P = 5.8 GPa at a rate of $\mathrm{d}T_N/\mathrm{d}P$ = 0.55 K GPa^{-1}, after which there is a decline to T_N = 33.1 K at P = 6.2 GPa. It should be mentioned that for the $\rho(T)$ data at 2.2 GPa only, there are regions of missing data below 27 K. In order to generate the continuous temperature derivative of the electrical resistivity at 2.2 GPa ($\mathrm{d}\rho/\mathrm{d}T$ *vs* T) as shown in Fig. 7.2 (b), some amount of interpolation and smoothing was required in performing the differentiation of the raw data. However, owing to the sufficient amount of data in the vicinity of T_N = 33.1 K, the effect of interpolation and smoothing on the location of the maximum $\mathrm{d}\rho/\mathrm{d}T$ were well within the error in determining T_N.

A similar trend in the behavior of T_N with increasing applied pressure is observed in the electrical resistivity $\rho/\rho_{300\mathrm{K}}$, for both polycrystalline TiAu samples 2 and 3 as displayed in Fig. 7.2 (a) and (e), respectively. (TiAu samples 2 and 3 were measured simultaneously in a second BAC that was distinct from the BAC used to measure TiAu sample 1.) As observed in the case for TiAu sample 1, the characteristic drop in ρ at T_N (marked by the vertical arrows) is difficult to resolve in the $\rho(T)$ data at pressures above P = 5 GPa, as displayed in Fig. 7.2 (c) and (e). When possible, the location of the maximum in $\mathrm{d}\rho/\mathrm{d}T$ was used to determine the value of T_N as marked by the arrows in the $\mathrm{d}\rho/\mathrm{d}T$ *vs* T plots (Fig. 7.2 (d) and (f)). Arrows indicating the location of T_N are also shown in the plots of $\rho/\rho_{300\mathrm{K}}$ *vs* T (Fig. 7.2 (c) and (e)). Clear maxima are observed in $\mathrm{d}\rho/\mathrm{d}T$ up to $P \sim 5.5$ and 7.5 GPa for samples 2 and 3, respectively, as shown in Fig. 7.2 (d) and (f). However, at higher values of pressure, it was necessary to determine T_N from a different procedure

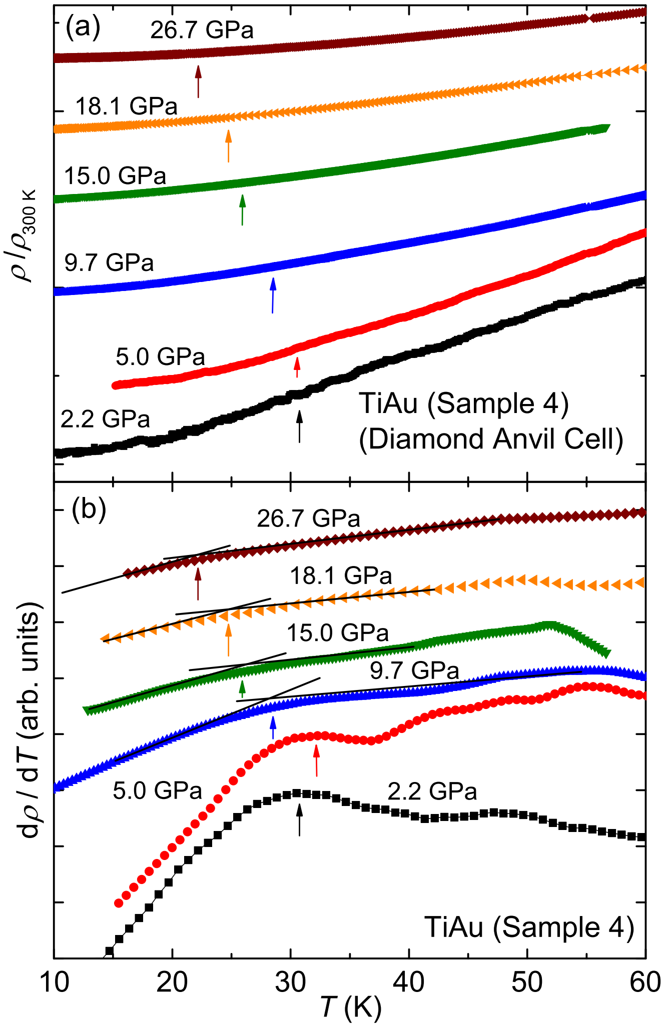

Figure 7.3: (a) Electrical resistivity $\rho/\rho_{300\mathrm{K}}$ *vs* temperature T in the vicinity of the AFM ordering temperature T_N at various pressures up to $P \sim 27$ GPa as measured in a diamond anvil cell (DAC). The arrows point to the features at T_N. (b) Temperature derivative of the electrical resistivity $\mathrm{d}\rho/\mathrm{d}T$ *vs* T. The values of T_N = 30.7 and 32.2 K at P = 2.2 and 5.0 GPa respectively were determined from the maximum in the $\mathrm{d}\rho/\mathrm{d}T$ *vs* T curves whereas the values of T_N = 28.5, 25.9, 24.7, 22.1 K at P = 9.7, 15.0, 18.1, 26.7 GPa, respectively, were determined from the intersection of the linear extrapolations (solid black lines) of the $\mathrm{d}\rho/\mathrm{d}T$ *vs* T curves as shown in panel (b).

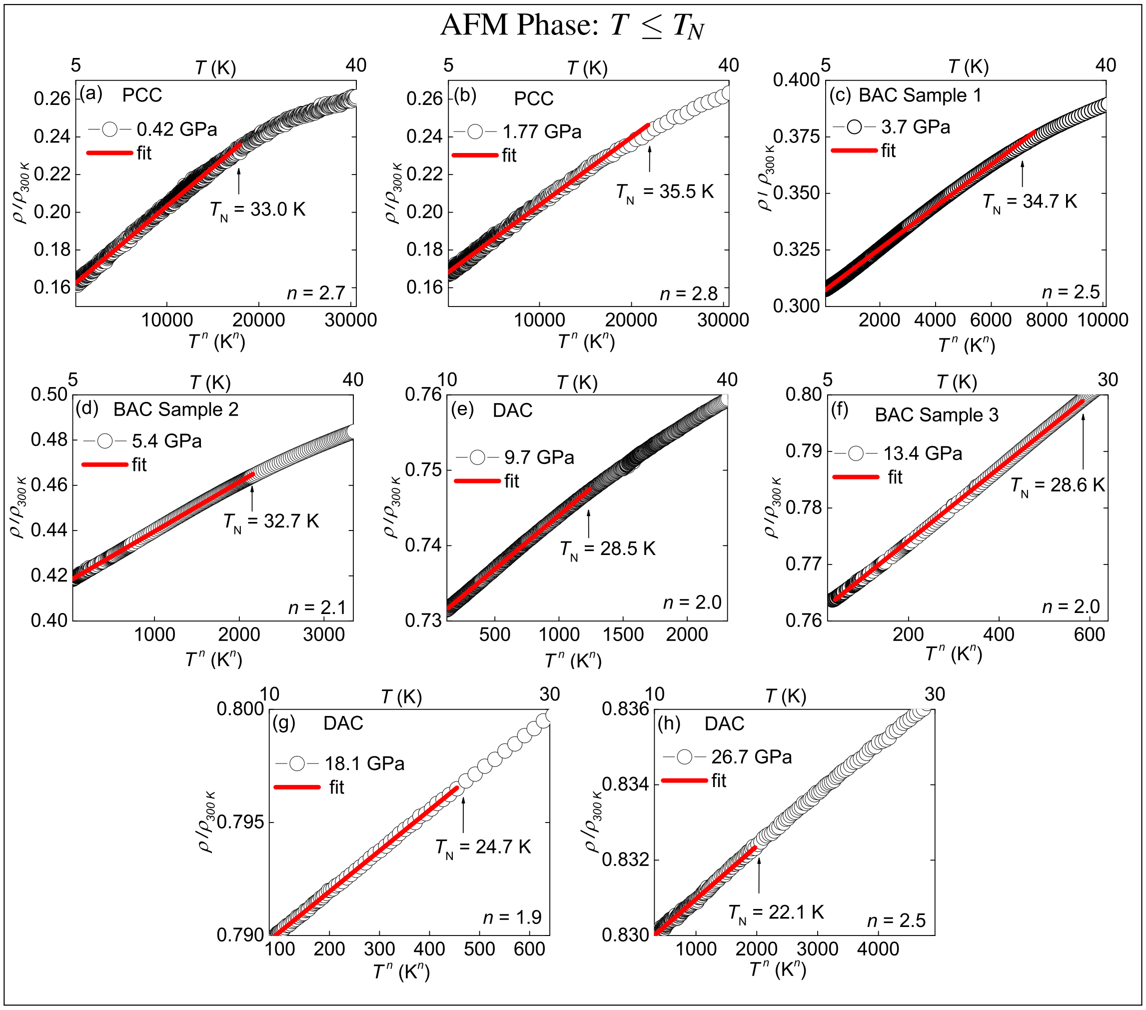

Figure 7.4: Scaled electrical resistivity $\rho/\rho_{300\text{K}}$ *vs* T^n above and below the Néel temperature T_N for TiAu under pressure, P. Power law fits of the electrical resistivity, $\rho = \rho_0 + A_n T^n$ to the $\rho(T)$ data were performed for $T < T_N$ in the AFM phase. The upper x-axis in each plot is shown as a linear T scale and T_N is indicated by the black vertical arrows.

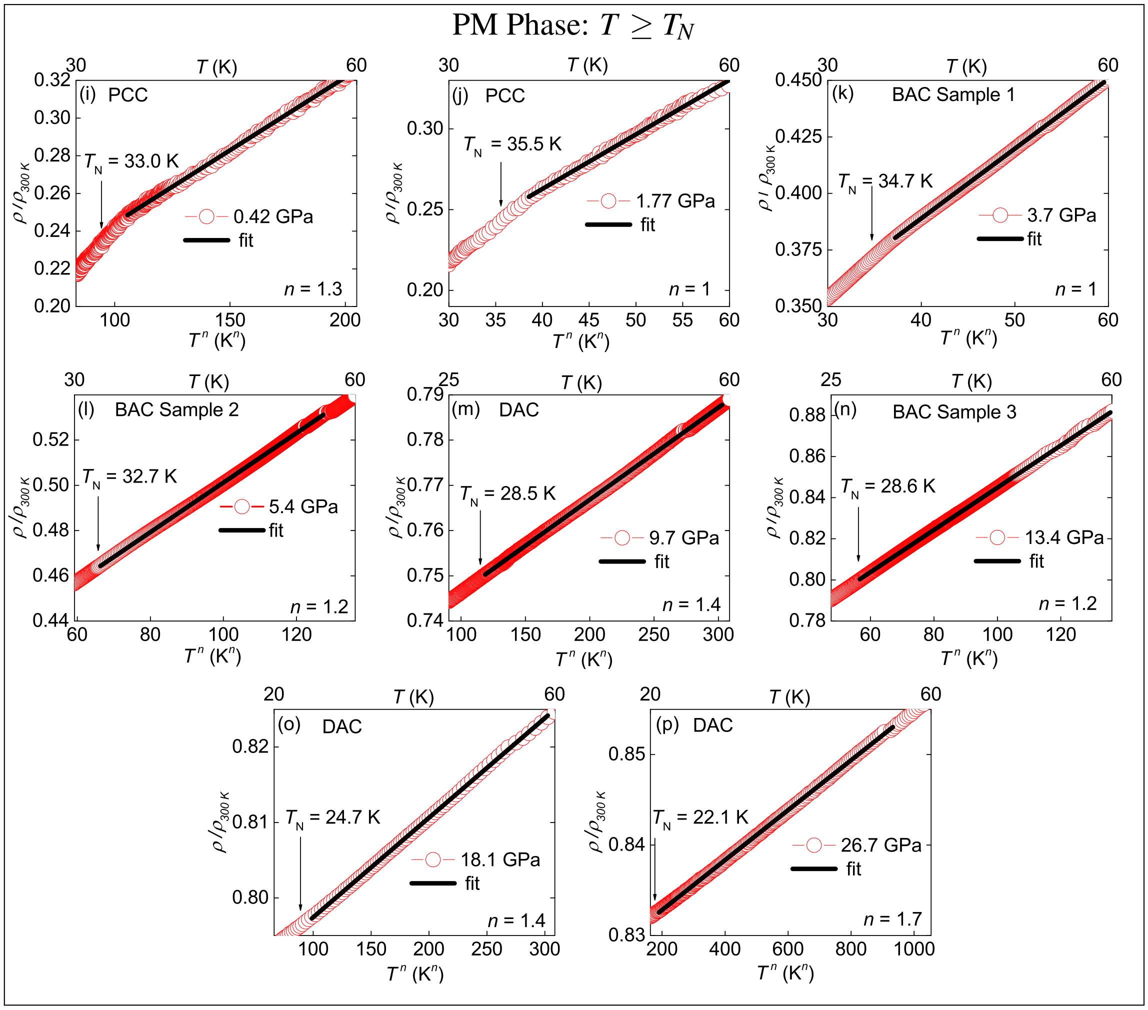

Figure 7.5: Scaled electrical resistivity $\rho/\rho_{300\text{K}}$ *vs* T^n above and below the Néel temperature T_N for TiAu under pressure, P. Power law fits of the electrical resistivity, $\rho = \rho_0 + A_n T^n$ to the $\rho(T)$ data were performed for $T > T_N$ in the PM phase. The upper x-axis in each plot is shown as a linear T scale and T_N is indicated by the black vertical arrows.

by which T_N was defined to be the intersection of the linear extrapolations of the dρ/dT curves above and below T_N as indicated by the black lines in Fig. 7.2 (d) and (f). At P = 2.7 GPa, both TiAu samples 2 and 3 appear to undergo the transition into the AFM phase at T_N = 31.7 K. The ordering temperature increases with further application of pressure at a rate of dT_N/dP = 0.30 K GPa^{-1} to a maximum value of $T_N \sim$ 32.5 K at $P \sim$ 5.5 GPa.

The values of the AFM ordering temperature T_N, are nearly identical for samples 2 and 3 up to P = 13.4 GPa. However, at lower pressures up to $P \sim$ 6 GPa the values of T_N are somewhat smaller than the values of T_N that were observed for TiAu sample 1 measured in the BAC which reaches a maximum of T_N = 35.2 K at P = 5.8 GPa. Nevertheless, the pressure dependence of T_N for all three samples measured in the two BACs is qualitatively consistent, in which T_N initially increases with pressure and passes through a maximum at $P \sim$ 5.5. There is a large and monotonic suppression of the AFM order with a further increase in applied pressure such that T_N is reduced to $T_N \sim$ 26 K at $P \sim$ 16 GPa. The suppression of AFM order can be seen in the shift of the intersection of the linear extrapolations (or "knee") in the dρ/dT *vs* T curves as shown in Figs. 7.2 (d) and (f). (We mention that the absence of $\rho(T)$ data at higher pressures for sample 1 ($P >$ 6.2 GPa) and sample 3 ($P >$ 13.4 GPa) was due to failure of the electrical leads in the high pressure Bridgman anvil cell.)

Measurements of electrical resistance under pressure $R(P,T)$, were extended to higher pressures up to $P \sim$ 27 GPa with the use of a designer diamond anvil cell (DAC). The temperature dependence of the scaled electrical resistivity $\rho/\rho_{300\mathrm{K}}$ in the neighborhood of T_N at various pressures from P = 2.2 to 26.7 GPa are displayed in Fig. 7.3. The characteristic drop in ρ at the AFM transition at T_N = 31.6 K is just detectable in the $\rho(T)$ curves at P = 2.2 and 5.0 GPa; each of these $\rho(T)$ curves exhibits a clear maximum observed in their temperature derivatives (dρ/dT) as shown in Fig. 7.3 (b). The AFM ordering temperature for $P >$ 5.0 GPa, as measured in the DAC, was defined to be the

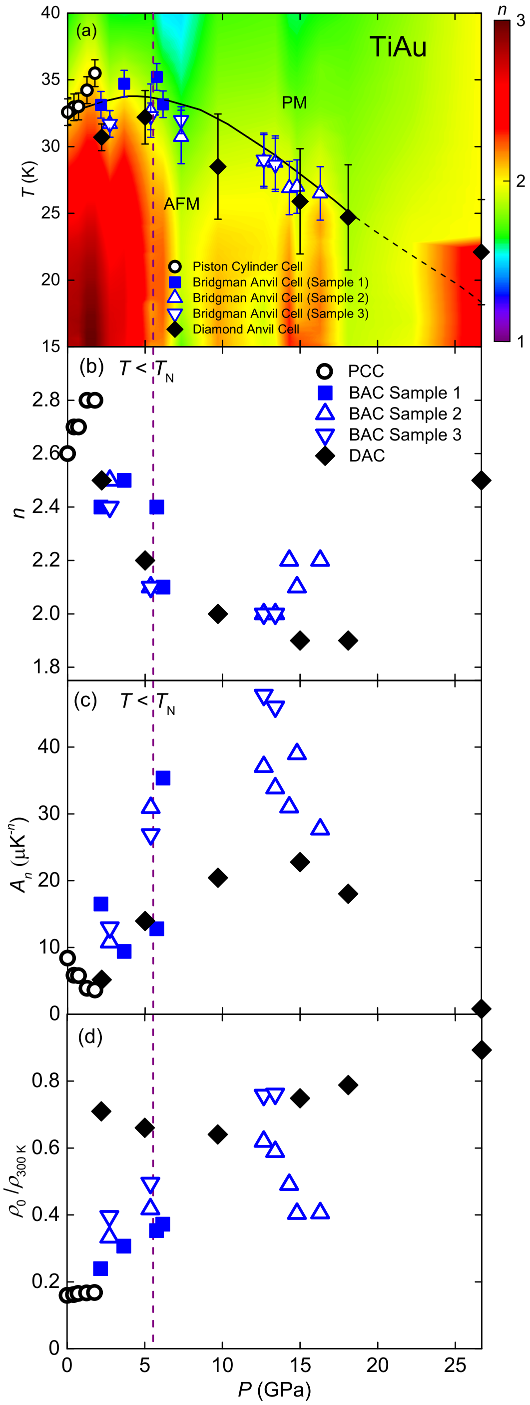

Figure 7.6: (a) Temperature *vs* pressure (T_N *vs* P) phase diagram superimposed on a color contour representation of the exponent $n(P,T)$ from the electrical resistivity: $\rho = \rho_0 + A_n T^n$ (see text). The solid black curve is a guide to the eye and denotes the $T_N(P)$ phase boundary. (b, c, d) The parameters n, A_n, and ρ_0 *vs* pressure P were extracted from power law fits of the electrical resistivity in the AFM phase as shown in Fig. 7.4. The dashed vertical line at $P = 5.5$ GPa is a guide to the crossover at the peak in $T_N(P)$.

temperature at the intersection of the linear extrapolations (solid black lines) of the $\mathrm{d}\rho/\mathrm{d}T$ curves above and below T_N as shown in panel (b) of Fig. 7.3. (This method is similar to the determination of the values of T_N at higher pressures for TiAu samples 2 and 3.) The Néel temperature increases from T_N = 30.7 K at $P \sim 2.2$ GPa to 32.2 K at $P \sim 5.0$ GPa. As pressure is increased further, the AFM order is suppressed to T_N = 22.1 K at $P \sim 27$ GPa at a rate of approximately $\mathrm{d}T_N/\mathrm{d}P = -\ 0.48$ K GPa^{-1}.

The temperature dependence of the electrical resistivity $\rho = \rho_0 + A_n T^n$, in the neighborhood of T_N, is displayed in Fig. 7.4 and Fig. 7.5 as a series of power law fits to the $\rho(P,T)$ data for TiAu under pressure. The eight panels in Fig. 7.4 are fits to the data in the AFM phase ($T < T_N$) at selected pressures from the various pressure cells while the eight panels in Fig. 7.5 are fits to the data in the PM phase ($T > T_N$). A nearly linear temperature dependence describes the data above T_N in the PM phase up to 60 K for $P <$ 5.4 GPa and a slightly larger power law exponent of $n = 1.4$ to 1.7 describes the $\rho(T)$ data in the PM phase at higher pressures for $P = 10$ to 27 GPa. Below the Néel temperature in the AFM phase (5 K $< T < T_N$), the $\rho(T)$ behavior is described by a much higher exponent of $n = 2.8$ for low pressures up to $P \sim 2$ GPa. As pressure is increased slightly, the value of the power law exponent approaches $n \sim 2$ as the pressure approaches $P \sim$ 6 GPa. The $n = 2$ dependence remains as pressure is increased up to $P \sim 25$ GPa. It is interesting to note that the clear crossover to a T^2 dependence in the AFM phase is coincident with the peak in the $T_N(P)$ phase boundary at $P \sim 5.5$ GPa. In the PM phase, the temperature dependence is somewhat stagnant but perhaps showing a slight increase from a linear temperature dependence toward a $T^{1.5}$ dependence as pressure is increased and T_N is reduced. The onset of T^2 behavior during the suppression of T_N for $P > 6$ GPa suggests there may be a crossover to a Fermi-liquid ground state in this pressure range. However, these power law exponents are also consistent with the behavior of local moment (and also itinerant) AFM metals near T_N as described by self-consistent renormalization (SCR) theory, in which spin fluctuations account for most of the scattering that can lead to a A_nT^n ($n \sim 2$) term in the power law behavior of the electrical resistivity. [21]

The effect of applied pressure on antiferromagnetic order in TiAu

As mentioned in the Introduction, it has recently been reported that chemical doping has the effect of suppressing the AFM order in the TiAu metal toward a two-dimensional AFM QCP.[12] Magnetization, specific heat, and electrical resistivity measurements at ambient pressure provide evidence for a continuous suppression of the AFM order in the $\mathrm{Ti}_{1-x}\mathrm{Sc}_x\mathrm{Au}$ system as a function of x up to a critical concentration of x_c = 0.13, at which point the system appears to exhibit a continuous second order quantum phase transition (QPT). [12] The 2D AFM QCP in the $\mathrm{Ti}_{1-x}\mathrm{Sc}_x\mathrm{Au}$ system is supported by the logarithmically divergent electronic specific heat coefficient $\gamma(T)$ and the linear ($n = 1$) temperature dependence of the electrical resistivity ($\rho = \rho_0 + A_nT^n$) in the vicinity of the QCP.[12]

The pressure dependence of T_N as determined from the measurements of $\rho(T)$ for TiAu under pressure in the various pressure cells is summarized in the T_N *vs* P phase diagram as shown in Fig. 7.6 (a). There is a slight enhancement of AFM at low pressure. There is a clear peak in $T_N(P)$ boundary which is followed by a suppression of AFM as pressure is increased up to 27 GPa. (For comparison, the reader is referred to the T_N *vs* x phase diagram for the $\mathrm{Ti}_{1-x}\mathrm{Sc}_x\mathrm{Au}$ system as reported in Ref. [12].) The values of T_N, as determined from measurements of ρ in the PCC, the two BACs and the DAC, collectively indicate that the maximum in T_N occurs at $P \sim 5.5$ GPa. For pressures above $P \sim 6$ GPa, there is a monotonic suppression of the antiferromagnetic order. In particular, the Néel temperature is reduced to $T_N \sim 22$ K at a pressure of $P \sim 27$ GPa as measured in the DAC.

The evolution of T_N with P, in which there is an initial increase in T_N with pressure up to a maximum of ~ 35.5 K at $P \sim 5.5$ GPa, is distinct from the monotonic decrease in T_N observed with increasing x. [12] This contrasting behavior between the evolution of T_N with P and x in $\mathrm{Ti}_{1-x}\mathrm{Sc}_x\mathrm{Au}$ is similar to what was observed for the IFM $\mathrm{Sc}_3\mathrm{In}$, in which the FM ordering temperature T_C, is initially enhanced with increasing P but is monotonically suppressed toward a QCP with increasing x in $(\mathrm{Sc}_{1-x}\mathrm{Lu}_x)_{3.1}\mathrm{In}$.[22] In the $\mathrm{Ti}_{1-x}\mathrm{Sc}_x\mathrm{Au}$ system, band structure calculations reveal that the $3d$-electron bands of the Ti^{4+} ions contribute the most to the sharp peak observed in the DOS(ε_F) that leads to the magnetic ground state.[12] As x increases, and more Sc^{3+} ions replace the Ti^{4+} ions, the peak in the DOS(ε) shifts away from the ε_F leading to a reduction in the magnetic ordering temperature T_N. [12]

On general grounds, the application of pressure should also lead to a suppression of the magnetic ordering temperature in an itinerant magnet in which the $3d$-electron bandwidth is broadened leading to a decrease in the DOS at the Fermi level. [7] There are relatively few examples in the literature in which the application of pressure results in an enhancement of the magnetic ordering temperature. [7, 11, 23–25] In the case of the enhancement of FM order observed in the $\mathrm{Au}_{1-x}\mathrm{V}_x$ system, it was determined that there is an increase in the exchange interaction, J, as pressure is increased. [25] In the present study, there was no determination of the magnitude of J as a function of pressure. However, calculations of the band structure for TiAu under pressure indicate that the magnetic moment decreases monotonically with increasing pressure.[26] This suggests that the initial increase in T_N with pressure up to $P \sim 6$ GPa may result from an increase in J that is dominant over the decrease in the DOS(ε_F).

The distinct behavior observed in the evolution of T_N with increasing P in TiAu when compared with increasing x in the $\mathrm{Ti}_{1-x}\mathrm{Sc}_x\mathrm{Au}$ system may result from the contrasting effects of pressure and doping on the unit cell volume. There is an overall expansion of the unit cell volume of TiAu by 4 % upon substituting Ti with slightly larger Sc ions between $x = 0$ and 0.25 in $\mathrm{Ti}_{1-x}\mathrm{Sc}_x\mathrm{Au}$. Most of the volume increase is due to the increase in the intra-planar lattice parameter b, while the inter-planar spacing (lattice paramater c) remains unaffected with increasing Sc doping. [12, 26] However, it is reasonable to assume that an application of pressure would result in a reduction of the unit cell volume. In particular, under the most hydrostatic environment as observed in the PCC, the unit cell volume of TiAu is more likely to contract isotropically leading to conditions that might favor an enhancement of T_N, namely an increase in the DOS at the Fermi level, or an enhanced exchange interaction J that could result from a contraction along the intra-planar (b) or inter-planar (c) directions. Under a less hydrostatic environment, or as pressure is increased beyond a certain threshold value, the unit cell may contract or deform anisotropically resulting in a monotonic decrease of T_N as suggested by calculations of the band structure under pressure. [26] In particular, a contraction solely along the inter-planar c direction might result in a change to the relative unit cell geometry similar to the relative change observed upon Sc substitution in which there was an increase in the intra-planar lattice parameter b but no change in the inter-planar spacing (lattice paramater c).

The T_N *vs* P phase diagram displayed in Fig. 7.6 (a) is superimposed on a color contour representation of the power law exponent $n(P,T)$ from the expression for the electrical resistivity: $\rho = \rho_0 + A_n T^n$. The representation of n was determined from the logarithmic derivative of the electrical resistivity $\partial \ln(\rho - \rho_0)/\partial \ln T$, which yields the local behavior of $n(P,T)$. Interestingly, the local behavior of $n(P,T) = \partial \ln(\rho - \rho_0)/\partial \ln T$ corroborates most of the values of T_N as were determined from measurements of ρ (and the temperature derivatives, $d\rho/dT$) in the various pressure cells over the pressure range $P \sim 0$ to 27 GPa. This can be seen in the abrupt change in the value of n in the vicinity of T_N (i.e., at the $T_N(P)$ phase boundary). The local change in $n(P,T)$ is most evident at lower pressures ($P \leq 6$ GPa) in which the power law exponent changes abruptly from $n \sim 1.5$ (green-yellow) in the PM phase to $n \geq 2.5$ (yellow-red) in the AFM phase.

The effect of pressure on the parameters n, A_n, and ρ_0 (in the expression $\rho = \rho_0 +$

A_nT^n) below the Néel temperature is summarized in Fig. 7.6 (b), (c), and (d), respectively. At each pressure, the expression for ρ was fit to the $\rho(T)$ data in the AFM phase over the temperature range 5 K $< T < T_N$. (Examples of power law fits at selected pressures are displayed in Fig. 7.4.) The values of the power law exponent n in Fig. 7.6 (b) are consistent with the local behavior of $n(P,T)$ represented by the color contour in Fig. 7.6 (a). The representations of n in panels (a) and (b) of Fig. 7.6 both show a clear crossover at $P \sim$ 6 GPa from a $n \geq 2.5$ dependence during the enhancement of T_N to a $n = 2$ dependence during the suppression of T_N as pressure is increased above 6 GPa. Both the A_n coefficient and the residual electrical resistivity ρ_0 (at $T = 2$ K) increase steadily with increasing pressure up to $P \sim 15$ GPa as shown in Fig. 7.6 (b) and (c), respectively. While the residual electrical resistivity ρ_0 represents the contribution of impurity scattering to ρ, it is well recognized that spin fluctuations also play a significant role in the electrical resistivity of both ferromagnetic (FM) and AFM metals. [21, 27] This is often reflected in the large value of the coefficient A_2 in the A_2T^2 term. [21, 27] Here, we observe that the coefficient A_n appears to strengthen with increasing pressure up to $P \sim 15$ GPa. It is interesting to note that A_n reaches a maximum as the temperature dependence of the electrical resistivity stabilizes toward T^2 behavior (where n reaches a minimum). However, it should be mentioned that the parameter n is naturally conflated with the parameter A_n, making it difficult to speculate on their relative role in scattering processes.

The effect of sample quality and non-hydrostatic pressure on the Néel temperature

The values of T_N determined for TiAu sample 0 measured in the PCC and TiAu sample 1 measured in the initial BAC are approximately 3 K higher than the values of T_N for TiAu samples 2 and 3 that were measured in the second BAC and TiAu sample 4 measured in the DAC. The samples in the PCC and the first BAC were from the same

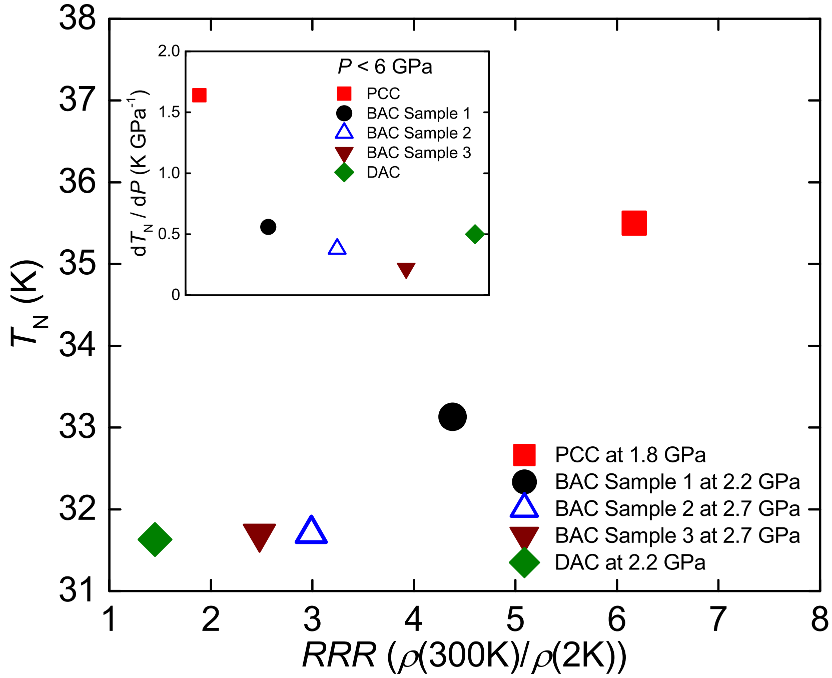

Figure 7.7: A plot of T_N *vs* residual resistivity ratio RRR = ρ(300 K)/ρ(2 K) for the five TiAu samples measured in each of the various pressure cells at a low pressure of $P \sim 2$ to 3 GPa Inset: Pressure coefficient dT_N/dP during the enhancement of T_N as pressure is increased up to $P \sim 6$ GPa for the five different TiAu samples.

synthesis but different than the synthesis that yielded the two samples in the second BAC and the sample in the DAC. This may indicate that the nominal value of T_N at ambient pressure may be sensitive to varying conditions during synthesis. Figure 7.7 shows a plot of the Néel temperature T_N *vs* the residual resistivity ratio (RRR) at a pressure $P \sim 2$ to 3 GPa for the five different TiAu samples measured in this study. It is apparent that for RRR ≥ 3, there is a significant increase in the Néel temperature from $T_N \sim 32$ K to $T_N \sim 35.5$ K. For RRR ≤ 3, there is no significant change in T_N. In addition, the RRR values for the samples from the initial TiAu synthesis (namely, the PCC sample 0 and BAC sample 1) are 2 to 4 times larger than the RRR values for the samples from the second TiAu synthesis (namely, BAC samples 2 and 3 and the DAC sample 4).

Based on the $T_N(P)$ dependence observed in the various pressure cells, it appears that T_N is also sensitive to the degree to which the pressure environment is hydrostatic. There is a large response of T_N to pressure as performed in the PCC when compared to the response of T_N at low pressure as performed in the two BACs and DAC. As shown in the inset of Fig. 7.7, the initial enhancement of T_N with P as observed in the PCC is $\mathrm{d}T_N/\mathrm{d}P = 1.64$ K GPa^{-1}, which is more than three times the enhancement of T_N with pressure as observed for the three samples measured in the two BACs and the sample measured in the DAC in which the pressure coefficients were observed to be $\mathrm{d}T_N/\mathrm{d}P = 0.56$ K GPa^{-1}, 0.38 K GPa^{-1}, 0.22 K GPa^{-1}, and 0.5 K GPa^{-1}, respectively. It is possible that the more hydrostatic conditions that are characteristic of the pressure-transmitting medium used in the PCC, when compared to the less hydrostatic environments typically achieved in the BAC and DAC, may result in the larger pressure coefficient, $\mathrm{d}T_N/\mathrm{d}P$, that we observed in the PCC up to $P \sim 2$ GPa. In previous investigations of the weak IFM Sc_3In, it was also found that the ferromagnetism is enhanced under the application of pressure under nearly hydrostatic conditions. [7, 11, 28] However, theoretical calculations show that the application of uniaxial strain (or non-hydrostatic pressure) results in a suppression of the

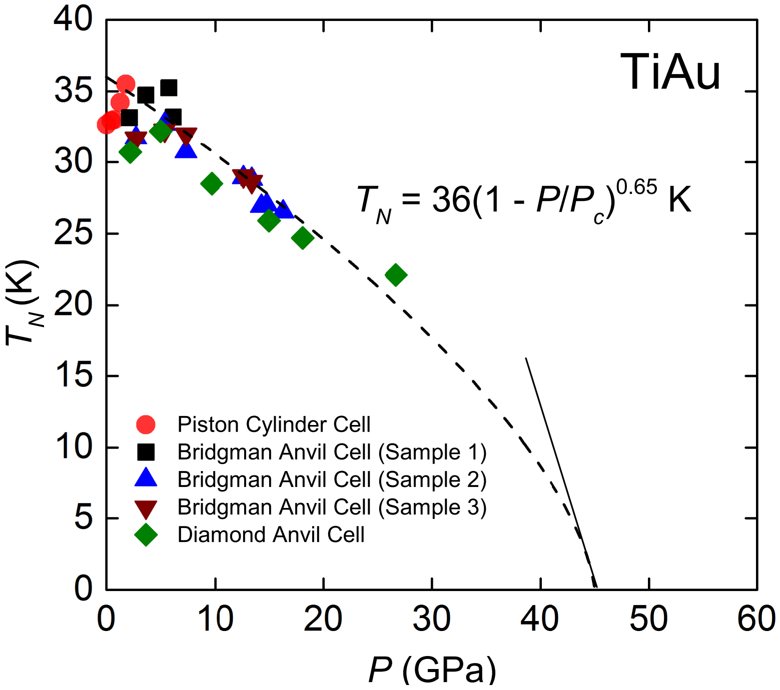

Figure 7.8: (a) A temperature *vs* pressure (T_N *vs* P) phase diagram for TiAu showing the extrapolated $T_N(P)$ boundary (dashed curve) toward a critical pressure P_c at T = 0 K. The critical scaling function $T_N = T_{N(P=0)} \times (1 - P/P_c)^{\alpha}$ was fit to the T_N(P) data up to P = 27 GPa. The ambient pressure value of the Néel temperature ($T_{N(P=0)}$) was set to 36 K while a rough estimate of the value for the critical pressure was determined from the fit to be P_c = 45 ± 11 GPa. The value for the scaling exponent α was determined from the fit to be α = 0.65 ± 0.20. The slope of the curve near T_N = 0 K (represented by the solid black line) is dT_N/d$P \sim -$ 2.5 K GPa^{-1}, while the slope of the nearly linear T_N(P) data accumulated from the various pressure cells up to $P = 27$ GPa is dT_N/dP = – 0.59 K GPa^{-1}.

magnetic order toward a possible QCP.[29]

7.4 Summary

At temperatures below T_N, conduction electrons in local moment systems typically scatter from both long and short-range spin fluctuations through the exchange interaction.[21] However, the long- and short-range fluctuations contribute differently to the electrical resistivity such that it is the short-range spin fluctuations that make the largest contribution to the electrical resistivity in a metal.[20, 21] This scenario also applies to weak itinerant-electron systems such as TiAu, in which the magnetic electrons are not localized. [20] Indeed, muon spin relaxation measurements [3] indicate that there is a rapid decay in the short-range spin fluctuations over a narrow temperature range during the transition from the PM phase to the AFM phase. This is reflected in the characteristic drop observed in the electrical resistivity $\rho(T)$ at T_N.

Recently, it was found that T_N = 36 K for the novel IAFM TiAu may be suppressed monotonically upon chemical doping toward a 2D AFM QCP. [3, 12] This served as the motivation for the present study in which we investigated the response of the magnetic order to applied pressure in the IAFM TiAu. As previously mentioned, there is an inherent competition between the strengthening of the exchange interaction (that tends to increase T_N) and the reduction (or broadening) of the DOS at the Fermi level (that tends to reduce T_N) as pressure is increased. However, at sufficiently high pressure, it is expected that the broadening of the $3d$-electron bandwidth W is dominant over the increase in the exchange interaction thus leading to a reduction in the magnetic ordering temperature (either T_C or T_N). [7]

In this investigation of the IAFM TiAu under pressure, we found that there is an initial enhancement of T_N with pressure up to $P \sim 6$ GPa after which T_N is reduced monotonically to $T_N \sim 22$ K at $P \sim 27$ GPa. This is in contrast to the monotonic suppression of T_N with increasing Sc concentration x in the $\mathrm{Ti}_{1-x}\mathrm{Sc}_x\mathrm{Au}$ system. Unfortunately, the characteristic drop in the electrical resistivity ρ is not well resolved at higher pressures, preventing a complete report on the suppression of T_N toward a QCP as was observed in the chemical doping study for $\mathrm{Ti}_{1-x}\mathrm{Sc}_x\mathrm{Au}$. The change in the temperature dependence of the electrical resistivity suggests there may be a crossover to a possible Fermi-liquid ground state in the AFM phase as T_N passes through its maximum value. We found that during the enhancement of T_N, the power law behavior of the electrical resistivity follows an n = 3 dependence which switches to an n = 2 dependence as T_N is suppressed with a further increase in pressure up to $P \sim 27$ GPA. However, it should be mentioned that on the basis of SCR theory for itinerant AFM metals, spin fluctuations are the dominant scattering mechanism responsible for both a n = 2 temperature dependence and also a large coefficient in the A_2T^2 term. [21] In the AFM phase below T = 30 K, there was no change observed in the magnetization $M(H)$ at ambient pressure in high fields up to H = 65 T. [26] Further experiments involving simultaneous application of both field and pressure are suggested in order to better determine the nature of the magnetic state (and possible scattering mechanisms at play) in the various regions of the T_N *vs* P phase diagram, both before and after the peak at $P \sim 5.5$ GPa.

Figure 7.8 shows a fit (dashed curve) of the scaling function $T_N = T_{N(P=0)} \times (1 - P/P_c)^{\alpha}$, to the T_N(P) data obtained from the measurements of ρ in the various pressure cells. The ambient pressure value of the Néel temperature $T_{N(P=0)}$, was set to 36 K while the estimated value for the critical pressure was determined from the fit to be $P_c = 45 \pm 11$ GPa and the value for the scaling exponent α was determined from the fit to be $\alpha = 0.65 \pm 0.20$. The slope of the curve near T_N = 0 K as indicated by the solid black line is $\mathrm{d}T_N/\mathrm{d}P \sim -2.5$ K GPa^{-1} while the slope of the nearly linear T_N(P) data accumulated from the various pressure cells up to P = 27 GPa is $\mathrm{d}T_N/\mathrm{d}P = -0.59$ K GPa^{-1}. There is a large error in the estimated values of both P_c and α, which is most likely due to the lack of T_N(P) data at higher pressure. Nevertheless, these values for the critical scaling parameters as well as the relative slopes for the two linear regions described previously are consistent with other systems that were forced toward a QCP with the application of pressure. [9, 30] We note that the projected value of the critical pressure, $P_c = 45$ GPa, is significantly smaller than the prediction of $P_c = 80$ GPa based on band structure calculations. [26] The overestimation of P_c may result from the tendency of band structure calculations to underestimate the role of electronic correlations. Hence, in the vicinity of a QCP, there is often an overestimation of the magnetic moment (or tendency towards magnetism) leading to an exaggerated value of P_c. [29]

Acknowledgements

Chapter 7, in full, is a reprint of the article, “Pressure effects in the itinerant antiferromagnetic metal TiAu,” by C. T. Wolowiec, Y. Fang, C. A. McElroy, J. R. Jeffries, R. L. Stillwell, E. Svanidze, J. M. Santiago, E. Morosan, S. T. Weir, Y. K. Vohra, and M. B. Maple, as it appears in *Phys. Rev. B* **95**, 214403 (2017). The dissertation author was the primary investigator and author of this paper.

Blbliography

[1] B. T. Matthias and R. M. Bozorth, “Ferromagnetism of a Zirconium-Zinc Compound”, Phys. Rev. **109**, 604–605 (1958).

[2] B. T. Matthias, A. M. Clogston, H. J. Williams, E. Corenzwit, and R. C. Sherwood, “Ferromagnetism in Solid Solutions of Scandium and Indium”, Phys. Rev. Lett. **7**, 7–9 (1961).

[3] E. Svanidze, J. K. Wang, T. Besara, L. Liu, Q. Huang, T. Siegrist, B. Frandsen, J. W. Lynn, A. H. Nevidomskyy, M. B. Gamza, M. C. Aronson, Y. J. Uemura, and E. Morosan, “An itinerant antiferromagnetic metal without magnetic constituents”, Nat. Commun. **6**, 7701 (2015).

[4] E. P. Wohlfarth, “Forced magnetostriction in the band model of magnetism”, J. Phys. C: Solid State Physics **2**, 68 (1969).

[5] P. Mohn, “Itinerant Electron Systems: Magnetism (Ferromagnetism)”, in *Concise Encyclopedia of Magnetic and Superconducting Materials*, edited by K. H. J. Buschow, 2nd ed. (Elsevior Ltd., Amsterdam, 2005), pp. 340–351.

[6] J. S. Schilling, “Some Recent Results in Magnetism under High Pressure”, in Physics of Solids Under High Pressure, Physics of Solids Under High Pressure, Proceedings of the International Symposium on the Physics of Solids under High Pressure, edited by J. S. Schilling and R. N. Shelton (1986), pp. 345–356.

[7] J. Grewe, J. S. Schilling, K. Ikeda, and K. A. Gschneidner, “Anomalous behavior of the weak itinerant ferromagnet Sc_3In under hydrostatic pressure”, Phys. Rev. B **40**, 9017–9024 (1989).

[8] R. C. Wayne and L. R. Edwards, “Effect of Pressure on the Curie Temperature of $ZrZn_2$”, Phys. Rev. **188**, 1042–1044 (1969).

[9] T. F. Smith, J. A. Mydosh, and E. P. Wohlfarth, “Destruction of Ferromagnetism in $ZrZn_2$ at High Pressure”, Phys. Rev. Lett. **27**, 1732–1735 (1971).

[10] J. G. Huber, M. B. Maple, D. Wohlleben, and G. S. Knapp, “Magnetic properties of $ZrZn_2$ under pressure”, Solid State Commun. **16**, 211–216 (1975).

[11] W. E. Gardner, T. F. Smith, B. W. Howlett, C. W. Chu, and A. Sweedler, “Magnetization Measurements and Pressure Dependence of the Curie Point of the Phase Sc_3In”, Phys. Rev. **166**, 577–588 (1968).

[12] E. Svanidze, T. Besara, J. K. Wang, D. Geiger, L. Prochaska, J. M. Santiago, J. W. Lynn, S. Paschen, T. Siegrist, and E. Morosan, “Quantum critical point in the Sc-doped itinerant antiferromagnet TiAu”, Phys. Rev. B **95**, 220405 (2017).

[13] T. F. Smith, C. W. Chu, and M. B. Maple, “Superconducting manometers for high pressure measurement at low temperature”, Cryogenics **9**, 53 (1969).

[14] G. D. Smith, U.S. Patent No. 3,356,542, 1967.

[15] H. K. Mao, J. Xu, and P. M. Bell, “Calibration of the ruby pressure gauge to 800 kbar under quasi-hydrostatic conditions”, J. Geophys. Res.: Solid Earth **91**, 4673 (1986).

[16] W. L. Vos and J. A. Schouten, “On the temperature correction to the ruby pressure scale”, J. App. Phys. **69**, 6744 (1991).

[17] E. Fawcett, “Spin-density-wave antiferromagnetism in chromium”, Rev. Mod. Phys. **60**, 209–283 (1988).

[18] J. A. Hofmann, A. Paskin, K. J. Tauer, and R. J. Weiss, “Analysis of ferromagnetic and antiferro-magnetic second-order transitions”, J. Phys. Chem. Solids **1**, 45–60 (1956).

[19] E. D. Thompson, “Low temperature magnetic specific heat of nickel”, Phys. Lett. **23**, 411–412 (1966).

[20] M. E. Fisher and J. S. Langer, “Resistive Anomalies at Magnetic Critical Points”, Phys. Rev. Lett. **20**, 665–668 (1968).

[21] K. Ueda, “Electrical Resistivity of Antiferromagnetic Metals”, J. Phys. Soc. Japan **43**, 1497–1508 (1977).

[22] E. Svanidze, L. Liu, B. Frandsen, B. D. White, T. Besara, T. Goko, T. Medina, T. J. S. Munsie, G. M. Luke, D. Zheng, C. Q. Jin, T. Siegrist, M. B. Maple, Y. J. Uemura, and E. Morosan, “Non-Fermi Liquid Behavior Close to a Quantum Critical Point in a Ferromagnetic State without Local Moments”, Phys. Rev. X **5**, 011026 (2015).

[23] T. F. Smith and W. E. Gardner, “Pressure Dependence of the Superconducting Transition Temperature of Uranium”, Phys. Rev. **140**, A1620–A1623 (1965).

[24] W. E. Gardner and T. F. Smith, “Superconductivity of α-Uranium and Uranium Compounds at High Pressure”, Phys. Rev. **154**, 309–315 (1967).

[25] D. D. Jackson, J. R. Jeffries, W. Qiu, J. D. Griffith, S. McCall, C. Aracne, M. Fluss, M. B. Maple, S. T. Weir, and Y. K. Vohra, “Structure-dependent ferromagnetism in Au_4V studied under high pressure”, Phys. Rev. B **74**, 174401 (2006).

[26] E. Svanidze, “Search, Discovery, Synthesis, and Characterization of Itinerant Magnets Composed of Non-magnetic Constituents”, PhD thesis (Rice University, Apr. 2015).

[27] T. Moriya, *Spin Fluctuations in Itinerant Electron Magnetism* (Springer-Verlag, Berlin, 1985).

[28] P. C. Riedi, J. G. M. Armitage, and R. G. Graham, “Forced magnetostriction and pressure dependence of the magnetism of weakly ferromagnetic $\mathrm{Y(Co}_{1-x})_2$ and $\mathrm{Sc_3In}$”, Journal of Applied Physics **69**, 5680–5682 (1991).

[29] A. Aguayo and D. J. Singh, “Erratum: Itinerant ferromagnetism and quantum criticality in $\mathrm{Sc_3In}$ [Phys. Rev. B **66** , 020401 (2002)]”, Phys. Rev. B **67**, 139902 (2003).

[30] N. Kernavanois, S. Raymond, E. Ressouche, B. Grenier, J. Flouquet, and P. Lejay, “Neutron diffraction study under pressure of the heavy-fermion compound $\mathrm{CePd_2Si_2}$”, Phys. Rev. B **71**, 064404 (2005).